

APPLICATIONS OF METAMATERIAL INSPIRED STRUCTURES IN DESIGN OF CIRCULARLY POLARIZED ANTENNAS

Thesis

Submitted in partial fulfillment of the requirements for the degree of

DOCTOR OF PHILOSOPHY

by

PUNEETH KUMAR T R



DEPARTMENT OF ELECTRONICS & COMMUNICATION ENGINEERING

NATIONAL INSTITUTE OF TECHNOLOGY KARNATAKA

SURATHKAL, MANGALORE - 575025, INDIA

June 2020

DECLARATION

I hereby *declare* that the Research Thesis entitled **APPLICATIONS OF METAMATERIAL INSPIRED STRUCTURES IN DESIGN OF CIRCULARLY POLARIZED ANTENNAS** which is being submitted to the **National Institute of Technology Karnataka, Surathkal** in partial fulfillment of the requirements for the award of the Degree of **Doctor of Philosophy in Department of Electronics and Communication** is a *bonafide report of the research work carried out by me*. The material contained in this thesis has not been submitted to any University or Institution for the award of any degree.

Puneeth Kumar T R

Register No.: 165090EC16F08

Department of Electronics and Communication Engineering

Place: NITK Surathkal

Date:

CERTIFICATE

This is to *certify* that the Research Thesis entitled **APPLICATIONS OF METAMATERIAL INSPIRED STRUCTURES IN DESIGN OF CIRCULARLY POLARIZED ANTENNAS**, submitted by **Puneeth Kumar T R** (Reg. No.: 165090EC16F08) as the record of the research work carried out by him, is *accepted as a Research Thesis submission* in partial fulfillment of the requirements for the award of degree of **Doctor of Philosophy**.

Dr.Krishnamoorthy K.

Research Guide

Assistant Professor

Department Electronics and Communication Engg.

NITK Surathkal - 575025

Chairman - DRPC

(Signature with Date and Seal)

*This thesis is dedicated to my beloved
Mother*

ACKNOWLEDGEMENTS

First and foremost, I take this opportunity to thank the Lord Almighty for enabling me to work persistently in pursuit of this research work, and for empowering me with the strength and perseverance towards the fruitful accomplishment of the task.

Next, I offer my deepest gratitude to my research guide, Dr. K. Krishnamoorthy who has been a constant source of support and encouragement to me. His timely counseling has always guided me technically and morally. His profound knowledge and thorough patience have always been a beacon of light for me throughout the course of my journey.

I owe my sincere thanks to Prof. M. S. Bhat and Prof. U. Shripathi Acharya, Prof. M. Kulkarni former heads and Prof. T. Laxminidhi, the present head, Department of Electronics and Communication Engineering for their valuable advice and administrative support. I would also like to acknowledge the encouragement, guidance and useful evaluation provided by my RPAC members, Dr. Joseph Antony, Dr. Arulalan M.R, Dr. Pathipati srihari and Dr.CMC Krishnan. I take this opportunity to thank all the teaching and non teaching staff and the lab technicians for offering their valuable expertise at all times which has helped me realize the goals of my work at a faster pace.

I particularly thank my fellow scholars who have been a part of my journey and helped me technically and motivated me. I take this opportunity to genuinely thank all my friends from far and near who have always been with me, never failing to support me and lift me up at times of need. I will forever be indebted to them for their invaluable friendship, care, concern and timely interventions.

Throughout the different phases of my Ph.D., the love and support provided by my family know no bounds, I thank them for always having worked behind the scenes for me. Their silent prayers and gentle chiding have molded me into the person I am today. A special word of thanks to my sisters, brother-in-law's, nieces and nephew for their

benevolence and guidance at every juncture of my course. I especially wish to thank my wife and the unparalleled support of my parents, who have provided me, for the sacrifices they have made, and for always believing in me.

ABSTRACT

This research is devoted to the potential properties of metamaterial (MTM) inspired structures in the design of novel circularly polarized (CP) antennas. Metamaterials (MTMs) are the artificially designed structures that have generated significant research interest through their unusual properties to achieve the demands of the modern era. Modern wireless communication like satellite, radar and mobile communication demands single feed, low profile, compact and low-cost antennas with multiple functionalities. To achieve these requirements, different metamaterial inspired structures are analyzed and utilized to design CP antennas with wideband, multi-band, high gain and RCS reduction properties. In addition, characteristic mode analysis technique is utilized to properly analyze the modes of an antenna, which contributes to radiation performance of the antenna.

This thesis focuses on metasurface (MTS) based antenna design, which gives multiple functions with CP characteristics. MTS is designed and analyzed using the theory of characteristic modes to achieve CP. Parameters like eigenvalues, modal significance, and characteristic angle help to analyze modes, which contribute to produce CP waves. Later, the absorptivity property of MTS is investigated to obtain its RCS reduction capability. The other design presents a slot antenna with the concept of an artificial magnetic conductor (AMC). The proposed AMC acts as a polarization-dependent frequency selective surface (FSS), which produces a zero degree reflection phase at the required resonance frequency. This reflective property helps to design wideband CP antenna with good gain.

Also, the concept of zero refractive index is introduced, which is used to enhance the gain of a primary antenna with simultaneous polarization conversion capability. MTS cover atop of LP patch antenna increases gain and converts LP into CP waves. Transmission and reflection property of the designed unit-cell is studied and its constitutive

parameters are extracted to justify its functionality. Zero-refractive index based MTS has no phase variation at its interface, which helps to focus energy towards the intended direction, thus enhancing the gain.

Multiband CP antennas with independent control of resonance frequency bands are much needed for wireless technologies to operate in a mobile environment. A dual-band CP antenna with wideband characteristics is designed using a slot and a pair of copper strips. Triband CP antenna is designed using the MTM structure called split-ring resonator(SRR) to obtain triple bands and control each resonance frequency bands independently. Also, polarization sense in each band is controlled through structural modification of the antenna design.

Proposed designs are fabricated using LPKF protomat machine S103 and experimentally verified using radiation pattern measurement set-up. Impedance bandwidth, peak gain, axial ratio bandwidth, radiation efficiency, radar cross-section and cross-polarization level are various metrics considered for the performance measures of the proposed designs with earlier work presented in the literature.

Keywords: Slot antenna, Patch antenna, Circular Polarization, Metamaterials, Meta-surface, Zero index metamaterial, Split ring resonator.

TABLE OF CONTENTS

ACKNOWLEDGEMENTS	ii
ABSTRACT	iv
LIST OF FIGURES	xvi
LIST OF TABLES	xvii
ABBREVIATIONS	xviii
1 INTRODUCTION	1
1.1 Introduction to Wireless Communication Systems and Antennas . . .	1
1.1.1 Mobile and Space Communication	2
1.1.2 Antenna systems for mobile and space communications . . .	4
1.2 Motivation	6
1.3 Problem Definition	7
1.4 Objectives	8
1.5 Methodology	8
1.6 Organization of the Thesis	9
2 BACKGROUND AND LITERATURE SURVEY	12
2.1 Circular polarization	12
2.1.1 Advantages of CP antennas	13
2.2 Introduction to Metamaterials	15
2.2.1 Split Ring Resonator	18
2.2.2 Metasurfaces	24
2.2.3 Frequency Selective Surface(FSS)	26

2.2.4	Zero-index based Metasurfaces	28
2.3	Theory of Characteristic Modes	30
2.4	Literature Survey	34
2.4.1	Characteristic mode based antennas and RCS reduction in meta- surface antennas	34
2.4.2	Wideband metasurface based circularly polarized antennas	39
2.4.3	High Gain Metasurface Antennas	41
2.4.4	Multiband Circularly Polarized Antennas	43
3	CHARACTERISTIC MODE ANALYSIS OF A COMPACT METASUR- FACE ANTENNA WITH CIRCULAR POLARIZATION AND LOW RCS	46
3.1	Introduction	46
3.2	Characteristic Mode Analysis of PDMTS	47
3.2.1	CMA of PDMTS with slot	49
3.3	Circularly polarized antenna design using PDMTS	51
3.4	RCS Reduction of the MTS CP Antenna	54
3.5	Fabrication and experimental results	56
3.6	Summary	59
4	WIDEBAND ANTENNAS WITH CIRCULAR POLARIZATION CHAR- ACTERISTICS	60
4.1	Introduction	60
4.2	A slot antenna with circular polarization and wideband characteristics using Frequency Selective Surface	61
4.2.1	Antenna structure and Its operation	61
4.2.2	Fabricated design and Results	66
4.3	A SRR loaded compact planar slot antenna with circular polarization and wideband characteristics for soil moisture sensor application	69
4.3.1	Antenna Design and its principle	69
4.3.2	Fabricated structure and its Results	73
4.3.3	Soil sensing application	75
4.4	Summary	77

5	HIGH GAIN METASURFACE BASED ANTENNAS WITH CIRCULAR POLARIZATION CHARACTERISTICS	78
5.1	Introduction	78
5.2	A Zero-Index Metasurface Based High Gain Antenna with Circular Polarization Characteristics	78
5.2.1	Structure and operating principle of the antenna	79
5.2.2	Experimental results and discussion	81
5.3	A zero index metasurface based high gain antenna with polarization conversion	84
5.3.1	Antenna Design and Operating Principle	84
5.3.2	Results and Discussion	91
5.3.3	Summary	94
6	MULTIBAND ANTENNAS WITH CIRCULAR POLARIZATION CHARACTERISTICS	95
6.1	Introduction	95
6.2	Dual Band CP antenna Using Asymmetric Cross Strips	95
6.2.1	Working principle of the antenna and its structure	96
6.2.2	Fabricated antenna and experimental results	98
6.3	Tri-band circularly polarized antenna using SRRs	101
6.3.1	Antenna structure and principle of operation	101
6.3.2	Fabricated prototype and its results	107
6.4	Summary	111
7	CONCLUSION AND FUTURE WORK	112
7.1	Contributions	112
7.1.1	CM based CP metasurface Antenna	113
7.1.2	Wideband CP antennas	113
7.1.3	High gain CP antennas	113
7.1.4	Multiband CP antennas	114
7.2	Future Work	114

LIST OF PUBLICATIONS BASED ON THESIS	116
CURRICULUM VITAE	117
REFERENCES	118

LIST OF FIGURES

1.1	Evolution of cellular technology(Viswanathan and Weldon (2014)).	3
2.1	Polarization ellipse plotted as a function of time and traced at a position in space.	13
2.2	Material classification based on permeability- permittivity and refractive index (Caloz and Itoh (2005))	16
2.3	Negative refraction(Engheta and Ziolkowski (2006))	16
2.4	First experimented LH materials consists of Thin wires and split ring resonators (a) LH structure with single dimension (b)LH structure with two dimension(Caloz and Itoh (2005)).	17
2.5	The structure of split ring resonator (SRR) in cylindrical form and planar form discoverd by Pendry. The magnetic field is induced orthogonal to the plane (conventional axis) of rings	19
2.6	Equivalent circuits of SRRs. (a) Double loop SRR configuration (b) Single loop SRR configuration(Caloz and Itoh (2005))	19
2.7	Experimental set-up to realize SRR behavior in a hallow metallic waveguide.(a)Simulation set-up (b) Transmission coefficient magnitude(Marqués et al. (2002))	20
2.8	Transmission coefficient of circular SRR as a function of rotation angle θ of inner ring(Saha and Siddiqui (2012))	21
2.9	Structure of different SRRs (a)Unit cell A (b) Unit cell B (c) Unit cell C(Ekmekci et al. (2009))	22
2.10	(a)Transmission coefficient of unit cell A (b) its photograph	23
2.11	(a)Transmission coefficient of unit cell B (b) its photograph	23
2.12	(a)Transmission coefficient of unit cell C (b) its photograph	23
2.13	Metasurface functionalities: (a) bandpass frequency selective surface (b)bandstop frequency selective surface (c) high-impedance surface (d) narrowband perfect absorber(e) twist polarizer (f) right-handed circular-polarization frequency selective surface (g) linear to circular polarization converter (h) two-dimensional leaky-wave antenna with a conical-beam pattern (i) focusing transmitarray; (j) focusing reflectarray (k) flat Luneburg lens (l) hologram.(Glybovski et al. (2016)).	24

2.14	Three regions of a composite material characteristics (Holloway et al. (2012)).	25
2.15	(a) array of circular metallic patches and array of circular apertures (b) array of square metallic loops and array of square aperture rings . . .	27
2.16	The transmission line model of frequency selective surface embedded in two dielectrics(Costa et al. (2012)).	27
2.17	The zero index lie in the intersection of material classification based on ϵ and μ Engheta and Ziolkowski (2006)	29
2.18	The spatial field distribution of (a)simple patch source and (b) zero-index based MTS	30
2.19	Characteristic modal currents of an arbitrary shaped conducting body (a) mode1 (b)mode 2	31
2.20	(a)Eigen values (b) modal significance and characteristic angle of rectangular PEC plate.	33
2.21	First four modal currents and modal radiation patterns of rectangular PEC plate	33
2.22	Wideband MTS antenna using CMA	35
2.23	Modal currents and modal patterns of MTS antenna(Lin and Chen (2017))	36
2.24	RCS reduction using checkerboard type metasurface (Chen et al. (2016d))	38
2.25	RCS reduction using absorbing type of cross slot based MTS (Kandasamy et al. (2015))	38
2.26	(a)The fabricated prototype of simple dipole backed by polarization dependent MTS. (b) experimentally verified reflection coefficient and axial ratio plots (Fan Yang and Rahmat-Samii (2005))	40
2.27	(a)The multilayer ZIM based high gain antenna prototype (b) Frequency response of refractive index (c) S_{11} plot (d) comparison between gain and directivity plot (Zhou et al. (2009))	42
2.28	Proposed asymmetrical multiband CP Antenna (a) cross-sectional view and (b) top view(Reddy and Sarma (2014))	44
3.1	(a) Geometry of the proposed PDMTS (b) Open radiation boundary set up with PEC in the -Z direction. $L_g=27\text{mm}$, $L_p=8.5\text{mm}$, $W_p=6\text{mm}$, $W_s=0.3\text{mm}$, $h_s=3.454\text{mm}$	47
3.2	Simulated (a) modal significance(MS) and (b) characteristic angle(CA) of the first four modes(J1-J4) of PDMTS.	48

3.3	Simulated (a)modal significance and (b)characteristic angle of first two modes(J1, J2) of PDMTS.	48
3.4	Simulated modal current distribution of PDMTS (a)J1 (b)J2 (c)J3 (d)J4	49
3.5	Simulated modal radiation pattern of PDMTS. (a)J1 (b)J2 (c)J3 (d)J4	49
3.6	Effect of W_p on simulated (a) modal significance (b) characteristic angle.	50
3.7	Effect of W_s on simulated (a) modal significance (b) characteristic angle	50
3.8	CM analysis of MTS with slot (a) modal significance (b) characteristic angle	51
3.9	Structure of the proposed design (a) front view (b) side view (c) back view	52
3.10	Simulation results of Surface current distribution at different time instant (a) t=0 (b) t=T/4 (c) t=T/2 (d) t=3T/4	52
3.11	Effect of L_f and W_f on simulated S_{11} and axial ratio (a & b) L_f (c & d) W_f	53
3.12	Effect of W_s and W_p on simulated S_{11} and axial ratio (a & b) W_s (c & d) W_p	53
3.13	Simulated absorptivity magnitude of metal backed PDMTS (b) Simulated monostatic RCS variation of PDMTS loaded slot antenna over oblique incidence (c) simulated frequency response of the monostatic RCS vs oblique incidence (d) simulated and measured monostatic RCS vs Angle at 5.86 GHz for y polarized wave (e) simulated and measured frequency response for y polarized wave at broadside direction.	55
3.14	Prototype of the fabricated structure (a) front view(MTS) (b) back view(slot) (c) micro-strip line feed	57
3.15	Simulated and measured S_{11} , axial ratio and gain (a) S_{11} (b) axial ratio and gain	57
3.16	Simulated and measured RHCP and LHCP radiation pattern at 5.86 GHz (a) xz palne (b) yz palne and 6.3 GHz (c) xz plane (d) yz Plane	58
4.1	The proposed FSS-based antenna structure.	62
4.2	Simulation results of reflection coefficient plot and axial ratio plot of the perturbed slot antenna. (a) $ S_{11} $ (b) axial ratio.	63
4.3	Simulated electric field distribution of the truncated slot antenna at 3.47 GHz. (a) $\omega t=0$ (b) $\omega t=90^0$	63
4.4	The FSS unit-cell characteristics in-terms of its reflection phase	64

4.5	Simulation results of reflection coefficient and axial ratio of the antenna design process. (a) $ S_{11} $ (b) axial ratio.	65
4.6	Simulation results of reflection coefficient, gain and axial ratio plot of the slot, the slot with PEC, and the slot with FSS. (a) $ S_{11} $, (b) axial ratio, (c) $ S_{11} $ of the designed antenna with and without tuning stubs, (d) gain variation of the presented antenna with and without FSS. . .	65
4.7	Photograph of the fabricated design. (a) Slot antenna,(b) FSS, (c) proposed antenna.	67
4.8	Simulation and measured results of reflection coefficient, axial ratio, and gain of the proposed antenna. (a) $ S_{11} $, (b) axial ratio and gain. .	67
4.9	Simulation and experimental results of LHCP and RHCP radiation patterns in (a) azimuth plane at 3.98 GHz, (b) elevation plane at 3.98 GHz, (c) azimuth plane at 4.42 GHz, and (d) elevation plane at 4.42 GHz.	68
4.10	Top view of the designed antenna structure. $W_g=70$ mm, $S=26$ mm, $a=8.4$ mm, $W_f=3$ mm, $g=0.3$ mm, $f_0=3$ mm, $L_f=33$ mm	70
4.11	Simulation results of reflection coefficient and axial ratio curves of perturbed slot antenna with different values of truncation (a) S_{11} (b) Axial ratio	71
4.12	Simulation results of reflection coefficient and axial ratio curves of wideband CP antenna design process (a) S_{11} (b) Axial ratio	71
4.13	Simulated electric field variation at different time instances at slot resonance 4.12 GHz (a)t=0 (b)t=T/4 (c) Electric field distribution at SRR resonance 4.6 GHz	72
4.14	Simulation results of reflection coefficient magnitude and axial ratio plot of wideband CP antenna (a) S_{11} of the feed shifted antenna (b) axial ratio of the feed shifted antenna (c) S_{11} plot with and without SRR (d) axial ratio plot with and without SRR	73
4.15	(a) Photograph of the fabricated antenna structure (b) simulated and measured reflection coefficient plot (c) measured and simulated plot of axial ratio (d) simulated and measured gain	74
4.16	Comparison between simulated and measured radiation pattern at different CP frequencies.(a) xz plane at 3.8 GHz (b) yz plane at 3.8 GHz (c) xz plane at 4.12 GHz (d) yz plane at 4.12 GHz (e) xz plane at 4.8 GHz (f) yz plane at 4.8 GHz	75
4.17	(a) Simulated reflection coefficient of wideband CP antenna with and without soil (b) comparison between measured and simulated reflection coefficient of wideband CP antenna with dry and wet soil (c) testing environment	76

5.1	Proposed unit-cell geometry. (a) Front view (b) Back view (c) Boundary condition. $L_u=8.5\text{mm}$, $L_1=4.5\text{ mm}$, $L_2=3.7\text{ mm}$, $L_3 = L_4=1.75\text{ mm}$, $L=5\text{ mm}$, $W=0.4\text{ mm}$, $g=0.4\text{ mm}$, $h_s=0.8\text{ mm}$	79
5.2	Effective parameters of the proposed unit-cell.	80
5.3	Proposed antenna geometry. (a) patch antenna (b) zero-index based MTS (c) side view of the high gain CP antenna. $L_p=10.6\text{ mm}$, $a=1\text{ mm}$, $L_g=76.5\text{ mm}$, $h_{am}=21.5\text{ mm}$, $h_a=0.508\text{ mm}$	80
5.4	Simulated gain comparison of the proposed antenna with and without MTS.	81
5.5	Fabricated prototype (a) MTS front view (b) MTS back view (c) Patch antenna (d) Proposed high gain CP antenna	82
5.6	Comparison between measured and simulated reflection coefficient and axial ratio. (a) S_{11} (b) axial ratio	82
5.7	(a) Comparison between simulated and measured gain (b) simulated radiation efficiency	83
5.8	Comparison between measured and simulated radiation patterns at 7.5 GHz (a) xz plane (b)yz plane	83
5.9	(a)Proposed ZIM based unit cell geometry(b) Simulation set-up	84
5.10	Simulated reflection and transmission coefficient and extracted parameters of the unit cell. (a) Magnitude curves of S_{11} and S_{21} . (b) Phase curves of S_{11} and S_{21} . (c) Effective permeability and permittivity. (d) Refractive index.	86
5.11	Transmission coefficient phase variation of the unit-cell for oblique plane wave incidence. (a) Transmission coefficient phase of x-component. (b) Transmission coefficient phase of y-component.	87
5.12	Proposed high-gain antenna with ZIM unit cells. $L = 76.5\text{ mm}$, $L_p = 12.6\text{ mm}$, $W_p = 12.2\text{ mm}$, $h_m = 22.3\text{mm}$, $h_a = 0.8\text{ mm}$, and $h_s = 1.52\text{ mm}$	88
5.13	Simulated gain and axial ratio variation of the proposed antenna with and without ZIM. (a) Gain. (b) Axial ratio.	89
5.14	Simulated surface current distribution of a portion of the MTS at different time instants. (a) $\omega t = 0^0$. (b) $\omega t = 90^0$	89
5.15	(a)Reflection coefficient plot variation for split gap g1 (b) Axial ratio plot variation for split gap g1.	90
5.16	(a)Reflection coefficient plot variation for split gap g2 (b) Axial ratio plot variation for split gap g2.	90

5.17	(a) Reflection coefficient plot for different height between patch and ZIM.(b) Gain plot for different height between patch and ZIM.	90
5.18	Fabricated high-gain CP antenna. (a) Patch antenna. (b) Double-sided 9×9 ZIM unit cells. (c) Proposed high-gain CP antenna.	91
5.19	Comparison between measured and simulated (a) Reflection coefficient (b) Axial ratio and gain	92
5.20	Radiation pattern of the proposed antenna at 7.34 GHz. (a) xz plane. (b) yz plane.	92
6.1	The proposed antenna geometry. $W_g=70\text{mm}$, $S_l=29.6\text{mm}$, $a=8.4\text{mm}$, $W_f=2.5\text{mm}$, $L_f=34.5\text{mm}$, $L_{s1}=26\text{mm}$, $L_{s2}=24\text{mm}$	96
6.2	The design process of presnetd dual-band CP antenna. (a) Simulated reflection coefficient (b) Simulated axial ratio	97
6.3	Simulated Electric field distribution at 2.76 GHz (a) $t=0^0$ (b) $t=90^0$ and 3.82GHz (c) $t=0^0$ (d) $t=90^0$	98
6.4	Simulation results of surface current distribution of designed antenna at 3.82GHz	98
6.5	The fabricated prototype of proposed dual band CP antenna (a) top view (b) bottom view	99
6.6	(a)Simulated and measured reflection coefficient (b) Simulated and measured axial ratio and gain	99
6.7	Comparison between measured results and simulated results of radiation pattern of the dual band CP antenna at 2.76 GHz and 3.82 GHz. (a)xz plane (b) yz plane (c)xz plane (d) yz plane	100
6.8	Geometry of the triband CP antenna $W_g=70$ mm, $S=28$ mm, $a=10$ mm, $W_f=3$ mm, $g=0.7$ mm, $L_f=33$ mm	102
6.9	Simulation results of reflection coefficient and axial ratio of truncated slot antenna for different values of a (a) S_{11} (b) axial ratio	103
6.10	Simulation results of reflection coefficient and axial ratio of triband CP antenna design process. (a) Reflection coefficient (b) Axial ratio	103
6.11	Simulated Electric field distribution at 4.4 GHz. (a) $\omega t = 0^0$ (b) $\omega t = 90^0$ (c) variation in the surface current of SRRs at 4.77 GHz and 5.1 GHz.	104
6.12	Equivalent circuit modeling of the triband CP antenna (a) SRR loaded CPW fed slot antenna (b) simplified equivalent circuit of proposed antenna. (c) The simulated reflection coefficient comparison between EM and circuit simulation	105

6.13	Simulation results of reflection coefficient and axial ratio due to variation of S_l , R_1 and split gap g_c . (a) S_{11} due to variation of S_l (b) axial ratio due to variation of S_l (c) S_{11} due to variation of R_1 (d) axial ratio due to variation of R_1 (e) S_{11} due to variation of g_c (f) axial ratio due to variation of g_c	106
6.14	(a) Prototype of the fabricated antenna (b) Radiation pattern measurement set-up for the proposed tri-band CP antenna	108
6.15	(a) Simulated and measured reflection coefficient (b) Simulated and measured axial ratio	108
6.16	Comparison between measured and simulated gain and simulated radiation efficiency (a) Gain (b) Radiation efficiency	108
6.17	Simulated and measured radiation pattern of proposed antenna at 4.15 GHz, 4.77 GHz, 5.1 GHz (a) xz plane (b) yz plane (c) xz plane (d) yz plane (e) xz plane (f) yz plane	110

LIST OF TABLES

3.1	Comparison of performance metrics of the proposed CMA based MTS CP antenna	59
5.1	The performance metrics comparison between the high gain CP antenna and existing literature	93
6.1	The comparison of the triband CP antenna with recent literature	111

ABBREVIATIONS

AMC	Artificial Magnetic Conductor
ARBW	Axial ratio bandwidth
CMA	Characteristic Mode Analysis
CPW	Co-planar waveguide
CP	Circular Polarization
EBG	Electromagnetic Band Gap
FSS	Frequency Selective Surface
HIS	High Impedance Surface
IoT	Internet of Things
IBW	Impedance bandwidth
LP	Linear Polarization
MTM	Metamaterial
MOM	Method of Moment
MSA	Microstrip Antenna
MTS	Metasurface
PDMTS	Polarization Dependent Metasurface
RFID	Radio Frequency Identification
RCS	Radar Cross Section
SRR	Split Ring Resonator
UWB	Ultra-wideband
ZIM	Zero-Index Metamaterial

CHAPTER 1

INTRODUCTION

Antenna is an essential part of the wireless communication system. The IEEE definition of an antenna is “a means of radiating or receiving electromagnetic waves”. In the communication system, an antenna is the first device at the receiving side and terminal device at the transmitter side (Balanis, 2005). Therefore, a careful design of an antenna is needed to maintain the required performance in the communication system. This chapter briefly describes the various wireless communication systems and their antenna systems. Many antennas are developed based on the requirement in communication systems; still, research gaps need to be filled in modern wireless communication that requires antenna systems with multiple functionalities. The work motivation, problem definition, formulation of objectives, work methodology and organization of the thesis are also discussed in this chapter.

1.1 Introduction to Wireless Communication Systems and Antennas

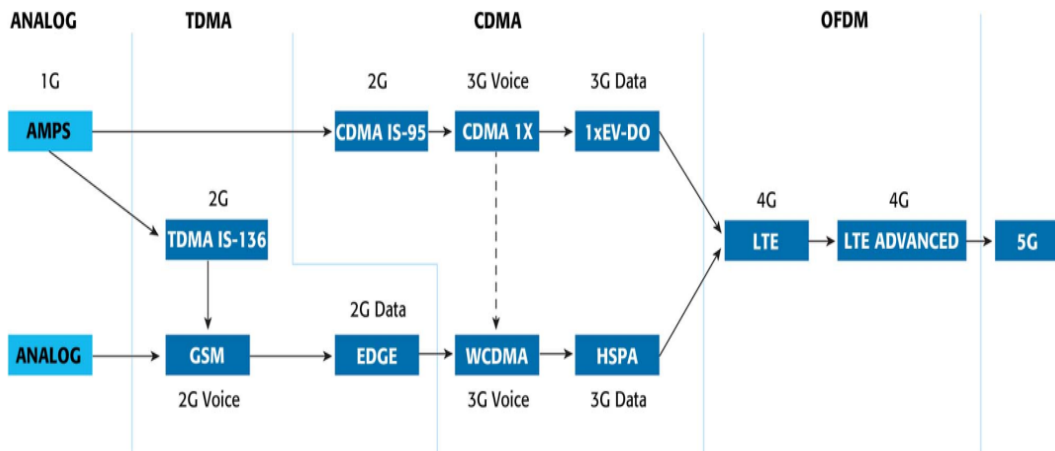
Wireless communication has grown very fast due to technological advancement with the better transmission, reception, and signal processing. Wireless communication begins with the theoretical studies of EM wave by Maxwell and experimental demonstration by Hertz. Since then, advancement in the wireless domain becomes numerous, and a lot of experiments were conducted on EM waves to carry the information. This section briefly discusses the evolution of different wireless technologies and their antenna systems, which simplifies the overall architecture of the communication system. It describes mobile technology from the first generation to the current generation, which led to the antenna design from a larger profile to compact and low profile with multiple functions.

Also, it discusses space communications, such as satellite and radar communications, which find numerous applications in the modern era.

1.1.1 Mobile and Space Communication

Wireless communication has become a new frontier for numerous applications like mobile, satellite, radar, military and biomedical, sensing, etc. It begins in the year 1946 with the first mobile phone service introduced by the united states with half-duplex mode. Later, improved mobile phone services (IMPS) are presented in the year 1960 with a full-duplex method. After the introduction of IMPS, demand increases due to more number of users. Cellular radio-telephony was developed by AT&T Bell laboratories and other companies to increase spectrum range and cover more area. In general, generation (G) in mobile technology refers to change in the fundamental service aspects like wide bandwidth, transmission technique, higher data rates and new frequency band allocation. Mobile communication started with first-generation (1G) cellular network, which uses analog transmission in the year 1980, followed by the second generation(2G) digital cellular technology.

In 1988, Europe introduced digital cellular communication called Global System for Mobile(GSM) communication. The 2G network provides digitally encrypted voice calls and efficient utilization of the frequency spectrum to accommodate the increased number of mobile users. Separate channels allocated to voice and data (text messages) with a transfer speed of 40 kbits/s. The third-generation (3G) network is introduced in 1998, which provides a minimum data rate of 144 kbits/s. 3G replaces 2G and 2.5G GPRS technology. 3G technology contributed many improved services like voice telephony, video calls, mobile internet access and mobile TV. In 2008, the fourth generation (4G) started and provided better services and applications like voice over IP(Internet Protocol), HDTV and high data rate up to 1 Gbps. The evolution of mobile generation is shown in Fig.1.1. Fifth-generation (5G) wireless technology expected to provide advanced features like cloud and pervasive computing that makes the enormous number of network connections. 5G is also capable of delivering higher bit rates using



(a)

Figure 1.1: Evolution of cellular technology(Viswanathan and Weldon (2014)).

macro-diversity techniques and new trends like the internet of things(IoT) in which many devices are connected to mobile through the internet. To successfully carry out the massive number of connections with less interference and better signal reception, multi-functional antennas play an essential role and they required improvement to meet the specifications of current generation wireless standards.

In the research era of space communication, radars and satellites were grown significantly due to their potential applications. World’s first communication satellite Telstar 1 was launched in the year 1962 by AT & T Bell labs. Telstar fascinated the world with its services like live images, entertainment, sports and news. It was a low earth orbit (LEO) satellite and set a basic model for all other communication satellites further. During the 1970s, the global industry has grown up and advancement in satellite communication began to develop. In 1973, the Canadian group successfully distributed video broadcasting over satellite internationally and in 1975, video programming is distributed by HBO to US customers. Commercial and technological use of satellites led to the development of new broadcasting satellites for the mobile environment, video programming, TV programs and launch vehicles. In the year 1990s, satellites became a primary means of distributing TV programs around the world. Due to advancements in satellite communication, the design of innovative antennas has begun to fulfill its requirements, which operate with multiple functions.

In stealth technology, radars are the essential devices to track the targets. The first radar was developed at the time of second world-war used to find large objects like aircraft and ships. In 1933, the first continuous-wave interference radar was developed by Taylor, Young, and Hyland at the Naval research laboratory. Later in 1936, the first pulse radar for antiaircraft fire control is designed by the US army and named as SCR-268. Further, they modified it to SCR-584 microwave radar. In 1939, SCR-270 was developed for the long-range early warning application and later, it is changed to detect echoes from the moon. The existence of pulsed radar made all countries to build their own detectors for different platforms. In the year 1990s, radar system development focuses on military applications, aircraft detection, weather control, air traffic control, remote sensing, and ship safety. Due to these applications of the radar system, novel antenna designs began, which perform multiple functions.

Radar and satellite communications are essential in the modern era due to their plenty of applications, as discussed earlier. In this aspect, an antenna is a critical device in developing multi-functional radars and satellites, so that there is a demand in designing a low profile compact antennas with multiple functionalities.

1.1.2 Antenna systems for mobile and space communications

Beginning of 2G technology in mobile communication, broadcasting satellites, and multi-functional radars in space communication in the year 1990 led to the development of new antenna systems that meets the required specification. Heinrich Hertz experimentally tested the first antenna after the EM wave predicted by Maxwell through theoretical equations. Since then, the requirement in new generation wireless communication grown fast and leads to the design and experimentation of innovative antenna systems.

In the early stage, the large profile antennas like dish antennas, horn antennas, yagi-uda antennas, array antennas, etc., were developed to improve critical parameters like gain, efficiency, axial ratio and bandwidth. The disadvantages of these antennas are; bulky, large size, and more cost to design based on the application requirement. Modern

communication requires antennas to be low profile, compact, easy fabrication, low cost and ease of integration to other devices with multiple functions. Due to these demands, low profile antenna designs such as a microstrip antenna, dipole antenna, microstrip array antenna, dipole array antenna, etc. are developed. Many antenna designs are investigated in the literature with improved performances like wideband, ultra-wideband, circular and dual-polarization, beam steering and scanning, miniaturization and efficiency in new materials (Peixeiro (2012)). Transmitarray, reflectarray, and Leaky wave antennas (LWAs) were also developed based on the application requirement. The new technology era demands the design of innovative antennas, which capable of controlling multiple functionalities like wide bandwidth, polarization control, beam scanning, pattern diversity and radar cross-section (RCS) reduction, sidelobe suppression, low cross-polarization, multiband operation, high gain and better efficiency values.

Diversity in the mobile network and multiple functions in space communication demands novel antenna designs to a specific application. Antenna designer has to put more effort into the design of an antenna due to more constraints and requirements to obtain multiple characteristics. Mobile cell phone requires a low profile antenna with various bands needed to operate for voice and data. The base station requires antennas with wide bandwidth, wide beam-width, and low side-lobes to cover the large area. To set-up a connection to devices like Bluetooth, WiFi, Zigbee, WiMAX and NFC, there is a need for compact antennas with less cost, high performance and easy integration with other circuits. Advancement in MMIC and MEMS technology brings miniaturized antennas to become practically realizable. Low power capability and compactness of these antennas fit in the area of RFID tags, IoT, implantable and on-body wearable communication. Short-range communication requires ultra-wideband antennas because they spread information over a wide range of frequencies with less power. Also, they are used in radar imaging, ground-penetrating radar, and through-wall radar. Navigation system and global positioning system (GPS) nowadays require CP antennas with other functions to find exact locations.

Hence, mobile and space communication provided significant growth in innovative antenna designs that can achieve better performance with multiple functions suitable to

a specific application. Various communication aspects demand particular requirements with ease of integration augment the development of novel antenna systems that meets the need for fast-growing wireless communication.

1.2 Motivation

As we discussed in the earlier section, the requirement of CP antennas depends on the specific application. Due to the increasing demand for high data rates in broadband communication, stealth technology and satellite links, it is required to design CP antennas with various characteristics. The antenna needs to be deployed on high-speed cars, airplanes, trains, etc. Such applications need a compact, low profile, wideband and high gain antennas, which can be easily integrated into the systems. In the future, millimeter-wave communication and small satellite communication (microsat, nanosat, CubeSat) require wideband, multi-band and high gain CP antennas with excellent beam scanning capabilities. In 5G mobile and terahertz communication, there is a requirement of low cost miniaturized CP antennas that can be integrated into small devices. Conventional methods are failed to maintain CP over wide bandwidth or in multiple bands. Many CP techniques are available in the literature, such as slit and stub loading methods, introducing multiple slots, modifying feed and designing of the feeding mechanism. Since two orthogonal modes are required with equal magnitude and 90° phase to produce CP wave, it is strenuous to maintain phase over wide bandwidth or multiple bands. Even single feed CP antennas are challenging to design with various functionalities. These requirements of CP antennas motivated us to further research on CP antennas with RCS reduction, high gain, wideband, and multi-band operation.

To achieve the required functionalities of antennas such as CP with wideband property, multi-band characteristics, high gain, RCS reduction, better radiation efficiency, and cross-polarization level, Metamaterials (MTMs) are the best candidate to attain these multiple characteristics. The integration of MTMs to antenna structure led to the design of new CP antennas with desirable functionalities and tuning capabilities.

In general, MTMs are defined as artificial and effectively homogeneous electromagnetic structures with anomalous properties not readily found in nature. An effective homogeneous subwavelength periodic structure has guided wavelength much higher than its average cell size. MTMs are a new research area that can be found from literature to design special functions like negative refractive index, Zero refractive index, MTM cloaking, imaging and lenses. All of these are difficult to achieve by naturally occurring materials. By suitably designing structures and carefully controlling surface waves and current distribution, many functionalities can be achieved. In the recent era, keen interest has been developed on 2D planar structures of MTMs called metasurfaces(MTSs). These MTSs produce similar functionalities like MTMs, except that they are more comfortable to fabricate, thin, and negligible losses. Many CP antennas are designed using MTSs that are found in the literature, which uses phase modification to engineer the wavefront of EM waves. Also, split-ring resonators are potential candidates to use with antenna designs to achieve multi-band characteristics with tuning effect due to their permeability effect.

1.3 Problem Definition

Linearly polarized (LP) antennas fail to meet the challenges of mobile and space communication due to their disadvantages. Circularly polarized (CP) antennas have more advantages than LP antennas in-terms of device orientation, immune to Faraday's rotation effect, fading channels, environmental effects, polarization losses, multi-path interference, etc. It is challenging to achieve circular polarization with multiple functionalities without affecting other requirements. Stealth technology requires low RCS antennas with CP property. Mobile communication requires wideband CP antennas to accommodate the maximum number of users. Also, CP antennas are needed to operate in multiple bands at a time. Small satellite communication needs high gain CP antennas to design CubeSats, nanosats, and navigation systems. Although previous literature has these types of antennas, there is a gap that needs to be filled in developing a low profile, RCS reduction, Gain improvement and wideband operation along with polarization

conversion. Literature survey fulfills some of these demands satisfactorily by various designs and optimization techniques using the current state of the art technology.

1.4 Objectives

Formulated objectives are:

- To design a compact and low profile circularly polarized antenna with RCS reduction capability over the impedance bandwidth.
- To develop an antenna that provides circular polarization over a wide bandwidth with stable gain for wireless applications.
- To design an antenna which offers high gain and linear to circular polarization conversion capability useful for satellite applications.
- To design a multiband circularly polarized antenna with independent control of each resonance frequency and their polarization states as required at each band.

1.5 Methodology

Extensive properties of MTMs and MTSs are used to achieve the proposed objectives.

Method adopted to obtain the desired characteristic of each design is described below.

Proposed models are simulated, fabricated and measured using facilities available at the lab.

- A CP antenna is designed using a compact and low profile rectangular patch-based MTS. A source free characteristic mode analysis is used to analyze the proposed MTS, which produces CP. It describes the exact modes which are contributing to CP. Modal significance and characteristic angle give information about orthogonal modes that are required to achieve CP. A slot antenna is utilized as an essential source to excite the orthogonal modes generated by MTS. Absorptivity property of MTS is analyzed to achieve RCS reduction in the entire impedance bandwidth.
- Backside radiation produced by the primary sources like slot antennas is reduced by utilizing zero phase reflective property of an artificial magnetic conductor (AMC). A CPW fed truncated slot is designed, which produces two orthogonal modes which are degenerative to achieve wide CP bandwidth. Further, gain

and CP bandwidth enhancement of truncated slot antenna is done by using an array of frequency selective surface (FSS), which is placed below the slot antenna. FSS structures improve the radiation in broadside direction, thus enhancing the gain when they put below primary sources. FSS array has a reflection phase such that it increases slot antenna CP bandwidth when the reflected wave from FSS combines with the forward wave of the slot.

- In general, the gain of any primary sources are less and they produce linearly polarized wave. An effort is made to increase the gain of LP antenna with the conversion of a linearly polarized wave into a circularly polarized wave using the zero-index property of MTS. The Zero-refractive index property focuses energy towards the intended direction, thus enhancing the gain. Polarization conversion is analyzed using transmission coefficients of MTS unit-cell. The constitutive parameters are extracted to justify unit-cell and MTS characteristics. MTS is placed at an optimum height above the LP antenna to achieve good gain and axial ratio.
- To design a multi-band CP antenna, a slot antenna is loaded with MTM elements, such as a split-ring resonator(SRR). CP resonance band of the slot antenna is not altered due to the loading of these structures. The additional CP frequency bands are achieved due to the excitation of SRRs placed on the slot. The triple CP bands are obtained with its compact size. The resonances of each frequency band can be controlled independently by selecting the optimum slot and SRR dimensions. Proper placement of SRRs on the slot antenna provides better coupling and resonance characteristics.

1.6 Organization of the Thesis

The goal of thesis is to design and implement wideband, multiband and high gain CP antennas using the extensive properties of MTMs. This thesis is organized into several chapters based on the various designs proposed and obtained results. Introduction section of the thesis describes various communication systems, their evolution and antenna systems. Motivation to design innovative antennas is presented, followed by problem formulation. The objectives, work methodology and thesis organization are provided in the separate sections.

The second chapter discusses the basic concepts of circular polarization, advantages and disadvantages. Also, a brief explanation of MTMs, MTSs and split-ring resonators are discussed, which are used to develop wideband, multi-band, and high gain CP an-

tennas. Also, it provides a brief explanation of the modal analysis, which helps us to understand the mode concept to obtain CP characteristics. A brief literature survey is included in the next section. The first section of the literature survey gives modal analysis and its contribution to design various types of antennas. Also, it gives an existing work on radar cross-section(RCS) reduction in antennas. The upcoming sections describe the literature works on wideband, high gain and multi-band CP based designs.

In the third chapter, a modal analysis of metasurface design to achieve CP characteristics is discussed. It gives a basic understanding of mode concepts to identify and excite orthogonal modes to produce CP wave. Also, the RCS reduction capability of MTS is estimated by utilizing the absorptive property of MTS. A plane wave is incident on the MTS to calculate its absorptivity. A compact antenna structure is designed and experimentally verified in-terms of impedance and axial ratio bandwidth with good gain and efficiency values.

The fourth chapter provides the design and investigation of two wideband CP antennas. In the first design, a truncated slot antenna is presented to achieve two orthogonal modes to obtain CP wave. Further to improve axial ratio bandwidth and gain of the truncated slot antenna, the reflective property of frequency selective surface (FSS) is utilized. The reflection phase of the FSS unit-cell has been analyzed for TE and TM polarization. The second design achieves wide axial ratio bandwidth using combined resonances of truncated slot and rotated split-ring resonator(SRR). The corner truncated slot antenna provides lower CP resonance and SRR gives higher CP resonance. The proposed structure is fed by CPW technique. Since it is a single layer design, it is used for soil moisture sensing applications.

In the fifth chapter, two high gain CP antennas are designed and validated. In the first design, the gain of a CP patch antenna is enhanced using the zero-index property of MTS. Reflection and transmission coefficient of designed unit-cell is analyzed. Constitutive parameters are extracted through an algorithm using scattering parameters of the unit-cell. According to snell's-law, zero-index based MTS focuses the energy normal to its interface without any phase variations, thus enhancing the gain. In the

second design, a unit-cell is designed to enhance the gain as well as polarization conversion. An optimum height is selected to place the MTS atop of the LP patch antenna to improve the gain and convert the LP wave into CP wave.

The sixth chapter discusses multi-band CP antennas. A dual-band and a tri-band CP antennas are designed and validated. In the first design, a slot antenna loaded with asymmetric cross strips is presented to obtain dual-band CP characteristics. The corner truncated slot produces two orthogonal degenerate modes, which gives lower band CP resonance, and asymmetric strips produce upper band CP resonance. The second design provides triple CP bands with independent control of each resonance frequencies. The corner truncated slot antenna achieves CP in the first resonance band. The second CP resonance band is due to a rotated SRR loaded on the slot antenna. The inner ring of SRR is rotated 90^0 with respect to outer ring generate orthogonal electric field produces CP. The SRR, which has multiple split gaps, is placed on the other diagonal corner of the slot antenna produces third band CP resonance. All bands are independently controlled by their dimensions and split gaps.

The seventh chapter gives conclusions about the contributions provided through different designs in the thesis. Also, it discusses future scope to develop antennas with improved performances for future 5G applications.

CHAPTER 2

BACKGROUND AND LITERATURE SURVEY

2.1 Circular polarization

In electromagnetic theory, polarization is defined as the direction of the electric field with respect to the wave propagation direction. Polarization types are elliptical, linear and circular polarization. An LP time-harmonic wave possesses electric field vector always oriented in a straight line in space. A CP wave at a given point in space traces a circle by its electric field vector. To produce CP wave, two electric field components are required with equal magnitude and quadrature-phase between them. If the electric field vector of a time-harmonic wave traces an ellipse at a given point in space is said to be elliptically polarized. Fig. 2.1 shows polarization ellipse ([Steven Gao and Zhu \(2014\)](#)). LP and CP are two extreme cases of elliptical polarization. Axial ratio (AR) is used as a parameter to measure polarization. If we consider polarization ellipse, the axial ratio is the ratio of the major axis to the minor axis. AR is between 1 to ∞ , and it is also expressed in dB scale. A pure circularly polarized wave possesses a 0 dB axial ratio. Since it is impractical to achieve absolute circular polarization, a range of frequencies over which the AR < 3 dB is considered.

$$AR = \frac{\text{Major axis}}{\text{Minor axis}} = \frac{a}{b} \quad (2.1)$$

Consider the plane wave propagating in +z direction, its time harmonic electric field vector at z=0 is given by,

$$E = E_x \cos(\omega t)a_x + E_y \cos(\omega t + \delta)a_y \quad (2.2)$$

Polarization can be easily understood by equation (2.2). Electric field components E_x and E_y are directed along x and y direction and phase difference between E_x and E_y

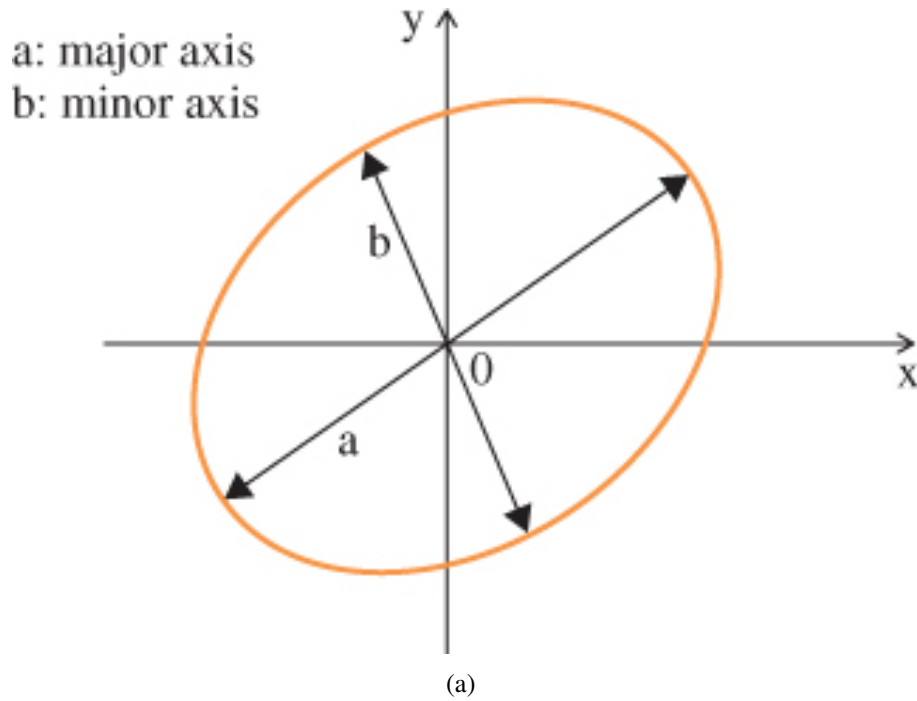


Figure 2.1: Polarization ellipse plotted as a function of time and traced at a position in space.

component is δ . If $\delta=0$, then wave exhibit linearly polarization. If the component $E_x \approx 0$, then it is vertically polarized and if $E_y \approx 0$, then it is horizontally polarized. When E_x and E_y are not equal and $\delta=45^\circ$, then wave is linearly polarized at an angle and it is given by,

$$\gamma = \tan^{-1} \frac{E_y}{E_x} \quad (2.3)$$

Circular polarization (CP) is obtained when E_x and E_y are equal and their phase difference is 90° . If wave propagation is in $+z$ -direction and rotation of the electric field vector is in a clockwise direction, then the wave exhibit a left-hand circular polarization(LHCP). If the electric field vector rotates in an anti-clockwise direction, then the wave produces right-hand circular polarization(RHCP).

2.1.1 Advantages of CP antennas

Multipath interference mitigation: A CP wave changes its polarization due to multiple reflections caused by the environment like raindrops, buildings, trees, etc. LHCP

wave is changed to the RHCP wave and vice-versa. The reflected wave is filtered out, and the directed wave is received. This mitigation in multipath interference is helpful in space communication and mobile environment, which requires higher data rates.

Faraday's Rotation effect: Plane of polarization is changed due to the interaction of light and magnetic field in space. This effect is called Faraday's rotation effect. Circularly polarized antennas are immune to these effects due to the rotation of the field vector. This effect is predominantly low in higher frequencies than lower frequencies. LP antennas are more affected by this effect and are undesirable due to the misalignment of polarization.

Polarization misalignment: The LP antennas suffer from Faraday's rotation effect, so to receive signal efficiently, LP transmitting and receiving antennas must align in the line of sight. This alignment is not required in CP antennas. An LP antenna experiences 3dB loss if it receives an ideal CP wave irrespective of the orientation. This property is useful in mobile applications and RFID systems, as it gets signals regardless of its orientation

It is worth designing CP antennas due to their advantages, which operate with multiple functionalities. To design an antenna that produces CP wave, two modes with equal magnitude are excited with a 90° phase difference. Many CP antennas are designed using power divider, multiple feeding techniques and also modified antenna geometry. The CP antennas with single feed are essential in modern communication due to their easy integration with other circuits. It is most challenging to design a wideband and multi-band CP antennas with a single feeding technique. Conventional methods of designing antennas are failed to meet these challenges of space and modern wireless communication. To achieve these requirements in the recent era, metamaterials(MTMs) attracted more interest in antenna design with multiple characteristics. Hence, there is a demand for circularly polarized antennas that meets the requirement of present mobile and space communication. These designs substantially reduce environmental effects and can be easily integrated into satellite and radar communication that has more impact on the outside environment. The focus of this thesis is to design CP antennas that fill some of the research gaps required by present mobile and wireless communication.

2.2 Introduction to Metamaterials

MTMs are periodic arrangements of sub-wavelength engineered materials, which exhibit electromagnetic properties that are not found in natural substances. J.C Bose first explored the concept of artificial materials in 1898 on twisted structures(J.C.Bose (1898)), which are mostly called chiral media in the present scenario. Later in 1905, backward wave propagation is suggested by Lamb(Lamb (1904)). Then in 1967, a Russian physicist Viktor Veselago(Veselago (1968)) shown the existence of left-handed substances. These substances exhibit simultaneous negative permeability and permittivity properties. The material medium plays a key role in the propagation of the EM wave. The materials are classified based on their effective parameters called effective permeability and permittivity, as shown in Fig.2.2(Caloz and Itoh (2005)). In the figure, the first quadrant represents right-handed (RH) materials, which support forward wave propagation and the third quadrant represents left-handed (LH) materials, which exhibit backward wave propagation. In the second and fourth quadrant, wave decays exponentially with time as it propagates through a medium. Here the exciting fact is that LH materials exhibit unusual properties like negative refraction, MTM cloaking, a reversal of Doppler effect, the reversal of Vavilov-Cerenkov radiation, etc. Negative refraction is illustrated in Fig.2.3. Such materials can be incorporated into antennas with suitable structural modifications to obtain multiple characteristics.

As suggested by Veselago, LH materials are not natural substances, but they are an artificial homogeneous structure(Pendry (2000)), which was experimentally demonstrated by J.B.Pendry and Shelby et al. (Shelby et al. (2001)) at University of San Diego. Pendry introduced a plasmonic type positive- μ /negative- ϵ and negative- μ /positive- ϵ structure shown in Fig.2.4. These structures have guided wavelength λ_g much greater than the average cell size. This condition should be satisfied when propagation in MTMs dominates over scattering/diffraction. Thin metal wires are shown in Fig.2.4(a) exhibits negative- ϵ /positive μ . When an electric field (E) is incident parallel to the metal wire axis, it induces current and generates equivalent dipole moments. This MTM exhibits

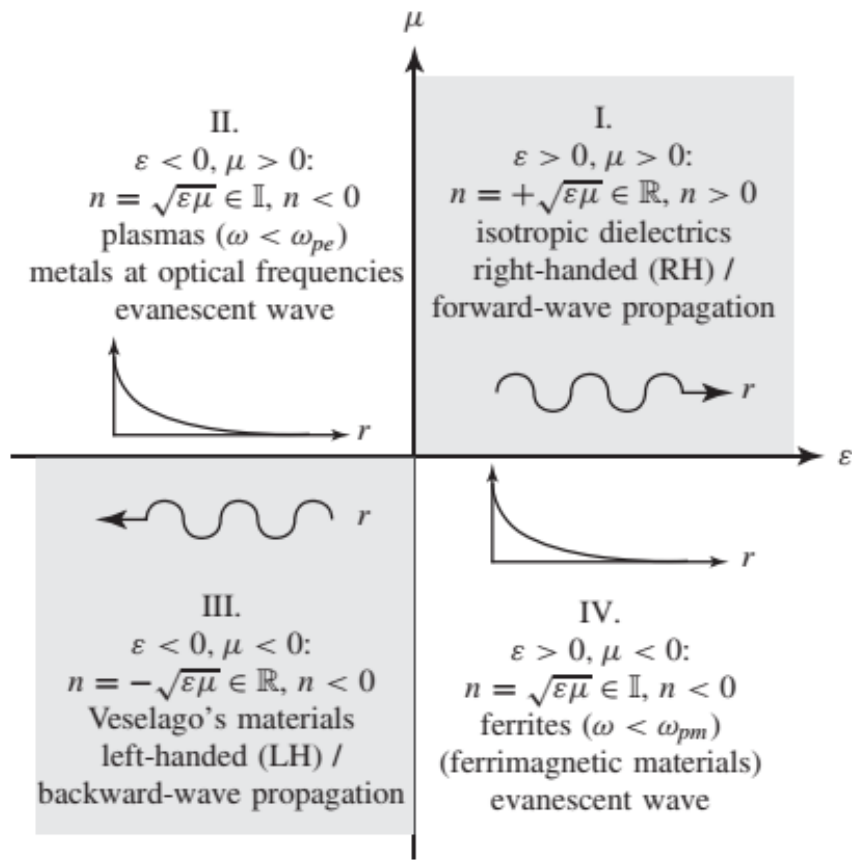


Figure 2.2: Material classification based on permeability- permittivity and refractive index (Caloz and Itoh (2005))

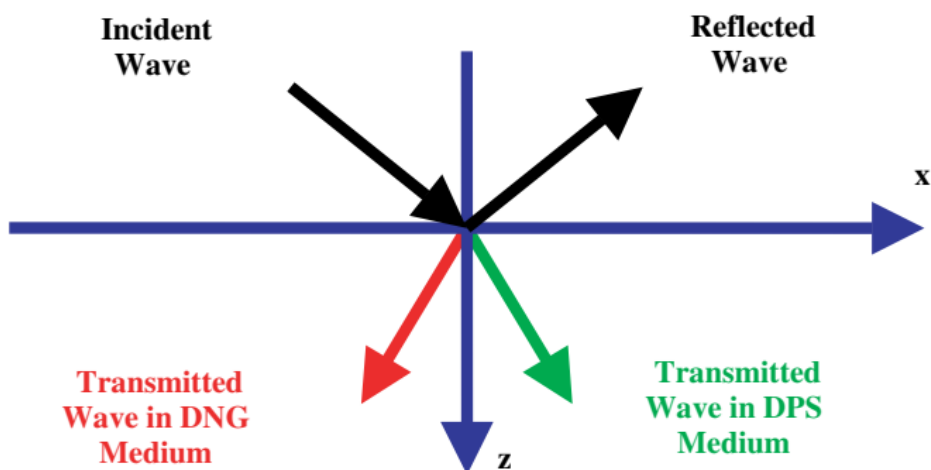


Figure 2.3: Negative refraction(Engheta and Ziolkowski (2006))

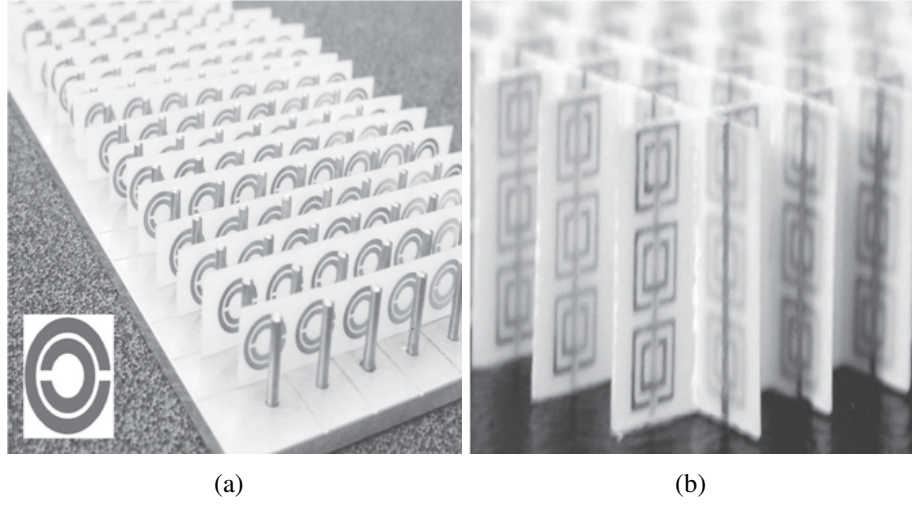


Figure 2.4: First experimented LH materials consists of Thin wires and split ring resonators (a) LH structure with single dimension (b)LH structure with two dimension(Caloz and Itoh (2005)).

the plasmonic type permittivity function vary with frequency and it is in the form

$$\epsilon_r(\omega) = 1 - \frac{\omega_{pe}^2}{\omega^2 + j\omega\zeta} \quad (2.4)$$

where, $\omega_{pe}^2 = \sqrt{\frac{2\pi c^2}{p^2 \ln(p/a)}}$ (c is speed of light and a is wire radius) is the electric plasma frequency and $\zeta = \epsilon_0 \frac{p\omega_{pe}^2}{\pi\sigma}$ (σ :conductivity of metal) is damping factor due to metal losses.

$$Re(\epsilon_r) < 0, \text{ for } \omega^2 < \omega_{pe}^2 - \zeta^2 \quad (2.5)$$

which reduces if $\zeta=0$ to

$$\epsilon_r < 0, \text{ for } \omega < \omega_{pe} \quad (2.6)$$

Since the magnetic dipole moment is not generated, permeability becomes $\mu=\mu_0$. The assumption is that metal wires are not greater than the wavelength, meaning that the first resonance of wires is far away from the frequency of the exciting wire.

The metal planar split-ring resonator(SRR) gives negative μ /positive ϵ , as shown in Fig.2.4(b). The metal rings are excited by the magnetic field (H), which is incident orthogonally to its plane of rings. The incident magnetic field produces an equivalent

magnetic dipole moment due to current flow in the loop of SRR. The plasmonic type of permeability frequency function exists in this structure, and it is given by,

$$\mu_r(\omega) = 1 - \frac{F\omega^2}{\omega^2 - \omega_{0m}^2 + j\omega\zeta} \quad (2.7)$$

where, $F = \pi(a/p)^2$ is a magnetic resonance and its frequency tunable to GHz range. (a: smaller ring inner radius), $\omega_{0m} = c\sqrt{\frac{3p}{\pi \ln(\frac{2wa^3}{\delta})}}$ (w : width of the rings; δ : radial separation between the two rings), $\zeta = 2pR'/a\mu_0$ is damping factor due to metal losses (R' : metal resistance per unit length). It is worth to note that SRR does not include the magnetic conducting material but resonance occurs due to artificially generated magnetic dipole moments. From equation(2.4) it reveals that the frequency range exists for $\text{Re}(\mu_r) < 0$, in general ($\zeta \neq 0$).

$$\mu_r < 0, \text{ for } \omega_{0m} < \omega < \frac{\omega_{0m}}{\sqrt{1-F}} = \omega_{pm} \quad (2.8)$$

where, ω_{pm} is called as magnetic plasma frequency.

2.2.1 Split Ring Resonator

In 1999, Pendry et.al (Pendry (2000)) developed micro-structured artificial materials exhibiting strong magnetic properties. When fields and currents are oriented along the wire axis, they obtained the expressions in which wires resemble the magnetic property of artificial material. For this work, they concluded that materials such as wires are diamagnetic and their permeability value approaches to the value of free space when wire radius is decreased. The response obtained is resembled like artificial dielectrics. Different behavior is observed in cylinders, which are structured like a parallel plate capacitor. Then the same is reduced to a planar form and termed as a split ring resonator(SRR), as shown in Fig.2.5(Eleftheriades and Balmain (2005)). This structure exhibits a strong electric field and large capacitance between the rings. Magnetic field (H) orthogonal to the plane (conventional axis) of rings induces currents on the rings. The capacitance between rings and inductance due to currents on cylindrical structure

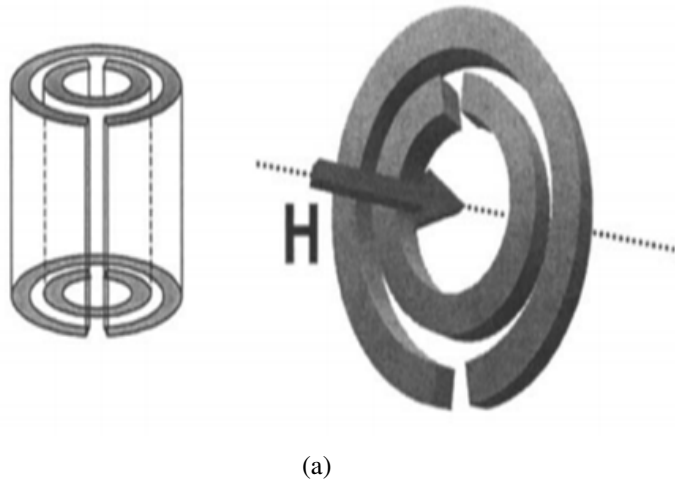


Figure 2.5: The structure of split ring resonator (SRR) in cylindrical form and planar form discovered by Pendry. The magnetic field is induced orthogonal to the plane (conventional axis) of rings

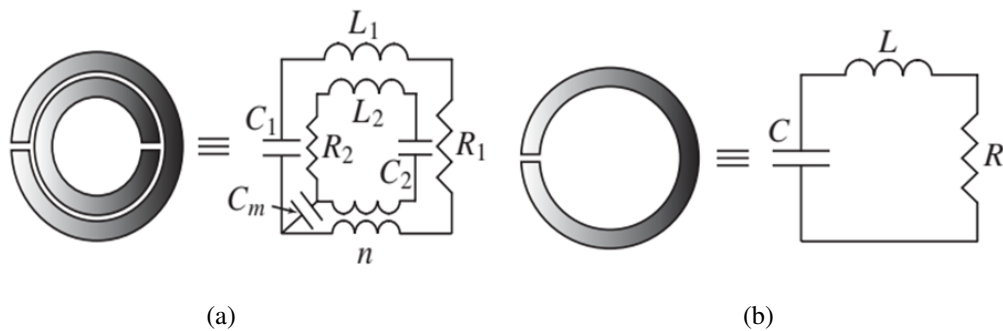


Figure 2.6: Equivalent circuits of SRRs. (a) Double loop SRR configuration (b) Single loop SRR configuration (Caloz and Itoh (2005))

results in a resonant behavior of SRR. Later this discovery of SRR was experimentally demonstrated by Shelby et al. in (2001) where L is the inductance provided by the rings and C is the capacitance between rings. Fig.2.6 shows the SRR's equivalent circuit. The single ring configuration is a simple RLC resonator. In double ring configuration, the inductive and capacitive coupling between smaller and larger rings is modeled as a transformer ratio n and coupling capacitance (C_m), respectively. The double ring configuration essentially becomes equal to a single ring configuration when the weak coupling

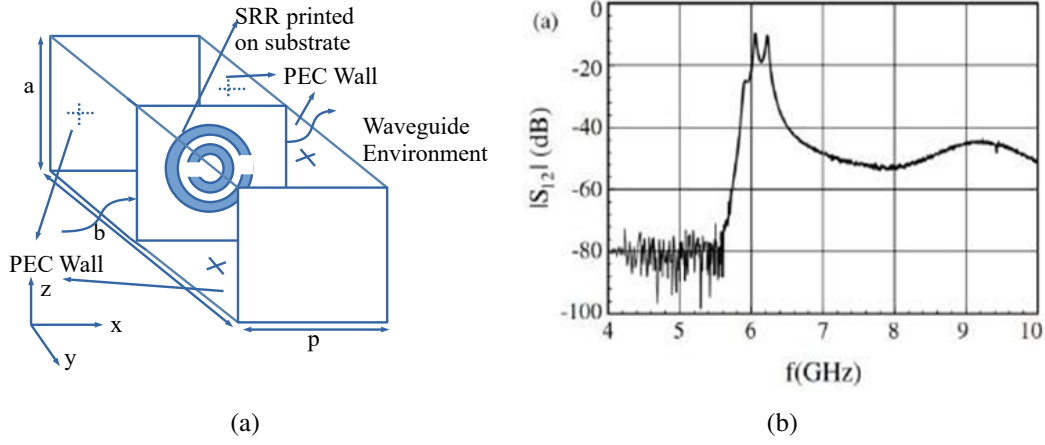


Figure 2.7: Experimental set-up to realize SRR behavior in a hollow metallic waveguide. (a) Simulation set-up (b) Transmission coefficient magnitude (Marqués et al. (2002))

exists between the rings. The resonant frequency is given by,

$$\omega = \frac{1}{\sqrt{LC}} \quad (2.9)$$

Fig.2.7 shows the experimental set-up of SRR. An SRR is etched on the substrate material and the dispersive nature of waveguide can be used to characterize the LH materials. It is the fact that a hollow metallic waveguide supports TE and TM mode propagation with its dispersion relation given by,

$$k = \omega \sqrt{\mu_r \epsilon_{eff}} \quad (2.10)$$

where k is the propagation constant, ω is the angular frequency, μ_r is the magnetic permeability of substrate, and ϵ_{eff} is the effective dielectric constant given by

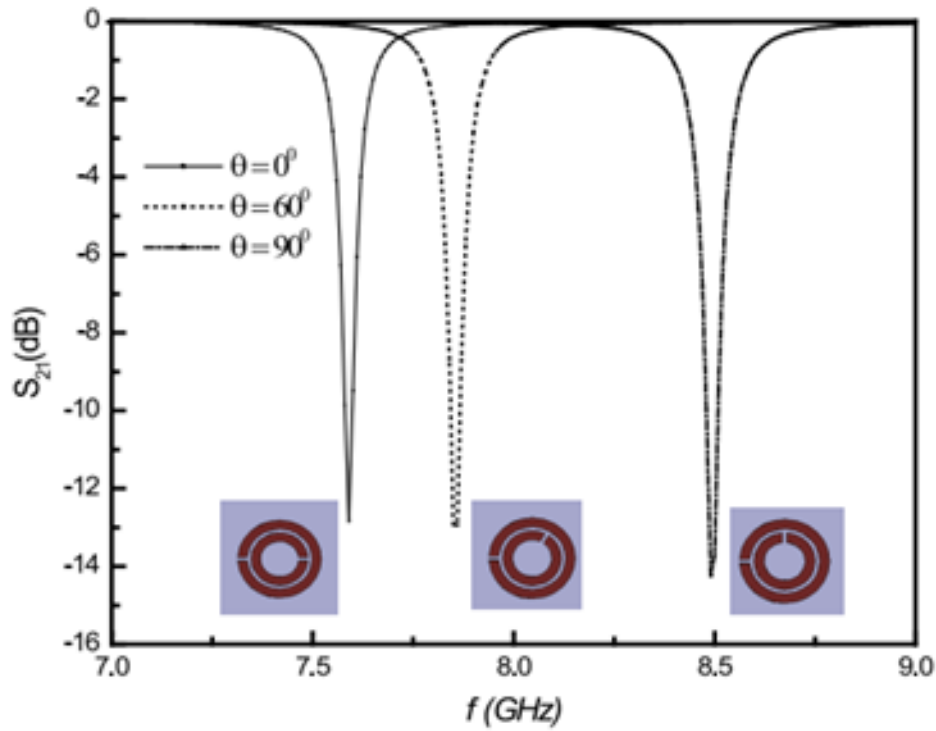
$$\epsilon_{eff} = \epsilon_r \left(1 - \frac{\omega_0^2}{\omega^2}\right) \quad (2.11)$$

with ω_0 being the cut-off frequency for the considered mode and ϵ_r the dielectric permittivity of the substrate.

An SRR is embedded inside waveguide and EM wave is impinging parallel to the

direction of the x-axis is shown in Fig.2.7(a). SRR introduces the negative permeability effect to obtain LH behavior. To enhance the interaction of SRR with the EM field, SRR should be placed inside waveguide in the y-direction with a spacing between the SRRs equal to the waveguide lateral side walls dimension. The fundamental mode resonance frequency of the waveguide should be greater than the operating frequency of SRR, to ensure the resonance occurs due to SRR when the negative permeability effect co-exists with negative dielectric permittivity. Fig.2.7(b) shows the transmission property of SRR embedded in a waveguide, which has a cut-off frequency of 25 GHz. The resonance at 6.2 GHz shows the existence of the LH nature of SRR due to its negative permeability effect.

In the earlier section, it is mentioned that SRR is a resonating structure with its equivalent parameters L and C. By varying the value of L and C, the negative permeability effect can be varied, and resonance can be tuned. In work by [Saha and Siddiqui \(2012\)](#), the SRRs are rotated by an angle and the effect of resonance is studied. The



(a)

Figure 2.8: Transmission coefficient of circular SRR as a function of rotation angle θ of inner ring([Saha and Siddiqui \(2012\)](#))

SRR which has a conventional axis, the gaps lie in the same axis so that the capacitance between lower and upper half rings are equal. When the angle θ between two split gaps of the rings is changed, then the resonance changes due to change in the capacitances on the lower and upper half rings of SRR. The resonance effect due to the change in capacitances by rotating the inner ring of SRR is shown in Fig.2.8. This effect can be utilized to control the SRR resonance to the desired frequency. The rotation effect of SRR can be used to achieve CP and polarization sense. Also, the multiple gaps can be created in the SRR to control SRR resonance to the required frequency. The multiple splits in the SRR produce additional capacitive effects which change the effective negative permeability region and shifts the resonance to a higher value. The work proposed by Evren Ekmekci et al. (Ekmekci et al., 2009) investigated the conventional SRR with multiple slit SRR(MSSRR) configuration. The different unit cells are analyzed with single and multiple slit configuration with their transmission characteristics. Fig. 2.9 shows the conventional SRR and multi-slit SRR configurations. The measured and simulated transmission characteristics of conventional SRR and MSSRR is shown from Fig.2.10-2.12.

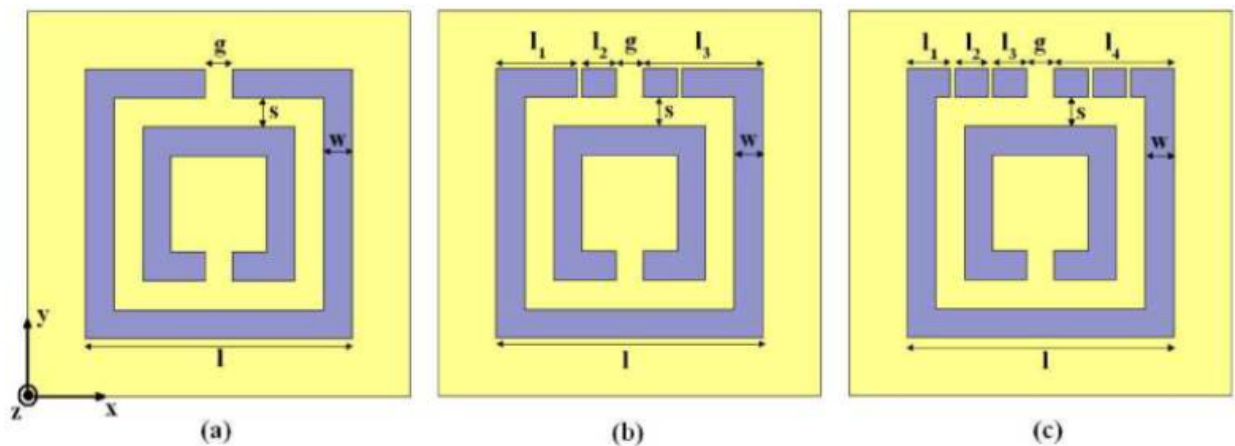
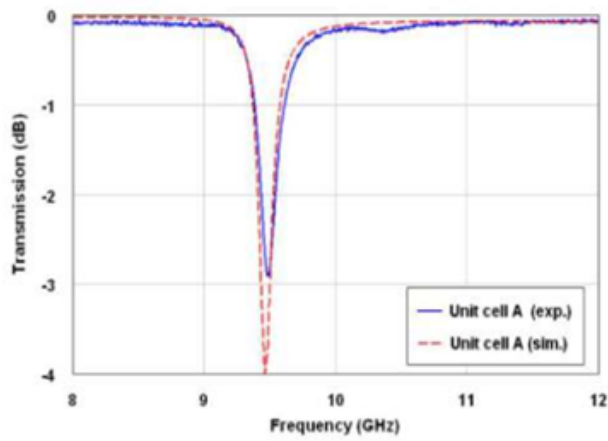
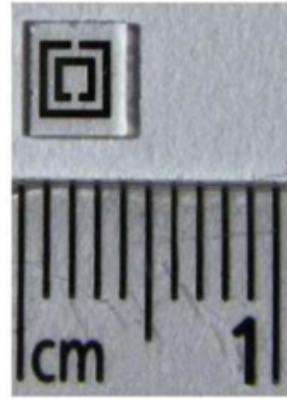


Figure 2.9: Structure of different SRRs (a)Unit cell A (b) Unit cell B (c) Unit cell C(Ekmekci et al. (2009))

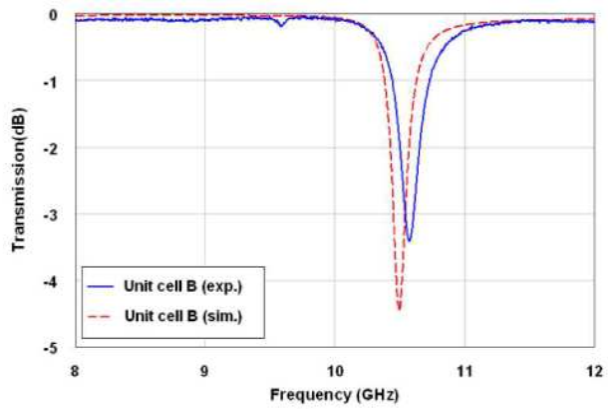


(a)

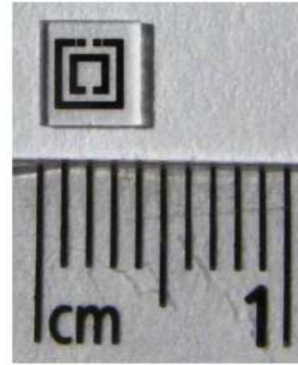


(b)

Figure 2.10: (a)Transmission coefficient of unit cell A (b) its photograph

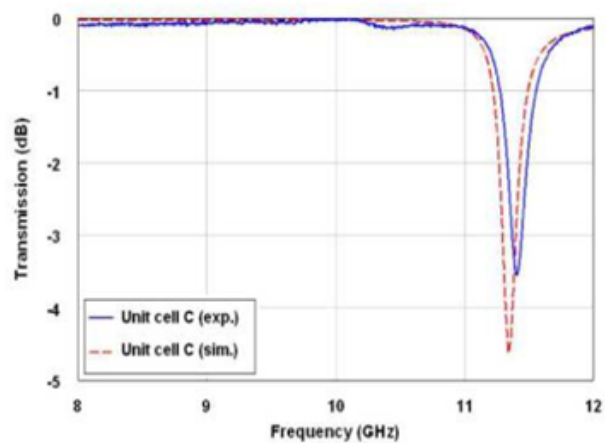


(a)

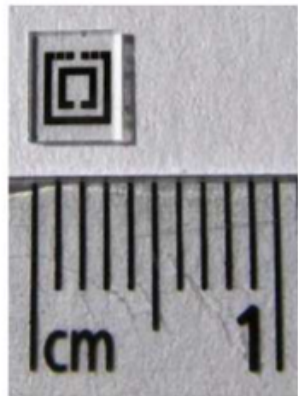


(b)

Figure 2.11: (a)Transmission coefficient of unit cell B (b) its photograph



(a)



(b)

Figure 2.12: (a)Transmission coefficient of unit cell C (b) its photograph

2.2.2 Metasurfaces

Metasurface(MTS) is the particular class of MTM, which consists of planar arrays of densely packed sub-wavelength elements, which are optically thin and nearly resonant structures. MTSs possess useful and unusual properties of their constitutive elements with resonant behavior. The resonant elements have periodicity to control EM transmitted and reflected waves(Chen et al. (2016a)). MTSs are promising solutions to develop the devices in the Microwave and optical domain. Some of the potential Functionalities of the MTSs are Frequency Selective Surfaces(FSS), Electromagnetic Band Gap(EBG)

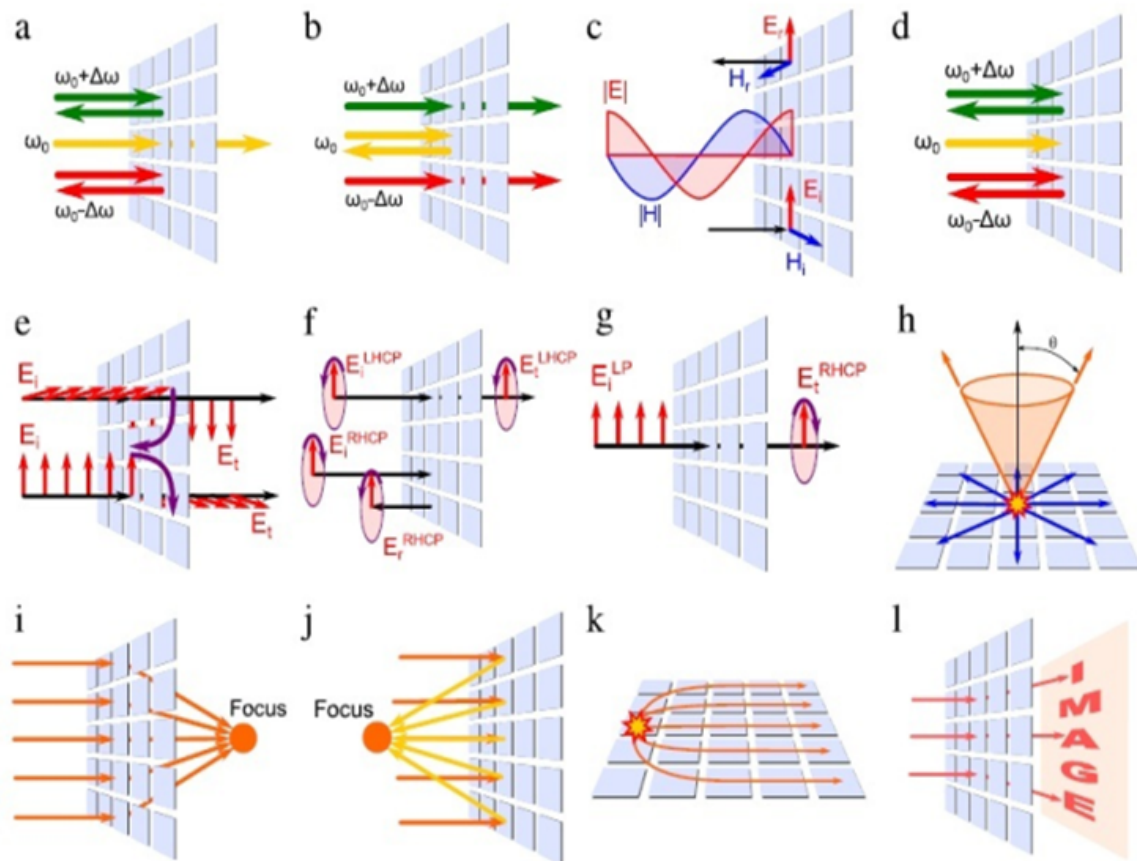


Figure 2.13: Metasurface functionalities: (a) bandpass frequency selective surface (b)bandstop frequency selective surface (c) high-impedance surface (d) narrowband perfect absorber(e) twist polarizer (f) right-handed circular-polarization frequency selective surface (g) linear to circular polarization converter (h) two-dimensional leaky-wave antenna with a conical-beam pattern (i) focusing transmitarray; (j) focusing reflectarray (k) flat Luneburg lens (l) hologram.(Glybovski et al. (2016)).

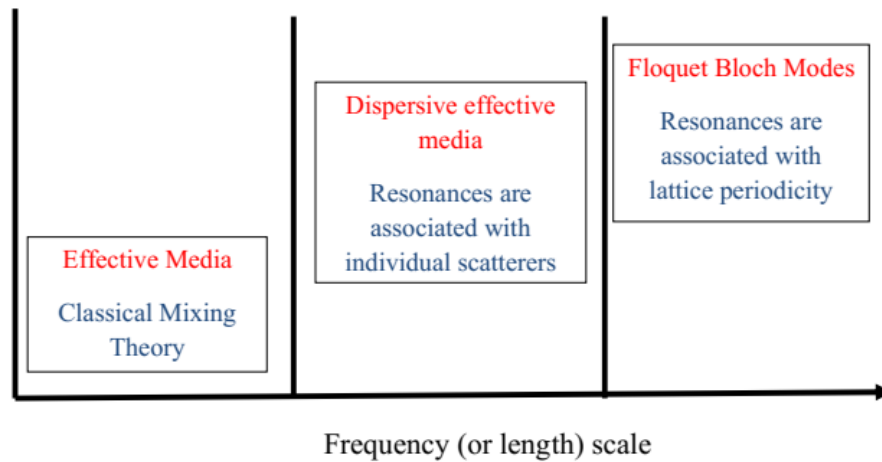


Figure 2.14: Three regions of a composite material characteristics (Holloway et al. (2012)).

structures, Absorbing surfaces, High Impedance Surfaces(HIS), Polarization twister, optical lenses, linear to circular Polarization Converter, etc. Some of the applications of MTSs are shown in Fig.2.13. When the wavelength becomes comparable to the period of the scatterer, then the fields are no longer see the composite as an effective medium due to its resonance behavior. Fig.2.14 shows the EM behavior of periodic structures with respect to the frequency region. In the figure, region 1 corresponds to quasi-static behavior. It implies that the period of the scatterer is comparable to the wavelength at low frequencies so that it induces the permanent dipole moments. These structures are similar to traditional materials used to achieve some specified behavior. In this region, the effective parameters are obtained using conventional mixing formulas. The region 2 corresponds to the effective dispersive medium where the scatterer is small compared to the wavelength. These small scatterers in this region behave as an individual resonant structure so that the array of scatterers can be realized as MTMs, and their characteristics give multiple EM behavior that is not found in nature. In this region, the array of scatterers becomes dispersive in nature, but it is possible to characterize the EM behavior by extracting the effective parameters of the single scatterer. Region 3 corresponds to the same array of scatterers called MTSs, where the scatterers are subjected to higher-order floquet Bloch mode analysis to study its EM behavior. In this region,

the structure is no more a composite material behaving as an effective medium. Since the wavelength is approaching the period of the scatterer, the higher-order modes must be considered in the EM analysis.

2.2.3 Frequency Selective Surface(FSS)

The FSS is a particular class of MTM, and it is periodic to obtain specific reflection and transmission property. The FSS finds applications in stealth and aerospace technology as an absorbing medium or reflecting surface(Munk (2000)). Also, FSS is used in low observable platforms to enhance the characteristics of an antenna like gain, bandwidth and radar cross-section(RCS) reduction. The FSS structures are categorized into two types based on the periodic structure of the geometry. The periodic patches are etched on the substrate called capacitive FSS and the substrate with metallic ground comprises of apertures called inductive FSS. The specific spectrum is selected by the careful design of these periodic structures. Fig.2.15 shows some of the FSS structures. Reflection and transmission properties of FSS are analyzed using lumped elements L and C approach. The analysis is carried out for different configurations like freestanding FSS with normal incidence and fixed periodicity. In general, the study is carried out for FSS with thin and thick dielectric slabs. The oblique incidence and variable periodicity are considered for FSS with dielectrics. For freestanding FSS, the analysis is valid till the frequency of interest, in which grating lobes occur($d=\lambda_g$ for normal incidence and $d=\lambda_g/2$ for grazing incidence). This is because the reflected or transmitted energy in other directions is also considered rather than the direction stated in snell's law resulting in a non-linear behavior of periodic structures. Under some assumption, a capacitive FSS is analyzed and its simple LC network can give its frequency response. Similarly, for an inductive FSS, a series LC network can provide the frequency response. A more straightforward approach can determine the impedance of FSS by finding the complex reflection coefficient by full-wave simulations and it is given by,

$$Z_{FSS} = \frac{Z_0^2(1 + \Gamma)}{2Z_0\Gamma} \quad (2.12)$$

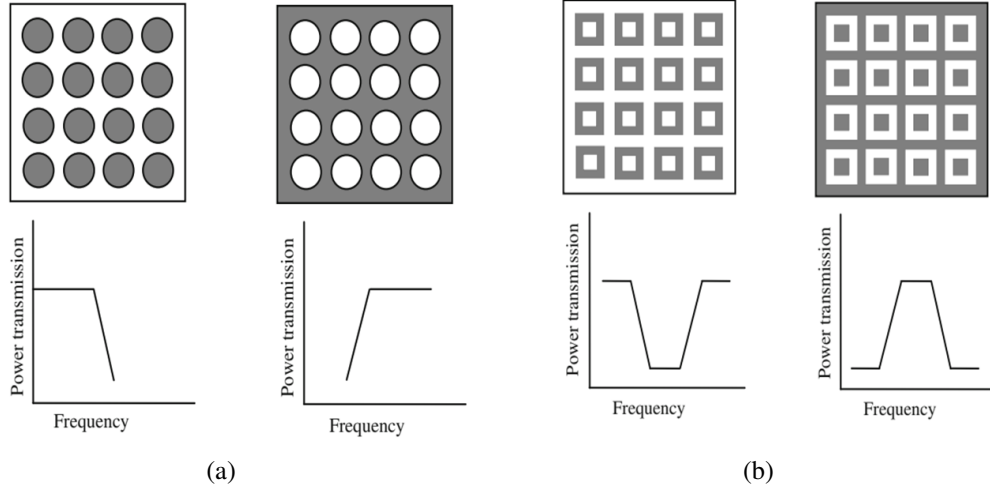


Figure 2.15: (a) array of circular metallic patches and array of circular apertures (b) array of square metallic loops and array of square aperture rings

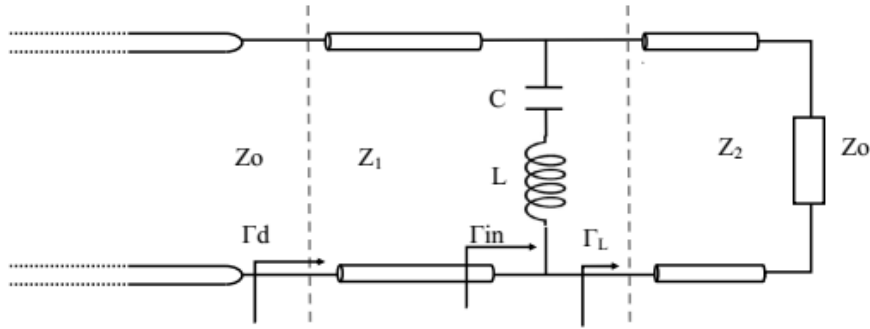


Figure 2.16: The transmission line model of frequency selective surface embedded in two dielectrics(Costa et al. (2012)).

Here, FSS is used along with a dielectric substrate and it is required to analyze the behavior of FSS with the dielectric substrate. Also, if an FSS is embedded within two dielectrics, an additional transmission line is considered while retrieving LC parameters. Fig.2.16 shows the model of an FSS embedded in two dielectrics.

The reflection coefficient Γ used in equation (2.12) is to compute the impedance of FSS and it is determined as,

$$\Gamma_{in} = \frac{Z_0(1 + \Gamma_d) - Z_1(1 - \Gamma_d)}{Z_0(1 + \Gamma_d) + Z_1(1 - \Gamma_d)} e^{i2\beta_1 d} \quad (2.13)$$

where Γ_d is the input reflection coefficient computed by method of moment (MOM)

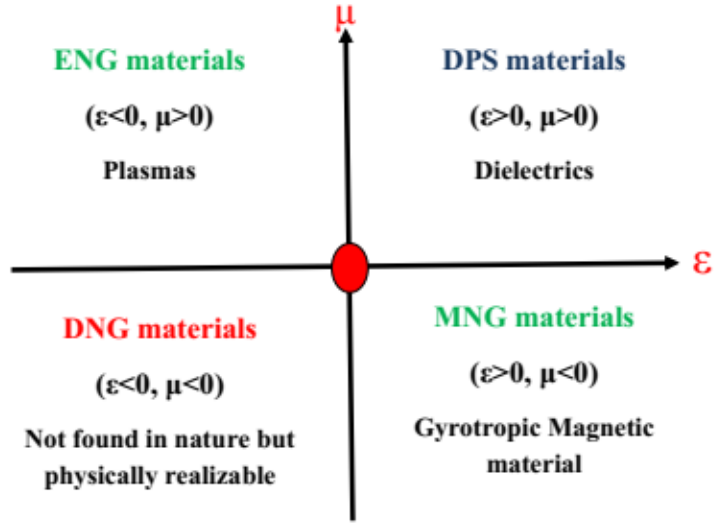
analysis. All other parameters are depicted in Fig.2.16. After finding the load impedance by transmission formulas, the impedance of FSS can be calculated by using equation (2.12). The transmission and reflection properties of FSS are calculated for TE and TM polarization by using the impedance and reflection coefficient equations.

2.2.4 Zero-index based Metasurfaces

The MTSs have a refractive index near zero or less than unity, gives the potential application in the field of Electromagnetics. The intersection in the plane of ϵ - μ space diagram is the zero-index point, as shown in Fig.2.17. Several investigations are presented theoretically and experimentally that MTSs exhibits zero-index property within the specific frequency range. Phase constant β as a function of frequency pass through the zero-index point from the DNG region to the DPS region. For instance, the investigations provided in (Enoch et al. (2002), Enoch et al. (2003), Tayeb et al. (2003)) gives a zero-index EBG, which is realized and placed on a source that lies within the EBG passband to obtain a highly directive beam. The work by Alu et al. (2003) shown experimentally that the power can be increased by a flat conducting screen that has tiny apertures and a slab of materials with $\mu < \mu_0$. This is due to the screen supports the conversion of an incident wave into a directed leaky wave. The transmitted power is increased in such a structure and a sharp beam can be generated by covering the tiny structure on both sides. The study by Ziolkowski (Ziolkowski (2004)) gives the details about dispersive and passive materials having propagation and scattering properties that are matched approximately to free space and having a refractive index equal to zero with zero phase variations at the interface. The EM behavior of zero-index medium ($\epsilon(\omega_0) \cong 0, \mu(\omega_0) \cong 0$) implies that $Z(\omega_0) = Z_0, n(\omega_0) \cong 0$ gives the static characteristics in spacial and dynamic variation in time. To demonstrate this behavior, consider Maxwell's equations given by,

$$\nabla \times E_\omega = -j\omega\mu H \quad \nabla \cdot (\epsilon E_\omega) = \rho_\omega \quad (2.14)$$

$$\nabla \times H_\omega = j\omega\epsilon E + J_\omega \quad \nabla \cdot (\mu H_\omega) = 0 \quad (2.15)$$



(a)

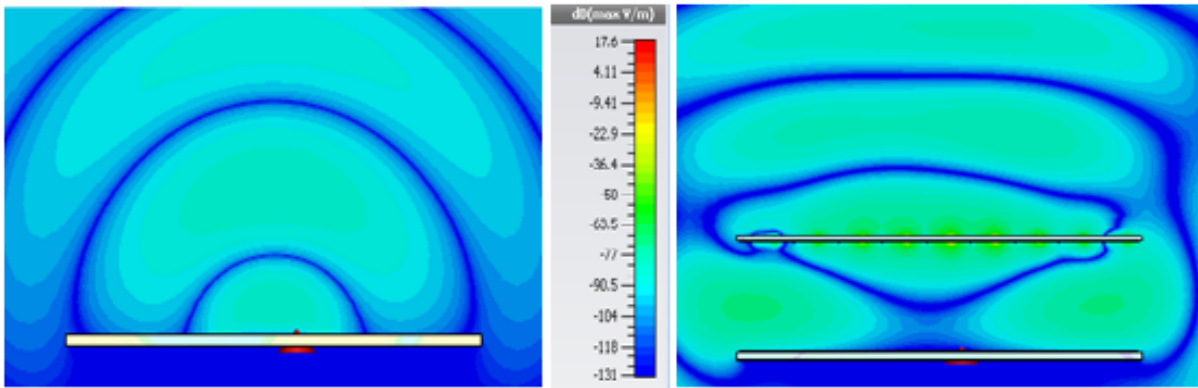
Figure 2.17: The zero index lie in the intersection of material classification based on ϵ and μ [Engheta and Ziolkowski \(2006\)](#)

when $(\epsilon(\omega_0) \approx 0), \mu(\omega_0) \approx 0)$, the time harmonic divergence equations then yield $\rho_\omega = 0$ and the time-harmonic curl equations reduce to

$$\nabla \times E_\omega = 0 \quad (2.16)$$

$$\nabla \times H_\omega = J_\omega \quad (2.17)$$

Since this means $\nabla \cdot J_\omega = 0$, then the charge conservation equation $j\omega\rho_\omega + \nabla \cdot J_\omega = 0$ is also satisfied. Thus the spatial components of the total electromagnetic field behave like a combination of a constant electric field and a magnetostatic magnetic field. Their specific values depend on the source and zero-index medium configuration. Thus the right side of the equations 2.16 and 2.17 is satisfied automatically in the medium, which has zero refractive index, if the fields are finite. Fig.2.18 shows the comparison between simple source antenna and zero-index based MTS antenna. In the figure, observation shows that the patch source distributes the fields spatially, but the zero-index based MTS directs the fields and focus the energy into a direction normal to its interface.



(a)

Figure 2.18: The spatial field distribution of (a) simple patch source and (b) zero-index based MTS

2.3 Theory of Characteristic Modes

The rapid growth of the wireless communication industry, EM simulation and modeling play an essential role in designing the antenna. This is due to the difficulty faced in understanding the physical insight of the antenna design and its excitation techniques. Many commercial softwares are available to solve the problem that exists in the antenna design, but these EM numerical modeling still give little information about the physical aspects of the antenna. From the practical aspect of the antenna design problem, the optimization becomes a tedious process due to the lack of physical concepts in antenna design to achieve enhanced radiation characteristics. The accuracy can be obtained by EM numerical modeling, which has an optimization algorithm. These algorithms give the optimized values to achieve the best performance of an antenna, but it's not true in all cases. As the structure of the antenna increases, the algorithms take more space and more computational time. After optimization, it is difficult to understand the radiation mechanism pertaining to that antenna. To follow clearly, the synthesis procedure of the antenna and to get optimized radiation performance, characteristic mode (CM) theory is a promising solution(Chen and Wang (2015b)). This CM theory is based on the modal analysis of a particular antenna problem.

Garbacz first formulated the theory of characteristic modes(CM) in 1965(Garbacz (1965)) and later, Garbacz and Turpin gave complete CM theory(Garbacz and Turpin

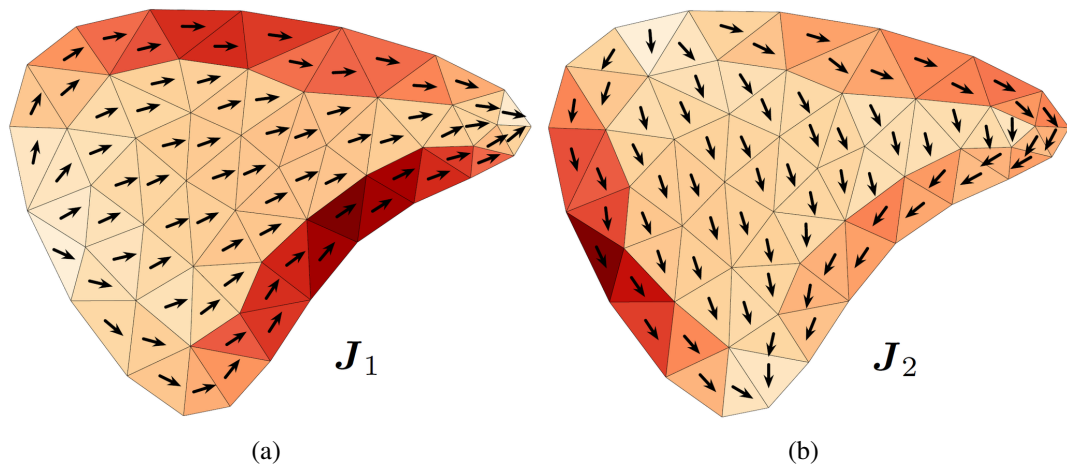


Figure 2.19: Characteristic modal currents of an arbitrary shaped conducting body (a) mode1 (b)mode 2

(1971)). Garbacz formulated the generalization of classical eigenfunctions termed as characteristic modes. He proposes the CMs have orthogonal property over both source region and sphere at infinity. Harrington and Mautz formulate CM theory based on the electric field integral equation (EFIE) in 1971 for PEC bodies in antenna engineering and scattering problems(Harrington and Mautz (1971)Harrington and Mautz (1971)). It relates to the tangential component of electric fields on the surface of the PEC body to the surface currents. By solving the eigenvalue equation and diagonalizing the operator used in EFIE, they obtained the similar modes formulated by Garbacz. Harrington's approach produced a convenient formula for CMs computation. CMs are the real currents of any arbitrary shape conducting bodies and they are solutions to the generalized impedance matrix obtained using Method of Moments(MOM). Fig.2.19 shows the first two modes of an arbitrary shaped conducting body.

The modal currents are the fields radiated or scattered by a PEC obstacle under harmonic excitation are called CMs, which form a convenient basis set to expand these currents. CMs are determined with source free excitation having eigenvalues and eigenvectors. CMs are the orthogonal basis functions that can be used to expand the total surface current on the PEC body. The characteristic currents are obtained using the eigenfunctions of the weighted eigenvalue equation. The eigenvalue equation is given

by,

$$XJ_n = \lambda_n R J_n \quad (2.18)$$

where λ_n is eigenvalues, J_n is the eigencurrents, X is the imaginary part and R is the real part of impedance operator Z and n represents indexing order of each mode. If the impedance operator Z is linear symmetric, then its hermitian parts X and R are real and symmetric, then eigenvalues λ_n are real and eigencurrents J_n are also real and equiphase over the surface. The total surface current on the conducting body gives information about the characteristic modes, i.e., $J = \sum \alpha_n J_n$, where α_n is the weighting coefficients to be determined which are the complete orthogonal set of modal currents. The α_n is given by,

$$\alpha_n = \frac{\oint_s (E^i J_n dS)}{1 + j\lambda_n} \quad (2.19)$$

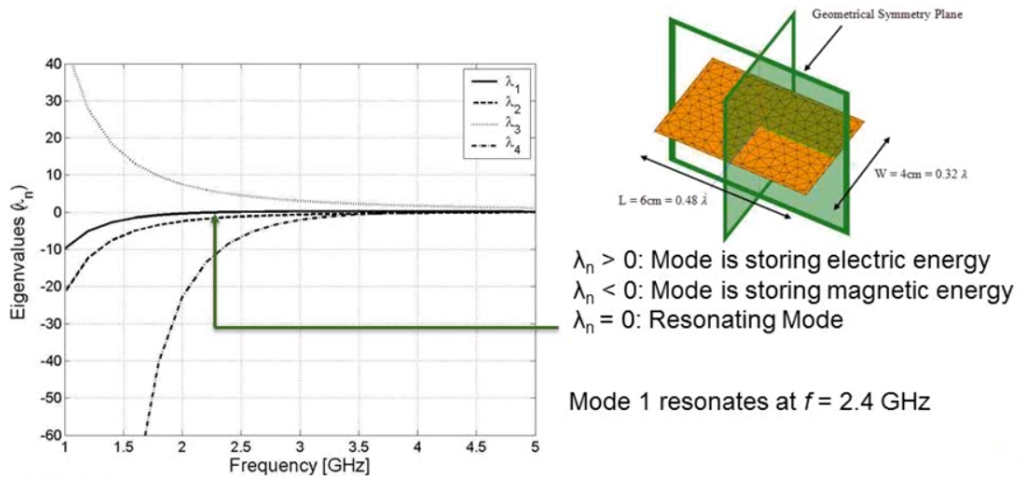
Modal significance(MS) is an important parameter to track the modes, which is defined as

$$|MS = 1/(1 + j\lambda_n)| \quad (2.20)$$

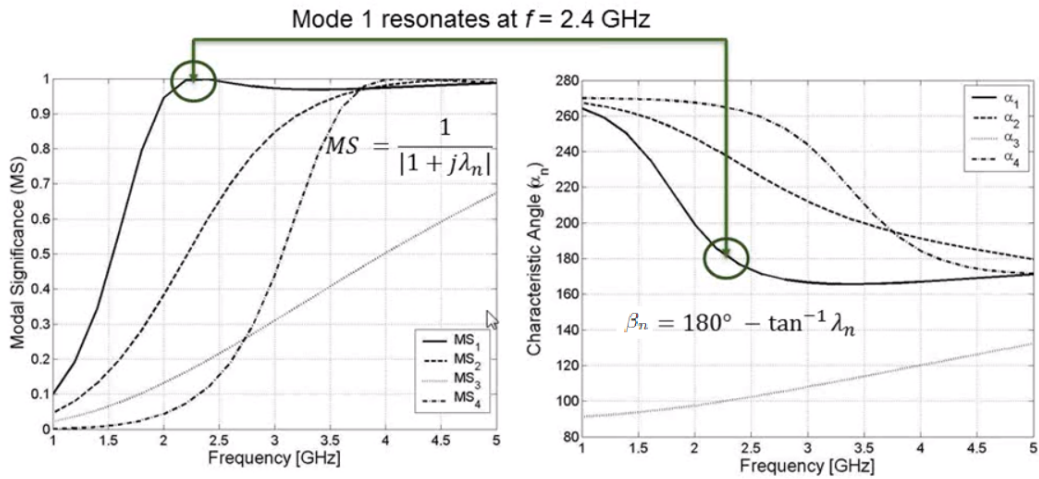
which ranges from 0 to 1. When the mode is resonant and most efficiently radiating, then its Modal significance value is 1. Also, the characteristic angle (β_n) is an important parameter that needs to be considered here to see the phase variation of each characteristic mode. It is defined based on the eigenvalue obtained from the equation(2.15), and it is given by,

$$\beta_n = 180^\circ - \lambda_n \quad (2.21)$$

To understand these CMs, consider a rectangular PEC plate analyzed using CMs. The eigenvalues, modal significance, and characteristic angle of the PEC plate are shown in Fig.2.20. From the figure, the eigenvalues of the first two modes are nearly zero, meaning that they are resonant modes and can be excited. The other modes are higher-order modes, which are of not useful to achieve the best radiation performance. Fig.2.21 shows the first four modes of modal currents and its radiation patterns. In the figure, it is observed that the first two modes are contributing to the radiation in the broadside direction. These modes can be excited to achieve the radiation performance



(a)



(b)

Figure 2.20: (a) Eigen values (b) modal significance and characteristic angle of rectangular PEC plate.

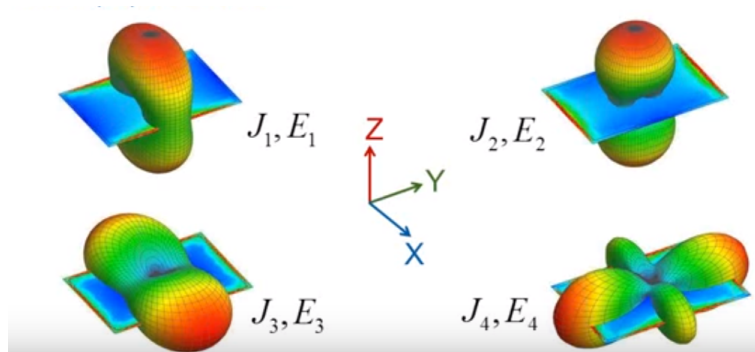


Figure 2.21: First four modal currents and modal radiation patterns of rectangular PEC plate

of rectangular PEC. The other two modes are higher-order modes, and they can't be useful for radiation.

CMs are promising solutions to an antenna engineer to understand the real insight of modes and their radiation characteristics. As we discussed in the earlier chapter about circular polarization, it is challenging to analyze CP antennas with a single feeding technique due to mode patterns. The modes contributing to CP radiation can't understand easily. By utilizing the potentials of CMs, it is easy to design circularly polarized antennas, CP based MTSs, and also scattering problems.

2.4 Literature Survey

In this section, an overview of the literature work related to the design of MTS based CP antennas, wideband/multi-band CP antennas and high gain CP antennas are discussed. Each section describes the literature available on the particular designs stated in the objectives. The first section explains about the CP antennas and characteristic mode based antennas to achieve CP. Also, the RCS reduction technique in MTS antennas and their design techniques are described. In the upcoming subsections, the recent works about the potentials of MTSs to achieve wideband CP antennas, the zero-index property of MTSs, and their applications to achieve high directive beams and different techniques to achieve multi-band CP operations are discussed.

2.4.1 Characteristic mode based antennas and RCS reduction in metasurface antennas

Metasurfaces are required by the numerous applications due to their properties to control the Electromagnetic (EM) Wavefronts. Microstrip antennas can use the metasurfaces to achieve requirements like wideband CP, beam steering, wavefront shaping, beam-tilting, Linear to circular polarization conversion, biomedical devices, absorbers, angular independent surfaces[[Chen et al. \(2016b\)](#) and [Holloway et al. \(2012\)](#)]. [Zhu et al.](#)

(2013) proposed a rectangular loop with diagonal strip and truncated corner patches that are used to convert LP to CP waves with wide operational bandwidth. Nasimuddin et al. (2016) used rectangular sub-wavelength patches to enhance the impedance and axial ratio bandwidth. In (Zhang and Dong (2017)), a shared aperture MTS is placed on top of the CP patch to get RCS reduction in wide bandwidth and gain enhancement. In the above designs, Equivalent circuit modeling is used to analyze the MTS.

Characteristic mode analysis (CMA) is a promising solution to understand the systematic design of antennas. In [Daviu (2008), Fabres (2007), Chen and Wang (2015a)], modal analysis is used to analyze the structures like wire, planar monopole, mobile chassis, etc., by decomposing the surface currents of the conducting structures. The asymmetric ‘U’ and ‘E’ shaped CP antennas (Chen and Wang (2012)) are analyzed based on the characteristic modes to achieve CP. Metamaterial based metal-dielectric structure is analyzed based on the reactive impedance substrate, which exhibits artificial magnetism excited by the parallel magnetic field using modal analysis. A new expression is introduced to calculate the Q factor of an arbitrarily shaped antenna that has metamaterial inclusions. The method of moment based analysis solves for the external and internal resonances, but external resonances are only the characteristic modes. These methods are given by [Rabah et al. (2016b), Rabah et al. (2016a)]. Miers and Lau (2016) proposed the design, which has minimum radiated power defined in the structure, which removes all internal resonances using the new post-processing technique, which gives unique and real CMs.

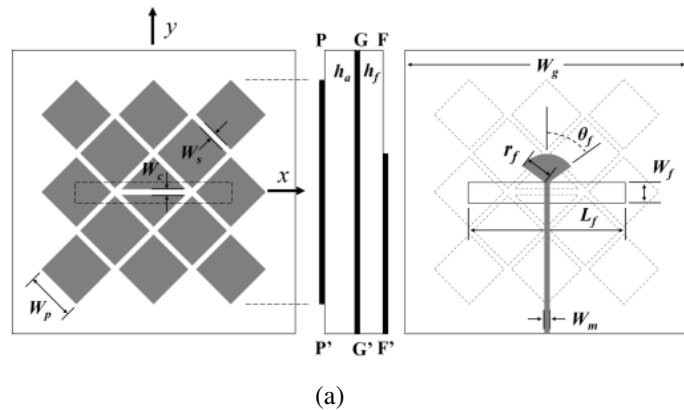


Figure 2.22: Wideband MTS antenna using CMA

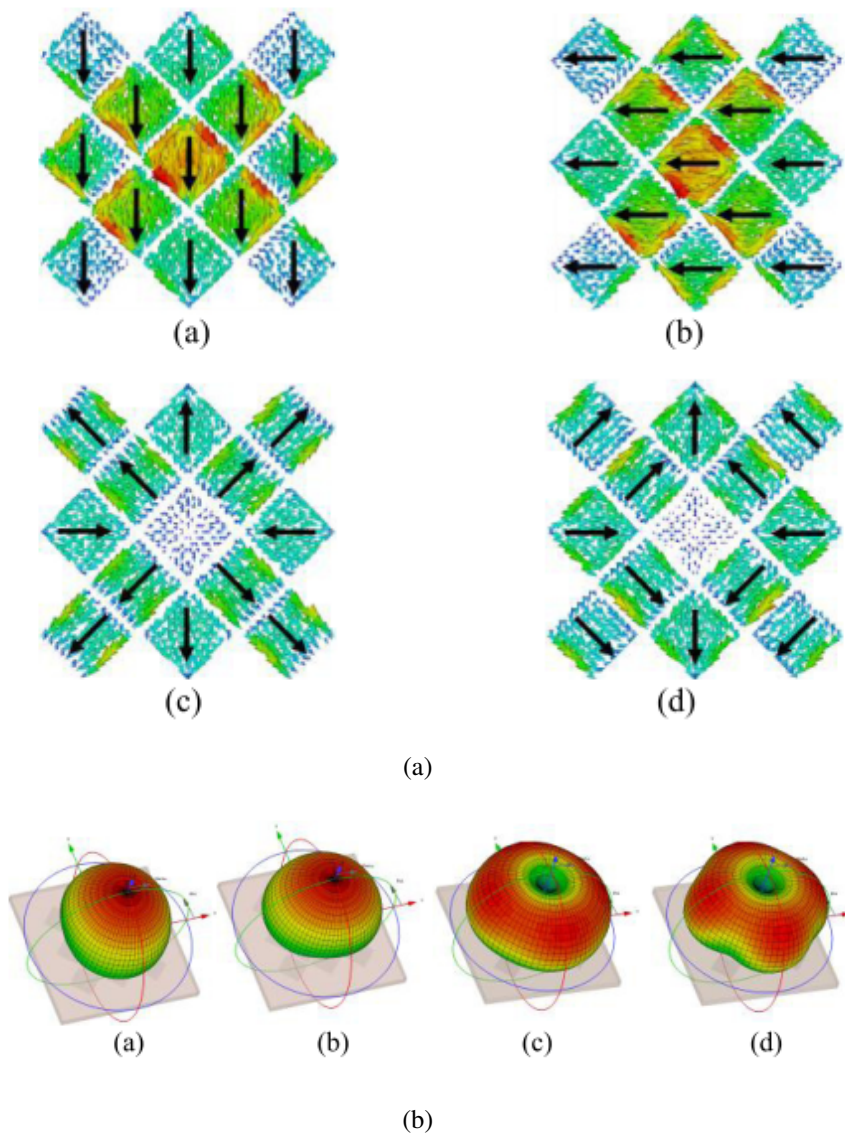


Figure 2.23: Modal currents and modal patterns of MTS antenna(Lin and Chen (2017))

The bandwidth enhancement for MIMO mobile handset[Li and Shi (2018),Deng et al. (2016)], stub loaded dipole(Luo et al. (2019) and ring-type CP slot antennas(Saraswat and Harish (2018)) are analysed using characteristic modes. wideband and dual-band CMA based MTS antennas are proposed in[Lin and Chen (2017),Li and Chen (2018)]. The MTS antenna analyzed using CMA to achieve wideband property is shown in Fig.2.22 and the modes are shown in Fig.2.23. The wideband characteristic is obtained using MTS mode and slot mode.

Radar cross-section reduction is essential nowadays for many radars and stealth

technologies, which can be easily integrated into the communication systems. Antennas are contributing more in the area of radar and stealth platforms to reduce overall RCS of the system. The previous literature shows that good improvement in out-band and in-band RCS reduction over a wide bandwidth with features like CP, high gain, and good front to back ratio. (Zheng et al. (2015)) proposed a checkerboard surface having two different Artificial Magnetic Conductors(AMCs), which gives a 180° reflection phase difference between them to reduce RCS over a wideband. (Zhao et al. (2017)) uses the checkerboard array concept to obtain broadband RCS reduction with CP. In (Zhao et al. (2017)), a broadband MTM Polarization Dependent Artificial Magnetic Conductor(PDAMC) surface is designed using complementary SRR to reduce the RCS.

(Zhao et al. (2016)) proposed a new polarization-insensitive MTS that varies spatially in dimension to reduce reflection in the desired direction to get the bistatic reduction of RCS in the wide frequency range of 7-12 GHz. [Chen et al. (2016d), Chen et al. (2015)] uses different EBG structures as checkerboard surfaces on the same ground plane to reduce dual-band monostatic and bistatic RCS in wide bandwidth which scatters the field in four quadrants. The bistatic RCS pattern is shown in Fig.2.24. Huang et al. (2016) proposed a frequency reconfigurable two-layer metasurface to reduce the RCS. An absorbing top layer is embedded with the slot coupled microstrip patch antenna along with reflecting phase cells in the bottom layer. Varactor diodes tune the frequency in the reflecting phase cells at the bottom surface. Han et al. (2017) presented a novel double-slotted polarization-dependent EBG structure that reduces the RCS and enhances gain in the boresight direction. The layout pattern is adopted to improve gain and the chessboard type surface is used to reduce the RCS of the MPA. Low RCS is achieved by the energy cancellation method in the boresight direction and gain is enhanced by increasing aperture efficiency.

Mu et al. (2017) proposed a Partially reflecting and absorbing Surface(PRAS) to simultaneously reduce in-band, out-band RCS, and enhance the gain at boresight direction. A PRS cell is placed on top and the absorbing surface is placed below the patch antenna. Kandasamy et al. (2015) presented a novel cross slot based MS which reduce

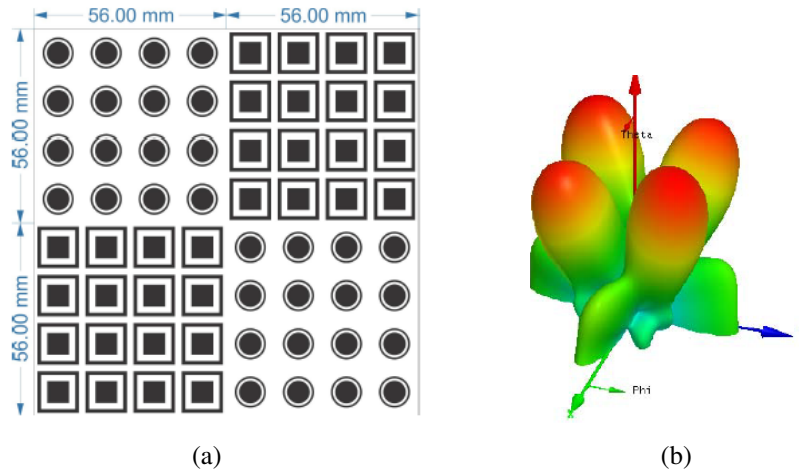


Figure 2.24: RCS reduction using checkerboard type metasurface (Chen et al. (2016d))

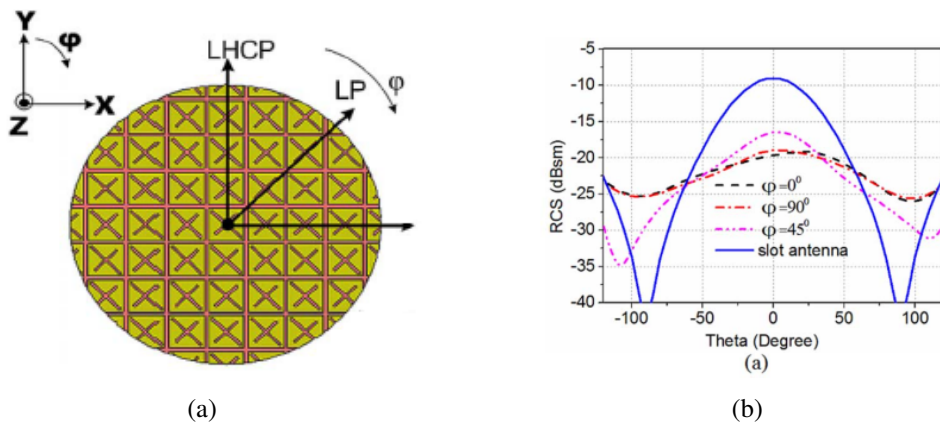


Figure 2.25: RCS reduction using absorbing type of cross slot based MTS (Kandasamy et al. (2015))

the RCS and achieves polarization reconfigurability. The MTS is rotated concerning to the slot antenna to switch the polarization from LP to CP and vice-versa. MTS acts as an absorbing surface to reduce the RCS in a broadside direction. The structure with its RCS pattern is shown in Fig.2.25. [Jia et al. (2015),Jia et al. (2017)] proposed a polarization conversion MS and three different AMC surfaces to reduce RCS and achieve wideband CP. PCM achieves CP and high gain over the wide operating band and there is a passive phase cancellation between PCM and AMCs to reduce RCS. A wideband Polarization Rotation Reflective Surface(PRRS) is used to convert incident LP to reflective orthogonal polarization. By arranging the PRRS unit cells, RCS reduction is achieved in a wide frequency range. [Zheng et al. (2015),Zheng et al. (2017)] proposed

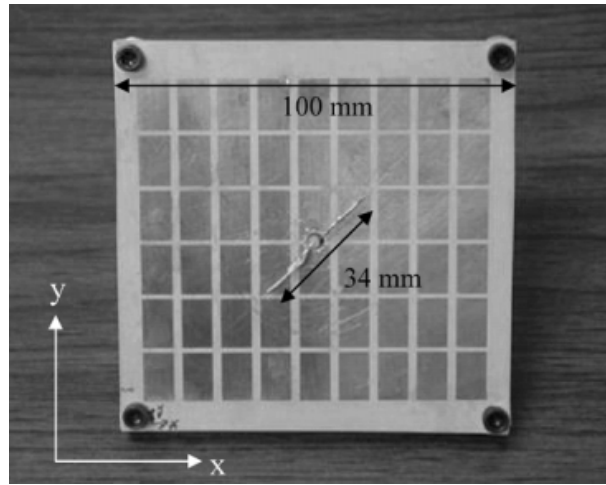
composite AMCs(3 types), which are arranged to get destructive phase difference to reduce the RCS over Ultrawideband frequency range.

The third chapter of the thesis contributes to a design of MTS based CP antenna using CMA. The modal analysis is applied to rectangular patch-based MTS to analyze two orthogonal modes required to achieve CP. The RCS reduction capability of MTS is also analyzed using the absorptive property of MTS. The proposed antenna is compact and can be utilized in stealth and space applications.

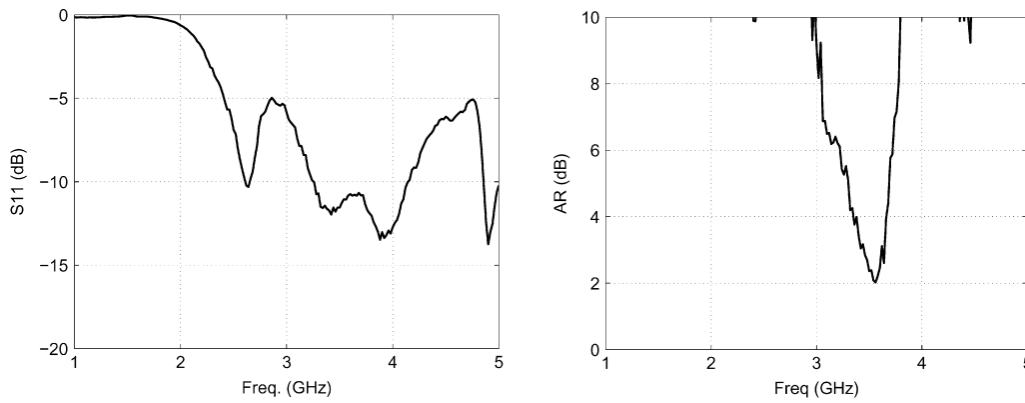
2.4.2 Wideband metasurface based circularly polarized antennas

Wideband CP antennas are required in wireless applications to achieve high data rates as well as to accommodate the increased number of users. Many techniques have been used to convert linearly polarized antennas to exhibit circular polarization behavior in wide operating bandwidth. By introducing strip lines into coplanar waveguide (CPW)-fed slot antennas, a broadband CP is achieved in [Cao and Yu (2015),Karamzadeh et al. (2016),Pourahmadazar and Mohammadi (2011)]. In [Sze et al. (2008)], an inverted L-shaped asymmetric CPW-fed slot antenna with small strips is proposed to achieve a wideband CP. A strip-loaded monopole antenna is designed to obtain a wideband CP in [Saini et al. (2017)]. As strip loading is sensitive to the design process, achieving optimum wideband CP characteristics using a stub or the strip-loading method is difficult. The gain of a slot antenna is low because its radiation characteristic is bidirectional. A perfect reflector or a backed cavity can be used to improve the gain, but both have a limited axial ratio bandwidth [Fu et al. (2014),Pan et al. (2012), Li et al. (2008)]. Therefore, metasurfaces (MTSs) are the potential structures that can be used to obtain CP and good gain in a wide range of frequencies.

MTSs are used as reflectors to achieve axial ratio <3 dB over a wide bandwidth. Frequency selective surfaces (FSS), high impedance surfaces (HIS), artificial magnetic conductors (AMCs) and electromagnetic bandgap (EBG) structures are some of the MTSs used as reflectors to improve the gain, CP bandwidth and pattern purity. A simple linearly polarized dipole antenna is utilized to generate a circularly polar-



(a)



(b)

Figure 2.26: (a)The fabricated prototype of simple dipole backed by polarization dependent MTS. (b) experimentally verified reflection coefficient and axial ratio plots (Fan Yang and Rahmat-Samii (2005))

ized wave using an EBG structure in [Fan Yang and Rahmat-Samii (2005) Yi and Qu (2013)]. Fig.2.26(a) shows a polarization-dependent MTS based dipole antenna. It converts the LP wave radiated by a dipole into CP wave by reflective property of MTS placed below it. Fig.2.25(b) shows its reflection coefficient and axial ratio plots. Different slot antennas with a single- and dual-layer AMCs as reflectors are investigated in [Agarwal et al. (2013a) Agarwal et al. (2013b)]. A loop antenna is designed with an AMC as a reflector to improve axial ratio bandwidth in [Li et al. (2013)]. The above MTS-based antennas have less axial ratio bandwidth. The careful design of a primary source antenna with MTS as a reflector can achieve wideband CP characteristics. Corner truncated microstrip patch antennas have been discussed in the literature, but they

have a narrow CP bandwidth [Sharma and Gupta (1982)]. In [Kandasamy et al. (2016)], a pair of SRRs are loaded on the truncated slot antenna for dual-band CP applications. The disadvantage is that the corner truncated slot antenna alone cannot achieve a CP. The loading of an SRR on the truncated slot antenna gives a CP in both bands. In our proposed design, the perturbed slot antenna alone can produce a wideband CP by increasing the depth of perturbation.

The fourth chapter of the thesis presents a novel perturbed slot antenna to achieve wide axial ratio bandwidth. Further, to improve the axial ratio over a wide range of frequency, an FSS based reflective MTS is used. The combined effect of the slot antenna and FSS gives wide axial ratio bandwidth. The proposed design is useful in wireless applications to assign a maximum number of users in a mobile environment. In the other design, an SRR is placed on the slot antenna to improve the CP bandwidth. The slot mode and SRR modes are controlled to achieve optimum wide axial ratio bandwidth. Since this design is a single layer, it is utilized for soil sensing applications.

2.4.3 High Gain Metasurface Antennas

In space applications like satellite and radar, high gain antennas are essential. Many high gain LP antennas are designed using metamaterials. Using Fabry Perot (FP) cavity concept in [Li et al. (2017), Long et al. (2017)] to achieve high gain. Here in FP cavity-based antennas, the FP resonant condition is to be satisfied to improve the gain. So another good class of MTMs to enhance the gain is materials with zero or near-zero permittivity or permeability, which are called zero-index materials (ZIM). ZIM enhances the directivity when excited with a primary source. Many high gain antennas are designed based on ZIM/low index metamaterial (LIM) in the microwave and visible region using subwavelength metallic thin wires (Enoch et al. (2002)), resonant non-magnetic inclusions (Silveirinha and Engheta (2007)) epsilon near zero (ENZ) media (Liu et al. (2008)) and metal-dielectric nanostructures (Vespeur et al. (2013)). Also, multilayered ZIM based high gain antennas are proposed in [Zhou et al. (2009), Li et al. (2012)]. The thin metallic wires and modified split-ring resonators are used to design a

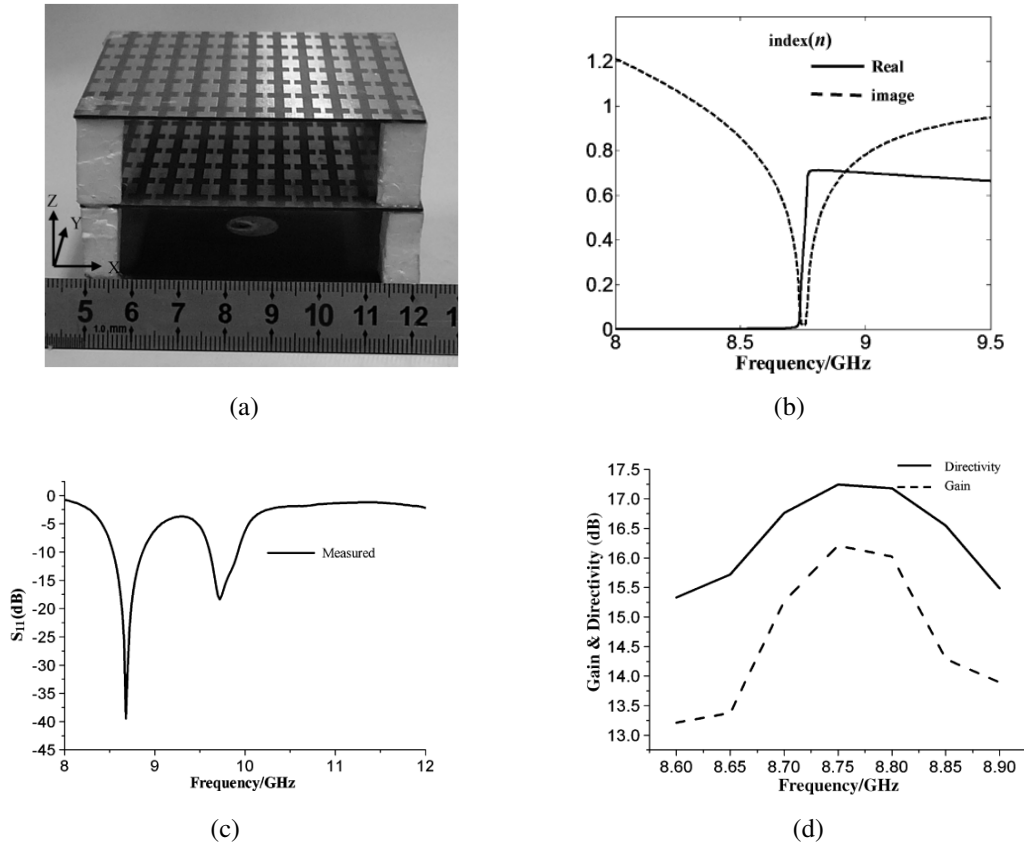


Figure 2.27: (a)The multilayer ZIM based high gain antenna prototype (b) Frequency response of refractive index (c) S_{11} plot (d) comparison between gain and directivity plot (Zhou et al. (2009))

zero-index metamaterial lens to enhance the gain (Meng et al. (2012)). To enhance the directivity of an antipodal tapered slot antenna and a SIW slot antenna, zero-index based unit-cells are investigated in [Sun et al. (2013), Jiang et al. (2014)]. ZIM lens antenna based on AMC surface(Turpin et al. (2014)) and reactive impedance surface (RIS) (Majumder et al. (2018)) are designed for compact high gain antennas. Fig.2.27(a) shows the fabricated prototype of a multilayer ZIM based MTS antenna. Fig.2.27(b) & (c) shows the refractive index and reflection coefficient plot. Fig.2.27(d) shows the comparison of directivity and gain plot. In this design, the gain of the patch antenna is enhanced, but it is linearly polarized. High gain CP antennas are an essential requirement in space and radar applications [William A. Imbriale et al. (2006)]. Also, The ZIM based high gain antennas available in the literature are LP antennas. Hence, there is a scope to design a ZIM based antenna with simultaneous LP to CP conversion with

gain enhancement.

The fifth chapter of the thesis proposes the ZIM based high gain antennas. In the first design, the gain of a CP patch antenna is enhanced using a swastika and ring-shaped ZIM MTS. In the second design, a two-sided dual split ring based ZIM is proposed to convert LP to CP wave and gain enhancement of rectangular patch antenna simultaneously. The proposed designs are useful in space communication in comparison with other ZIM based antennas.

2.4.4 Multiband Circularly Polarized Antennas

The multi-band CP antennas are essential in mobile communication to operate multiple bands at a time. There have been many antennas in the literature that shows good CP characteristics. [Bao and Ammann \(2007\)](#) proposed the design of a dual annular ring with a compact circular patch and an unequal arm slotted ground plane with a small CP frequency ratio. By adjusting the length of the cross slots, dual-band CP is achieved. [Chen and Yung \(2009\)](#) presents a CPW fed dual sense dual-band CP slot antenna loaded with asymmetric spiral slots at the edges. Two spiral slots with opposite rotation give two sense of polarization and two T shaped strips give CP with dual-band. [Nasimuddin et al. \(2010\)](#) proposed an S-shaped slotted MSA for dual-band CP application. The asymmetric slot arms of S shape are adjusted to get CP without an increase in the thickness and size of the patch. In [Chen and Yung \(2011\)](#), a corner truncated patch is proposed by loading two outside L shaped stubs. The outside L shaped stub excites the inner mode of truncated corner patch. Inner mode and originally excited with outer mode gives the dual-band dual circular polarization with front to back ratio of around 20 dB. [Shao and Chen \(2012\)](#) presents cross slot and annular slot based dual-band dual sense antenna. Two resonant frequencies are produced by annular slot and cross slots of asymmetric length. Electromagnetic coupling is used to excite asymmetric slots and annular slot, which gives a circularly polarized antenna. [Weng et al. \(2014\)](#) presents a single layer compact low profile dual-broadband CP antenna with a single feeding. An L-shaped and asymmetric U-shaped strips are introduced in the slots to get dual-band

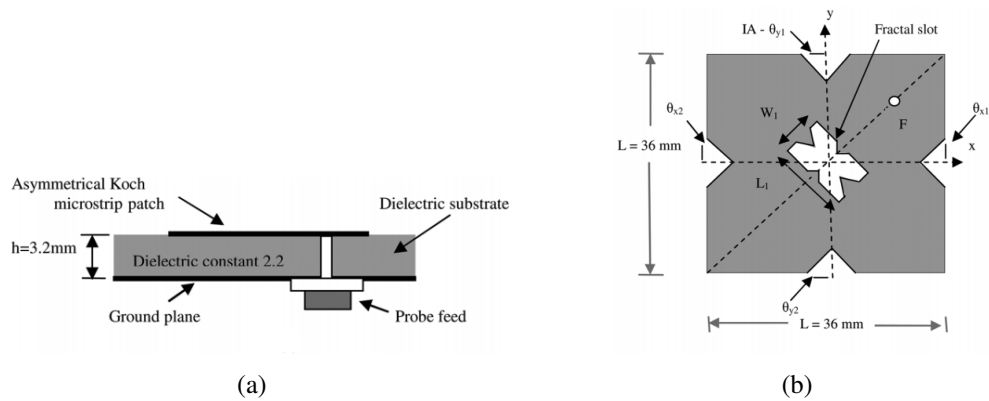


Figure 2.28: Proposed asymmetrical multiband CP Antenna (a) cross-sectional view and (b) top view (Reddy and Sarma (2014))

CP characteristics. L shape gives the lower band and the U shape gives higher band CP.

A single feed single layer Koch fractal boundary microstrip antenna is designed (Reddy and Sarma (2014)) to get triband CP is shown in Fig.2.28. By introducing the slot in the Koch fractal patch and by iterative Koch functions, CP is achieved. Wang et al. (2015) proposed a single layer bent microstrip feeding structure to get wideband with dual-band CP. L shape and T-shaped slots are introduced to excite two modes, which are orthogonal to get dual-band CP. A rectangular patch is added to improve the CP bandwidth and impedance bandwidth. (Liang et al. (2015)) proposed a complementary semicircular monopole loaded with adjusting stubs to get dual-band CP. The monopole and its complementary gives LP and the adjusting stubs are added to achieve CP. Saurav et al. (2015) introduced a dipole loaded with multi-band resonators to achieve multi-band CP. By controlling the geometrical parameters of the LC resonator, multi-band CP is achieved. A cavity is attached to get the unidirectional radiation pattern.

A shared aperture array of different microstrip antennas (Zhang et al. (2016), Zhang et al. (2017)) is presented to obtain dual-band with dual CP. A rotating feeding network is used to match the array. A pair of arc-shaped (Chen et al. (2016c)) slits are embedded in a circular patch to achieve LP and two gap coupled capacitive grids are added to get orthogonal modes to achieve CP. In Kandasamy et al. (2016), dual-band CP is obtained by an SRR loaded cavity-backed corner truncated slot antenna. The outer ring of SRR is connected and changing the orientation to get a dual sense of polarization. The two

bands are controlled independent each other with unidirectional radiation pattern without affecting the CP performance. FSS can be used to achieve more bands with CP. Quadband CP(Hoang et al. (2016)) is achieved by loading FSS to U-shaped patch with I and L shaped structure tilted 45° with respect to the horizontal axis. Dual-band CP with improved impedance and axial ratio bandwidth is achieved by loading FSS to an S-shaped slot antenna(Ding et al. (2017)). Saini et al. (2017) presented a monopole antenna loaded with parasitic strips and I shaped grounded stub to obtain dual sense CP with dual-band characteristics. Dual-band antennas are designed with circular polarization with dual-polarization sense(Nayeri et al. (2011),Rui et al. (2016)). In the above designs, structures are sensitive to design parameters like slit or stub loading methods and optimization is a tedious process. Also, the tuning of frequency bands and polarization sense is difficult. Some of the designs present dual-band CP antenna with independent tuning, but axial ratio bandwidths are less. This requires the design of more frequency bands with independent tuning and CP characteristics.

The sixth chapter in the thesis presents the dual and triband CP antennas. In the first design, a dual-band CP antenna with a <3 dB axial ratio over a wide bandwidth is obtained in each band. The second design presents a triband CP with an independent tuning capability of each resonance frequency band. Also, polarization sense can be altered at each resonance frequency. The presented designs are compact and useful in wireless applications compared to other MTM inspired dual and triband CP antennas.

CHAPTER 3

CHARACTERISTIC MODE ANALYSIS OF A COMPACT METASURFACE ANTENNA WITH CIRCULAR POLARIZATION AND LOW RCS

3.1 Introduction

In this chapter, the characteristic mode analysis of a low profile, compact MTS antenna with circular polarization characteristics for in-band RCS reduction is discussed. The characteristic modes provide an intuitive analysis of the conducting structures in the multilayered medium. The metasurface is analyzed using source free characteristic modes. These modes give a better understanding of the mode contribution to the radiation properties of the metasurface. These modes are excited to obtain the desired radiation performance. The circularly polarized antenna is designed using rectangular patch-based polarization-dependent MTS (PDMTS). The PDMTS produces two orthogonal degenerate modes and it is excited with linearly polarized slot antenna to show its polarization conversion capability. Also, the RCS reduction capability of MTS is analyzed using plane wave incident normal to the MTS. The absorptivity property of PDMTS is utilized to reduce the RCS within the entire impedance bandwidth. The proposed antenna is compact and it has the overall size of $0.52\lambda_0 \times 0.52 \lambda_0 \times 0.078\lambda_0$ (where λ_0 is the free space wavelength). The antenna performance is validated experimentally by considering the axial ratio bandwidth, impedance bandwidth, monostatic RCS and gain.

3.2 Characteristic Mode Analysis of PDMTS

The rectangular patch-based PDMTS is shown in Fig.3.1(a). The PDMTS is etched on top of the roger RO4003C substrate ($\epsilon_r=3.38$, $\tan\delta=0.0027$ and height $h_s=3.454\text{mm}$) and it is oriented 45° with respect to XY plane. The PDMTS is analyzed using a method of moment (MOM) based CMA tool in CST MWS. The CMA results of PDMTS are obtained with PEC boundary applied in the negative z-direction with all other sides as open boundaries, as shown in Fig.3.1(b). In characteristic mode (CM) theory, the generalized eigenvalue equation is given by, $X\vec{J}_n = \lambda_n R\vec{J}_n$ where λ_n is eigenvalue. The eigenvalue reveals the resonant behavior of each mode. The modal significance ($MS=1/(1 + \lambda_n)$) and characteristic angle($CA=180^\circ - \lambda_n$) are the other two parameters, which effectively determine the radiation performance of each mode. The MS helps to distinguish between higher-order CMs from fundamental CM by transforming eigenvalues to a smaller range [0,1].

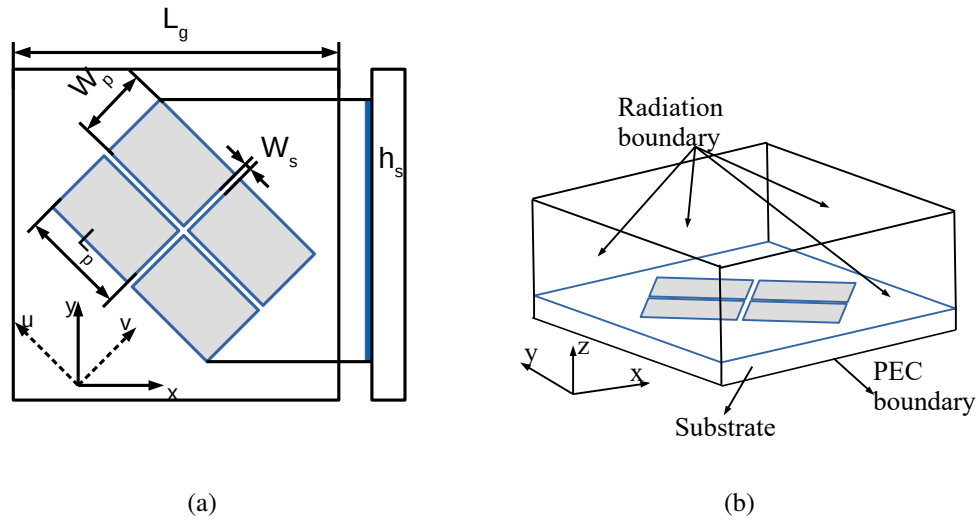


Figure 3.1: (a) Geometry of the proposed PDMTS (b) Open radiation boundary set up with PEC in the -Z direction. $L_g=27\text{mm}$, $L_p=8.5\text{mm}$, $W_p=6\text{mm}$, $W_s=0.3\text{mm}$, $h_s=3.454\text{mm}$.

The PDMTS patches have meshed and electrical currents are solved to get the modal behavior of PDMTS. The MS and CA of the first four modes are shown in Fig.3.2. In CMA results, J1 to J4 represents the first four characteristic modes. The first two modes

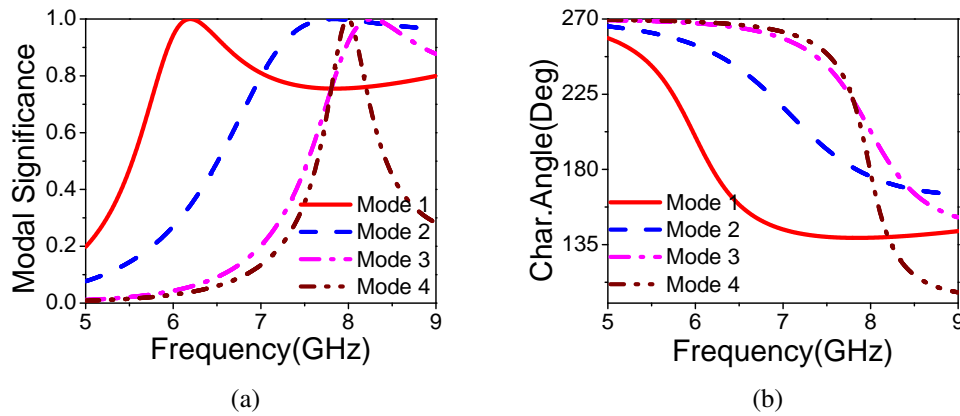


Figure 3.2: Simulated (a) modal significance(MS) and (b) characteristic angle(CA) of the first four modes(J1-J4) of PDMTS.

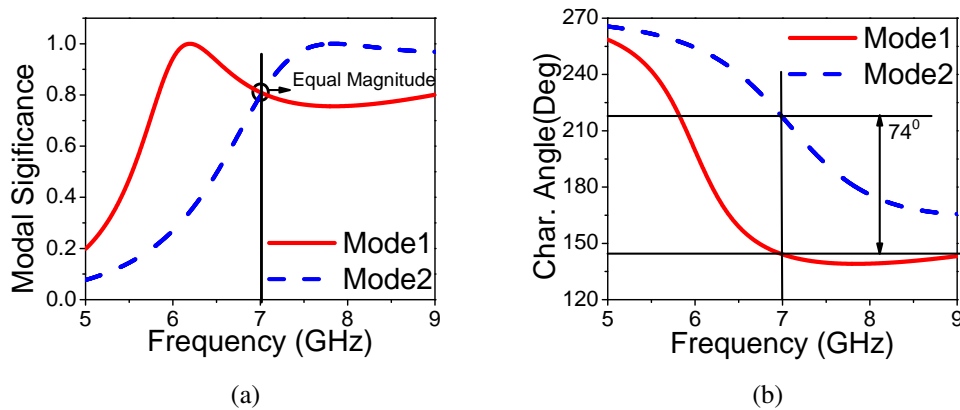


Figure 3.3: Simulated (a)modal significance and (b)characteristic angle of first two modes(J1, J2) of PDMTS.

possess equal magnitude and the phase difference of 74° at 7.02GHz and it is shown in Fig.3.3. Even though the phase shift between two modes is less than 90° before feed excitation, circular polarization can be achieved satisfactorily after feed excitation (Chen and Wang (2012)). The first four modal currents of the MTS at 7.02GHz are shown in Fig.3.4. It is observed that all the modal currents of J1 are in-phase over the MTS in u direction and all J2 modal currents are in-phase over the MTS in the v direction. J1 and J2 are the pair of orthogonal modes that are responsible for circular polarization. J3 and J4 are the higher-order modes which are opposite current distribution about u and v axes. The first four modal radiation patterns of the MTS at 7.02GHz are shown in Fig.3.5. The first two modes are well radiated in bore-sight direction and orthogonal to

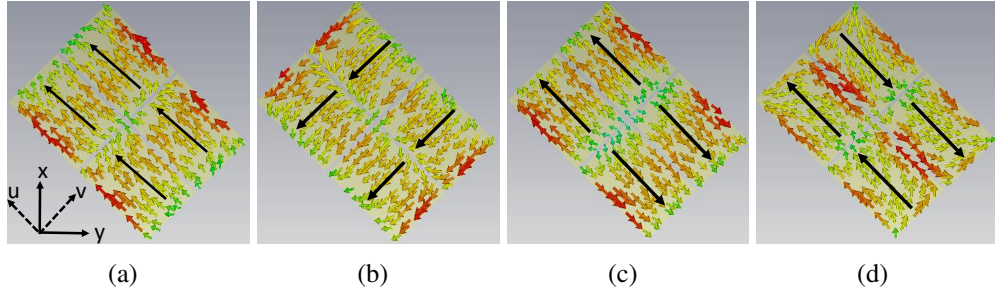


Figure 3.4: Simulated modal current distribution of PDMTS (a)J1 (b)J2 (c)J3 (d)J4

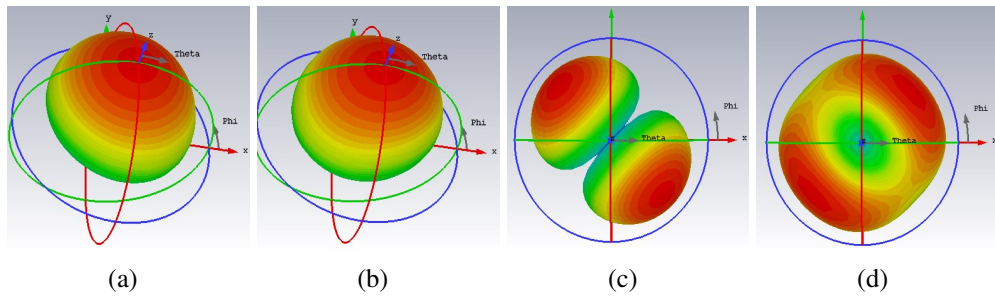


Figure 3.5: Simulated modal radiation pattern of PDMTS. (a)J1 (b)J2 (c)J3 (d)J4

each other, but higher-order modes have radiation null in the bore-sight direction. This analysis suggests that the first two modes are orthogonal and have an excellent in-phase current distribution with good broadside radiation performance. Excitation of mode J1 and mode J2 gives circular polarization with a good broadside radiation pattern.

Fig.3.6 and Fig.3.7 show the parametric study of characteristic modes to know the sensitivity of the designed parameters. It is observed that the effect of W_p on the modes is significant. If the parameter W_p increases, the resonance shifts to lower frequency due to the increase of MTS electrical size. The phase shift between the first two modes can be optimized using parameter W_p . W_s decides the coupling between patches, increasing the value of W_s shift the resonance to a higher frequency. The parametric study of CMA helps us to optimize the modal behavior.

3.2.1 CMA of PDMTS with slot

To see the effect of slot used to excite the PDMTS, the PDMTS with slot is analyzed using CMA. The slot portion of the surface is assigned as radiation boundary with all

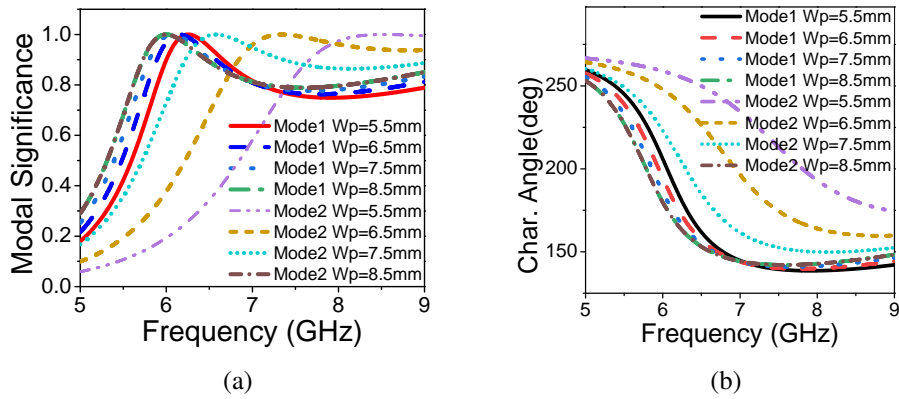


Figure 3.6: Effect of W_p on simulated (a) modal significance (b) characteristic angle.

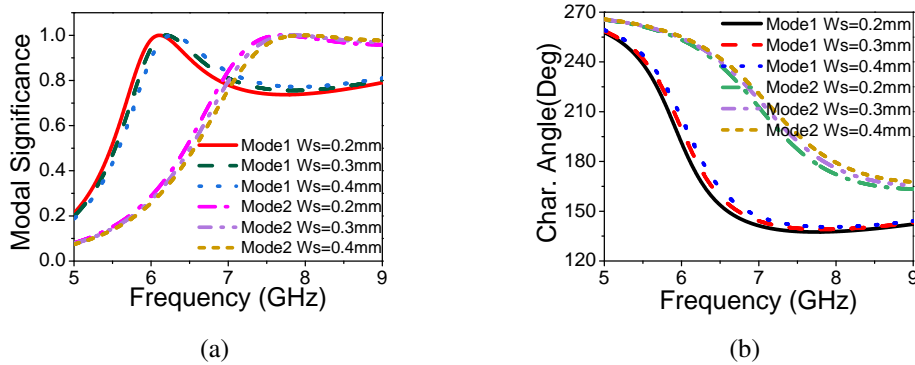


Figure 3.7: Effect of W_s on simulated (a) modal significance (b) characteristic angle

other sides keeping same as the Fig.3.1(b). The slot mode will affect the CP resonance of MTS and shifts to lower frequency. The MS and CA plots are shown in Fig.3.8. Mode 1 is the slot mode which resonates at 4.8 GHz and mode 2 & mode 3 are the MTS modes with slot, which are earlier mode 1 and mode 2 of MTS without slot. The MTS modes with slot (mode 2 and mode 3) have a phase difference of 82° at 6.3 GHz. The modal significance of these modes is the same at 6.3 GHz and phase difference is shown in the characteristic angle plot. After exciting the slot with the microstrip feed line, these MTS modes(mode 2 and mode 3) are intern excited by the slot to successfully achieve CP radiation.

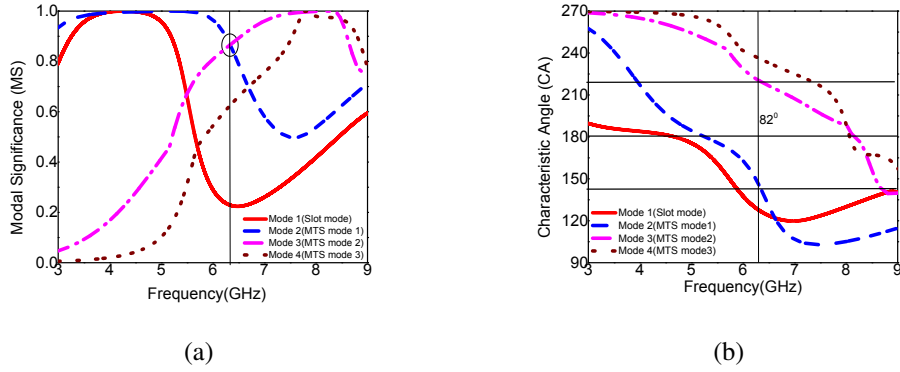


Figure 3.8: CM analysis of MTS with slot (a) modal significance (b) characteristic angle

3.3 Circularly polarized antenna design using PDMTS

The PDMTS analyzed using CMA method is loaded on a slot antenna to design CP antenna. It consists of PDMTS (SS'), slot antenna (GG'), and microstrip feed line (FF'), as shown in Fig.3.9. The slot antenna is designed using RO4003 rogers substrate ($\epsilon_r = 3.38$, $\tan\delta = 0.0027$) with thickness of $h_a = 0.508$ mm. The 50Ω microstrip feed line is printed on the top surface and the slot is engraved on the bottom surface. The slot antenna has the optimized dimensions of $L_f=11.65$ mm, $W_f=1.5$ mm and $W_{fl}=1.1$ mm. Fig.3.9(a) shows the PDMTS is loaded on the slot antenna and Fig.3.9(b) shows the bottom side, which is in direct contact with the microstrip feed line without any air gap. The PDMTS, feed line and slot are aligned at the center of the XY plane. Since the PDMTS is oriented 45° with respect to the XY plane, the mode directions of J1 and J2 of PDMTS are in-phase with the electric field component in u (Eu) and v direction (Ev) of the slot antenna. This enables the slot antenna to efficiently couple the PDMTS and produces right hand circularly polarized (RHCP) waves. To get left hand circularly polarized (LHCP) wave, the PDMTS should be placed on the other diagonal (v direction) of the substrate with respect to the XY plane. The surface current on PDMTS at the different instant of time rotates in anticlockwise direction with respect to +z -direction produces RHCP waves, as shown in Fig.3.10. The parametric study of PDMTS loaded slot antenna using full-wave analysis is shown in Fig.3.11 and Fig.3.12. The most significant parameters are L_f and W_f , which gives the impedance bandwidth

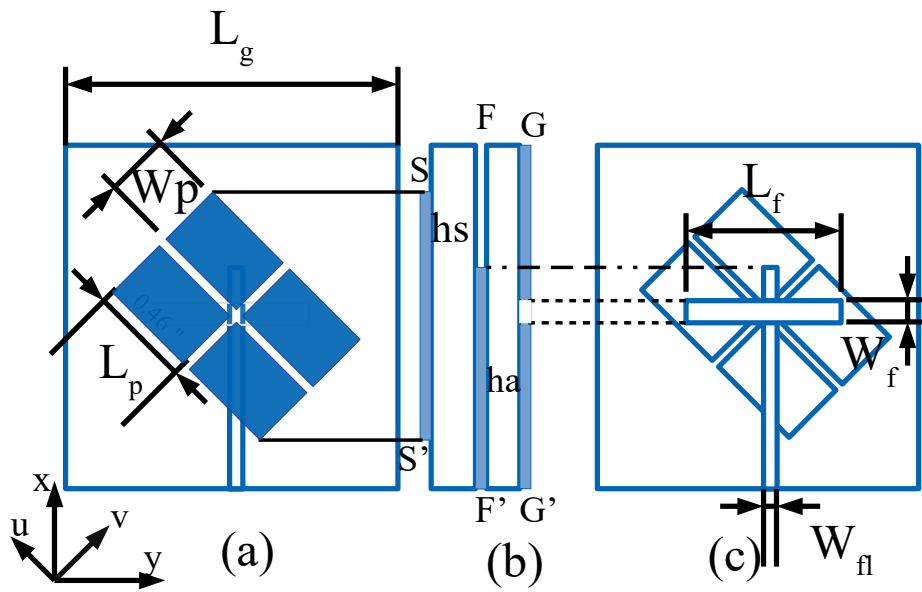


Figure 3.9: Structure of the proposed design (a) front view (b) side view (c) back view

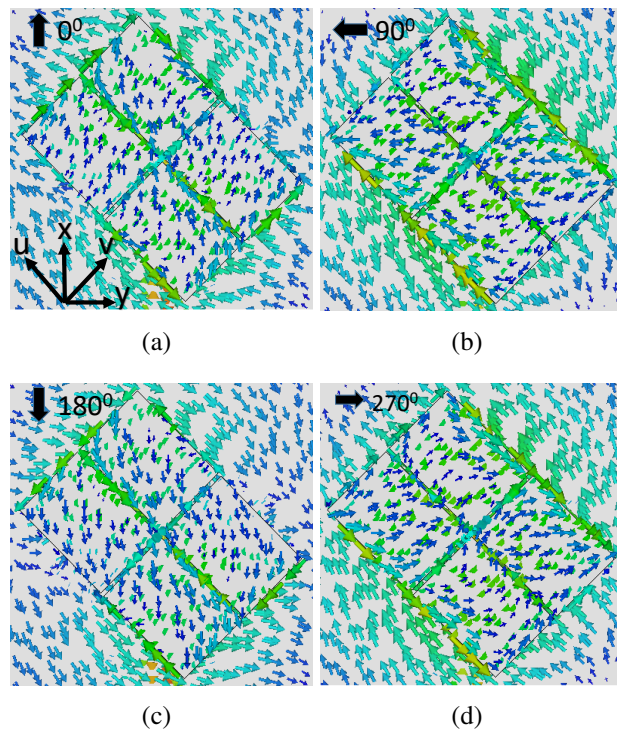


Figure 3.10: Simulation results of Surface current distribution at different time instant (a) $t=0$ (b) $t=T/4$ (c) $t=T/2$ (d) $t=3T/4$

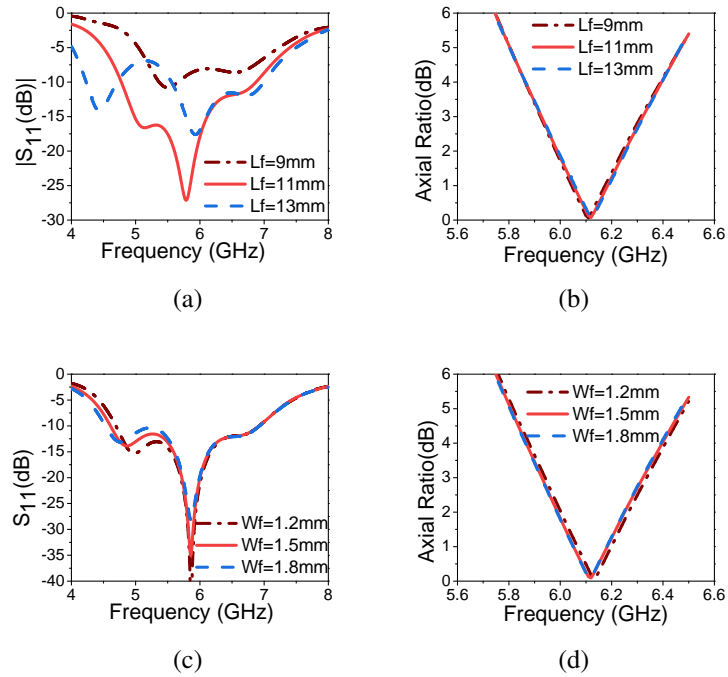


Figure 3.11: Effect of L_f and W_f on simulated S_{11} and axial ratio (a & b) L_f (c & d) W_f

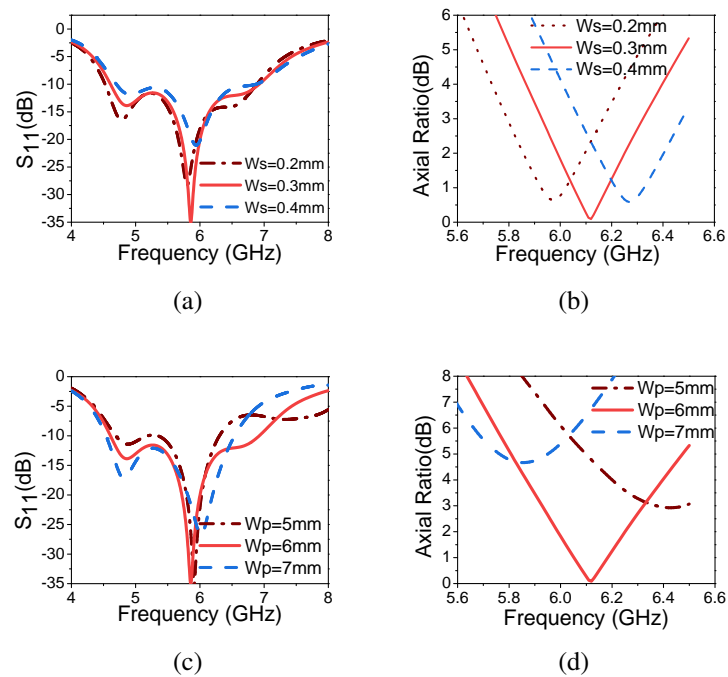


Figure 3.12: Effect of W_s and W_p on simulated S_{11} and axial ratio (a & b) W_s (c & d) W_p

variation but not the axial ratio. In the figure, increasing L_f shift the resonance to lower frequency and split the mode into degenerating modes. By decreasing L_f , the mode shifts to the higher frequency and also impedance matching degrades. Even though the modes of PDMTS with slot analyzed using CMA are resonating at 6.3 GHz before excitation, the resonance of CP antenna shifts to lower frequency after excitation of slot with microstrip line due to overall substrate thickness. The MTS mode and slot mode are combined to give wider impedance bandwidth. W_f does not affect much on the resonance frequency, but it improves the impedance matching. By optimizing the parameters L_f and W_f , good impedance bandwidth can be achieved. W_p is the parameter that affects the axial ratio significantly because of the change in the electrical dimension of MTS. W_s is also helpful to optimize the axial ratio as well as impedance variation. The CMA results are well in agreement with full-wave analysis (FWA), as shown in the parametric study. Finally, the L_f and W_f are mainly contributing to impedance matching, while W_p and W_s are helps to optimize the axial ratio.

3.4 RCS Reduction of the MTS CP Antenna

In stealth applications like radar, the antenna also considered as a potential reflector of the overall system. In the proposed antenna without PDMTS loading, the slot acts as a primary source antenna with poor RCS performance. The metasurface is absorbing the maximal incident energy and reduces the RCS. The two-dimensional periodic arrangement of sub-wavelength patches acts as an absorbing medium. The simulation is performed to find the absorptivity of the metal-backed MTS at the resonance frequency. A plane wave is incident normal to the MTS to calculate the absorptivity from the reflection coefficient curve. Fig. 3.13 (a) shows the absorptivity curve. The simulation set-up is shown in the subset of the same figure. The absorptivity is calculated using $A=1-|S_{11}|^2$, the proposed PDMTS covered slot antenna gives the absorptivity of 95%. When absorptivity value is nearly 100%, the material act as a perfect absorber. Absorbers act as RCS reduction materials [[Kandasamy et al. \(2015\)](#),[Wu et al. \(2016a\)](#),[Ghosh et al. \(2015\)](#),[Liu et al. \(2013\)](#)].

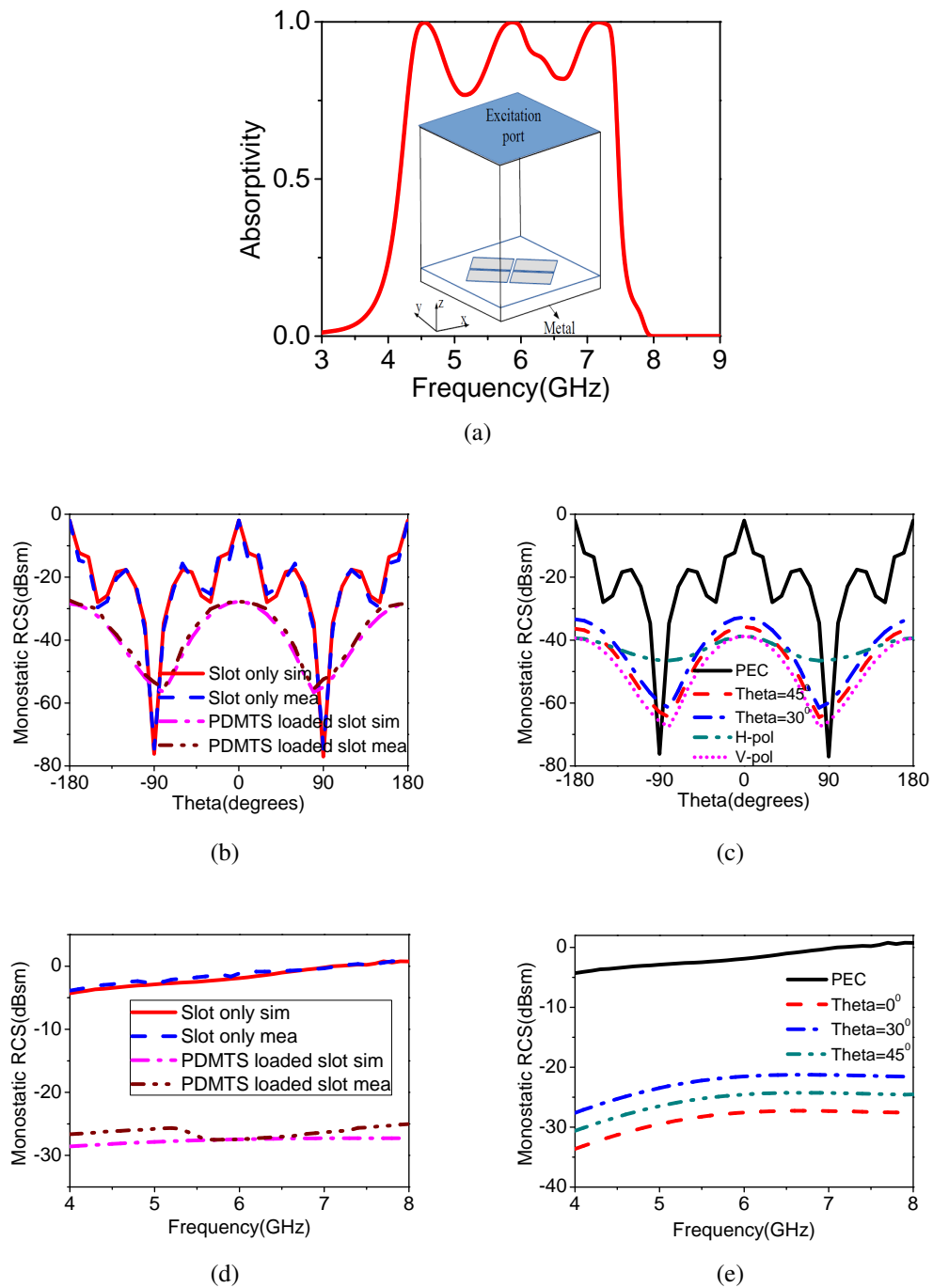


Figure 3.13: Simulated absorptivity magnitude of metal backed PDMTS (b) Simulated monostatic RCS variation of PDMTS loaded slot antenna over oblique incidence (c) simulated frequency response of the monostatic RCS vs oblique incidence (d) simulated and measured monostatic RCS vs Angle at 5.86 GHz for y polarized wave (e) simulated and measured frequency response for y polarized wave at broadside direction.

To observe the in-band RCS reduction capability of PDMTS loaded slot antenna, simulations and measurements are carried out for plane wave incident with different incident angles. The proposed antenna achieves a monostatic RCS reduction of -32.2 dBsm for y polarized wave at the resonance frequency of 5.86 GHz. Fig. 3.13(b) shows the variation of monostatic RCS with respect to the different incident angles. The observed monostatic RCS of the slot without PDMTS is -2 dBsm at its resonant frequency. It infers that there is a remarkable RCS reduction of -30.2 dBsm is achieved with the loading of PDMTS on the slot antenna. The PEC is the standard electromagnetic wave reflector. To evaluate the RCS reduction performance of the proposed PDMTS, the RCS of PEC is compared with the PDMTS. The RCS performance of the slot antenna with and without PDMTS is compared to show the RCS reduction capability of the PDMTS [30-32]. Fig. 3.13(c) shows the simulated RCS frequency response of PDMTS loaded slot with different incident angles. The observation in the figure shows that the frequency response has nearly -28 dBsm RCS reduction over the entire impedance bandwidth. The monostatic RCS is weakened with respect to oblique incidence over the in-band frequency. This is due to the increase in the reflectivity property of MTS with oblique incidence. Fig. 3.13(d) and 3.13(e) shows the simulated and experimentally verified results of monostatic RCS for y polarized wave. The measured results are comparable with the simulated results of the proposed MTS based CP antenna.

3.5 Fabrication and experimental results

Fig.3.14 shows the proposed prototype of the fabricated design. Fig.3.15 shows the comparison between simulated and measured results of gain, axial ratio bandwidth and impedance bandwidth. Fig.3.15(a) shows the measured and simulated impedance bandwidth ($|S_{11}| < -10$ dB). The simulated impedance bandwidth of 2.31 GHz (39.42%) from 4.61 GHz to 6.92 GHz and 3 dB axial ratio bandwidth of 0.39 GHz (6.72%) from 5.92 GHz to 6.31 GHz is achieved. The measured impedance bandwidth of 1.575 GHz (29.11%) from 4.96 GHz to 6.535 GHz and 3-dB axial ratio bandwidth of 0.49 GHz (9.05%) from 5.83 GHz to 6.32 GHz is achieved. The measured monostatic RCS value

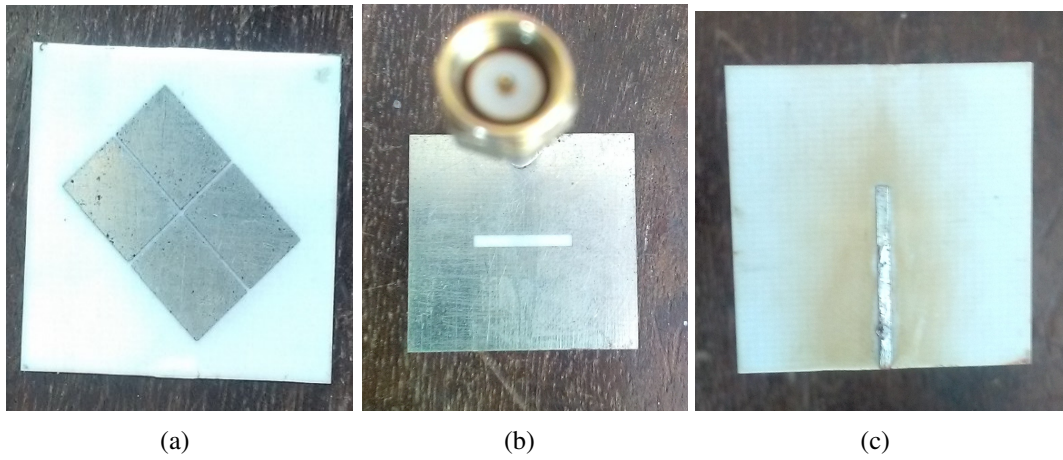


Figure 3.14: Prototype of the fabricated structure (a) front view(MTS) (b) back view(slot) (c) micro-strip line feed

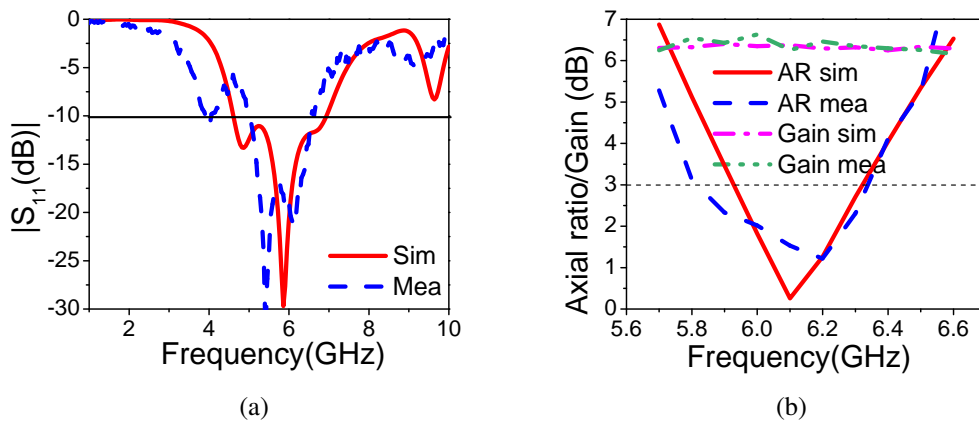


Figure 3.15: Simulated and measured S_{11} , axial ratio and gain (a) S_{11} (b) axial ratio and gain

of -23.2 dBsm is achieved for the proposed PDMTS loaded slot antenna. Fig.3.15(b) shows the simulated and experimentally verified gain of the antenna. The measured bore-sight gain of 6.34 dBiC is achieved at the center frequency. There is 0.5 dB gain variation in the entire axial ratio bandwidth because of small fabrication errors and SMA connector losses.

The measured and simulated radiation patterns of the MTS based CP antenna at two frequency points in azimuth and elevation planes are shown in Fig.3.16. In the figure, measured radiation patterns are in accordance with the simulated results both in RHCP and LHCP. The cross-polarization (LHCP) level of -10 dB is achieved in azimuth

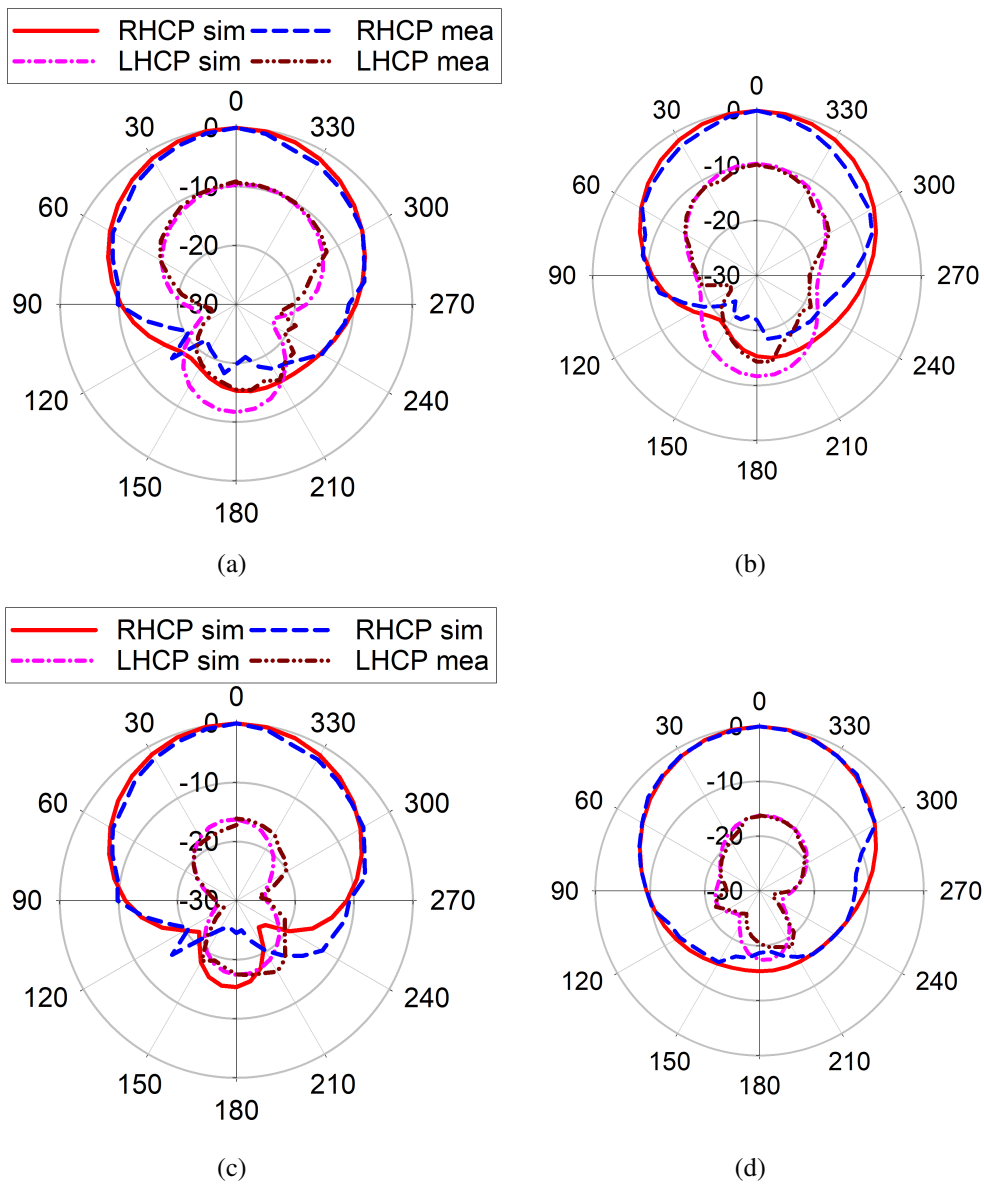


Figure 3.16: Simulated and measured RHCP and LHCP radiation pattern at 5.86 GHz (a) xz palne (b) yz palne and 6.3 GHz (c) xz plane (d) yz Plane

and elevation planes compared with the co-polarization (RHCP) level. The front to back (FB) ratio of -15 dB is achieved in both azimuth and elevation planes. Table 3.1 presents the comparison between the MTS based CP antenna and other literature.

Table 3.1: Comparison of performance metrics of the proposed CMA based MTS CP antenna

Ref.	Size (λ_0 is at 5.86 GHz)	Impedance bandwidth (%)	Axial ratio bandwidth(%)	RCS reduction band	CMA
[Zhu et al. (2013)]	$\lambda_0 \times \lambda_0$	25.1	8.37	No	No
[Zhu et al. (2014)]	$0.9\lambda_0$ (diameter)	26.31	11.4	No	No
[Kandasamy et al. (2015)]	$0.97\lambda_0$ (diameter)	26.35	2.36	4-5GHz	No
[Nasimuddin et al. (2016)]	$0.8\lambda_0 \times 1.17\lambda_0 \times 0.064\lambda_0$	35.6	28.6	No	No
[Wu et al. (2016b)]	$0.595\lambda_0 \times 0.49\lambda_0 \times 0.07\lambda_0$	33.7	16.5	No	No
[Lin and Chen (2017)]	$1.06\lambda_0 \times 1.06\lambda_0 \times 0.078\lambda_0$	31	No	No	Yes
[Zhao et al. (2016)]	$4.52\lambda_0 \times 4.52\lambda_0 \times 0.056\lambda_0$	7.54	No	5.14-7.15 GHz	No
[Zhao et al. (2017)]	$6.56\lambda_0 \times 4.28\lambda_0 \times 0.3\lambda_0$	10.93	No	3.15-3.25 GHz	No
[Wu et al. (2016a)]	$3\lambda_0 \times 3\lambda_0 \times 0.1\lambda_0$	8.47	No	9-19 GHz	No
proposed	$0.52\lambda_0 \times 0.52\lambda_0 \times 0.078\lambda_0$	29.11	9.02	4-8 GHz	Yes

3.6 Summary

In this chapter, A CP antenna based on PDMTS with in-band RCS reduction capability is presented. The PDMTS is analyzed using CMA to find two orthogonal degenerate modes to achieve CP. The polarization conversion capability of PDMTS from the LP into the CP wave is successfully validated. The proposed PDMTS CP antenna has a low profile and achieves an impedance bandwidth of 1.57 GHz and a 3 dB axial ratio bandwidth of 0.49 GHz. Also, the antenna gives good in-band RCS reduction capability. CMA is a powerful method in analyzing the modal behavior, excitation of modes, and feed optimization.

CHAPTER 4

WIDEBAND ANTENNAS WITH CIRCULAR POLARIZATION CHARACTERISTICS

4.1 Introduction

The first section of this chapter presents the design of a single-layer planar slot antenna with wideband circular polarization characteristics. It is fed by coplanar waveguide (CPW) feeding technique and it is backed by a frequency selective surface (FSS). A square slot antenna is designed at 2.5 GHz, which radiates linear polarization. The impedance bandwidth optimization of the planar slot antenna is performed by tuning a stub-loaded modified CPW feed line. The corners of the square slot antenna are perturbed to produce two orthogonal degenerate modes required for a wideband CP operation. The corner perturbed slot antenna gives an axial ratio bandwidth of 20.68% at 4.35 GHz resonance and the gain of the perturbed slot antenna is 1.88 dB. Furthermore, A 6×10 array of FSS is placed below the slot antenna to improve the gain and axial ratio bandwidth. The FSS improve the axial ratio bandwidth up to 31.14% at 4.33 GHz resonance and a peak gain of up to 4.87 dB. In the second section, a CPW fed slot antenna loaded with a rotated SRR to achieve wideband CP is presented. The corner truncation of the slot antenna provides CP in the lower band. To get CP in a higher band, the split gap of the inner ring is rotated 90° concerning to outer ring. The wideband CP response is achieved by merging two resonances of rotated SRR and perturbed slot antenna. Since the design is a single layer, it is utilized as a sensor to find the moisture content present in the soil. The antenna is placed on the surface of the testing soil and its reflection coefficient is measured. The resonance frequency varies as per the moisture content present in the soil.

4.2 A slot antenna with circular polarization and wide-band characteristics using Frequency Selective Surface

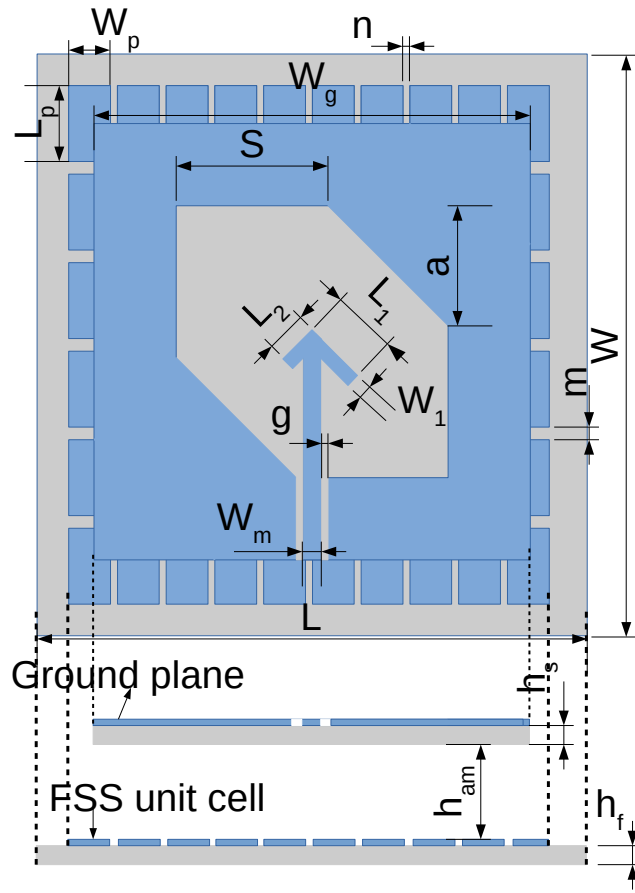
In this design, a slot antenna with a frequency selective surface for wideband CP characteristics is discussed. A slot antenna is designed to achieve CP, but the axial ratio bandwidth and gain are less. The potential property of FSS is used to enhance the CP bandwidth and gain of the slot antenna.

4.2.1 Antenna structure and Its operation

Fig.4.1 shows the proposed antenna and it consists of an FSS layer and CPW fed corner perturbed slot antenna. An inexpensive FR4 ($\epsilon_r=4.3$, $\tan\delta=0.025$) is utilized to design FSS and slot antenna. The FSS is placed underneath the slot antenna. An air gap of $h_{am}=22$ mm is maintained between the slot and FSS. The slot antenna resonance frequency is calculated using equation 1(Kandasamy et al. (2016))

$$f_r = \frac{c}{2S_l} \sqrt{\frac{2}{1 + \epsilon_r}} \quad (4.1)$$

where c =speed of light, $S_l=(S+a)$ = square slot length. Two tuning stubs are added to the CPW feed and by varying the parameters of these tuning stubs better impedance bandwidth is obtained. The proposed antenna parameters are $W_p=7$ mm, $L_p=13$ mm, $W_g=70$ mm, $W_m=3$ mm, $S=29$ mm, $n=0.1$ mm, $m=0.2$ mm, $W=89$ mm, $L=100$ mm, $h_s=1.6$ mm, $h_f=0.508$ mm, $a=8.4$ mm, $L_1=7$ mm, $L_2=5$ mm, and $W_1=1$ mm. The conventional slot is perturbed to obtain the axial ratio over the wideband. Fig. 4.2(a) shows the simulation results of the axial ratio and reflection coefficient of the slot antenna with various values of perturbation. The optimized value of perturbation is $a=8.4$ mm, as the axial ratio value deteriorates with a further increase in truncation. Fig.4.3 shows the electric field distribution of the corner perturbed slot antenna at different time instants. In the figure, the truncated slot antenna produces left-hand circularly polarized (LHCP)



(a)

Figure 4.1: The proposed FSS-based antenna structure.

waves. The opposite corners of another diagonal of the slot antenna should be truncated to obtain right-hand circularly polarized (RHCP) waves. Further, to enhance the gain and CP bandwidth of the corner perturbed slot antenna, an FSS consisting of rectangular unit cells are used. The proposed FSS acts as a polarization-dependent reflective surface. The gain is enhanced by selecting FSS so that it reflects the signal from the slot antenna back to the forward direction. The maximum gain is obtained for the 6×10 array. The rectangular unit-cell size of an FSS is W_p and L_p and the overall size of the FSS array is $W \times L$. n and m are the gaps between rectangular unit-cells in the vertical and horizontal directions. The perturbed slot gives a CP bandwidth of 3.9-4.8 GHz. The polarization-dependent reflective property of the FSS is used to enhance the CP bandwidth. Fig.4.4 shows the reflection phase characteristics for the x- and y-polarized

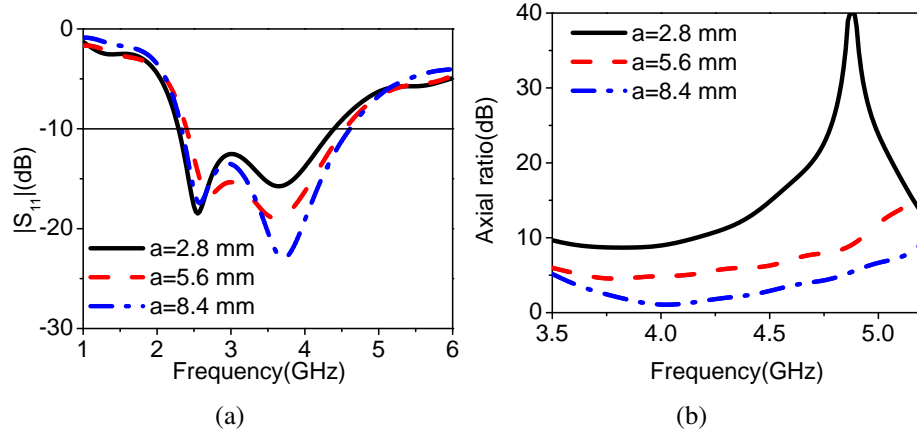


Figure 4.2: Simulation results of reflection coefficient plot and axial ratio plot of the perturbed slot antenna. (a) $|S_{11}|$ (b) axial ratio.

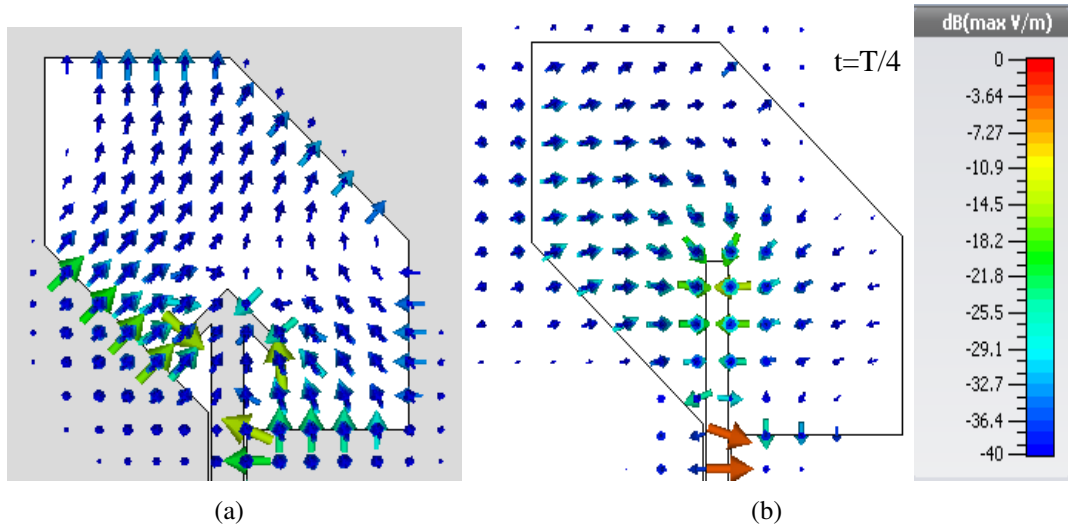


Figure 4.3: Simulated electric field distribution of the truncated slot antenna at 3.47 GHz. (a) $\omega t=0$ (b) $\omega t=90^\circ$.

wave incident orthogonal to the top surface of the FSS unit-cell. The proposed FSS gives a reflection phase of 90° for the x- and y-polarization from 3.6 GHz to 5 GHz. As explained in (Fan Yang and Rahmat-Samii (2005)), this 90° phase difference produces a CP radiation in the forward direction. This phase difference enhances the CP bandwidth of 3.6-5 GHz of the perturbed slot antenna. The total field E is calculated as the sum of the direct radiating field (E_f) of the slot antenna and the reflected field (E_r) from FSS. It is given by

$$E = \vec{E}_f + \vec{E}_r = \frac{E_0}{\sqrt{2}} e^{-jkz} [(x + y) + j(x - y)] \quad (4.2)$$

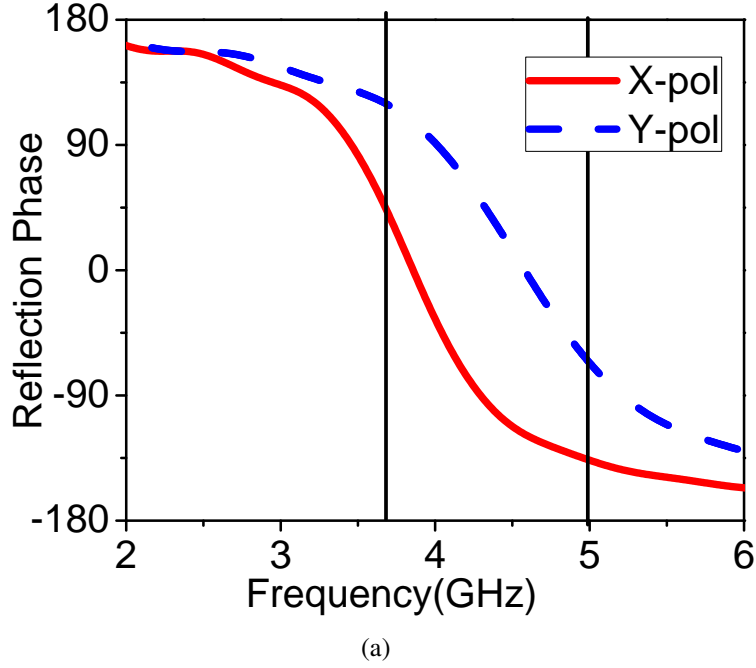


Figure 4.4: The FSS unit-cell characteristics in-terms of its reflection phase

$$\text{where } \vec{E}_f = \frac{E_0}{\sqrt{2}}[\vec{x} e^{-jkz} + \vec{y} e^{-jkz}]$$

$$\vec{E}_r = \frac{E_0}{\sqrt{2}}[\vec{x} e^{-jkz} e^{j\theta_x} + \vec{y} e^{-jkz} e^{j\theta_y}]$$

where E_0 is the amplitude of E, k is the wavenumber, and θ_x and θ_y are the polarization-dependent reflective phases for the x- and y-polarized incident waves, respectively. Fig.4.5 gives the presented antenna design process. The corner perturbed slot antenna is designed to operate (case a) at 2.5 GHz, which produces LP waves. Fig.4.5(b) shows the axial ratio plot of the square slot antenna and its value at its designed resonance frequency is high. The perturbed slot (case b) resonates at 3.66 GHz and produces a wide axial ratio bandwidth of 20.68%. Further, To attain the wide CP bandwidth, the FSS array is placed beneath the corner perturbed slot antenna (case c), which enhances the axial ratio bandwidth to 30.94%. The comparison among the conventional slot antenna, the corner perturbed slot antenna over a perfect electric conductor (PEC), and the FSS-backed slot antenna provides the performance evaluation of FSS is shown in Figs. 4.6(a) and 4.6(b). The S_{11} plot in Fig. 4.6(a) provides the resonance frequency variation of the slot backed by PEC or FSS. The resonance of PEC or slot antenna with FSS is shifted compared to the perturbed slot because of the loading

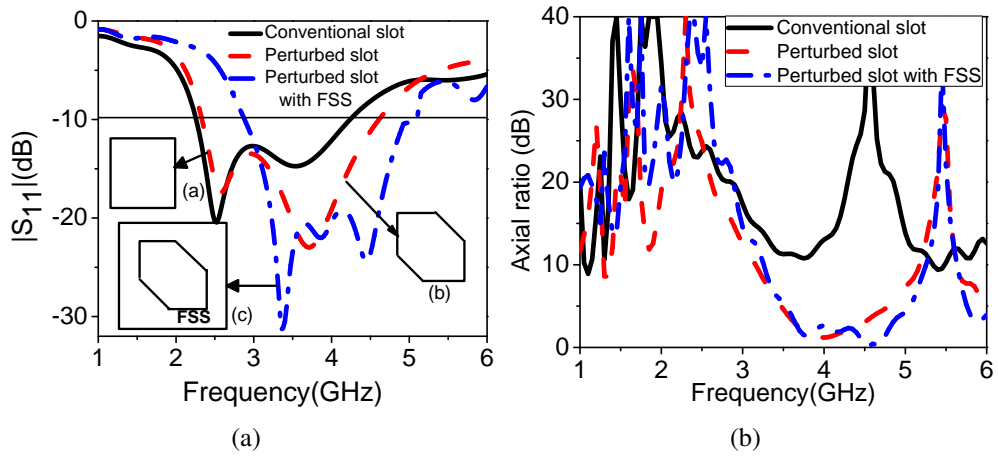


Figure 4.5: Simulation results of reflection coefficient and axial ratio of the antenna design process. (a) $|S_{11}|$ (b) axial ratio.

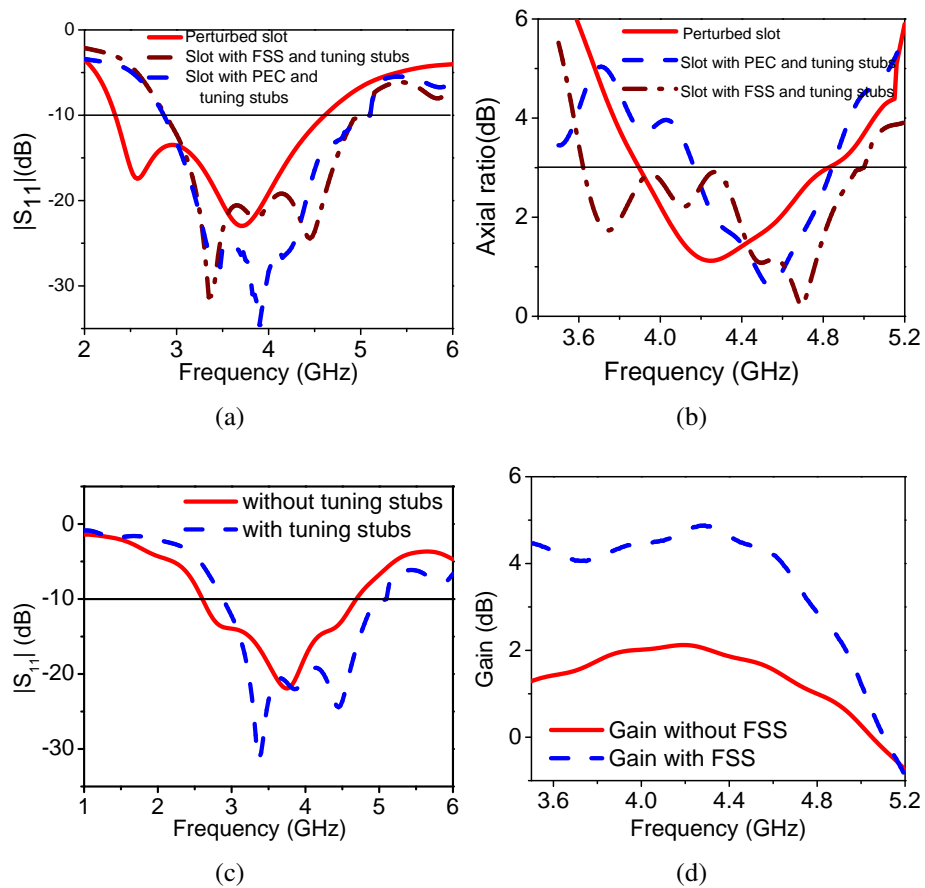


Figure 4.6: Simulation results of reflection coefficient, gain and axial ratio plot of the slot, the slot with PEC, and the slot with FSS. (a) $|S_{11}|$, (b) axial ratio, (c) $|S_{11}|$ of the designed antenna with and without tuning stubs, (d) gain variation of the presented antenna with and without FSS.

effect of PEC or FSS. In Fig. 4.6(b), the perturbed slot antenna has a lesser axial ratio bandwidth than the slot antenna with FSS. This is due to the fact that the forward signal from the slot and the reflected signal from the FSS produces orthogonal fields in the far-field region, producing a wideband CP.

Fig. 4.6(c) shows the simulation results of the reflection coefficient plot of the slot antenna with and without tuning stubs. The optimization is performed using tuning stubs added to CPW feed to obtain better impedance bandwidth. The slot antenna directivity is improved by nearly 3 dB for both PEC and FSS, but improving the axial ratio bandwidth is not possible for PEC. The gain comparison of the perturbed slot and the perturbed slot with FSS is illustrated in Fig. 4.6(d). In the figure, the gain of the perturbed slot is less, which is 1.88 dB at 4.2 GHz because of the bidirectional radiation pattern. The FSS is placed beneath the perturbed slot antenna, which increases the gain up to 4.87 dB. The above comparison infers that the FSS-backed perturbed slot enhances the CP bandwidth and gain.

4.2.2 Fabricated design and Results

The FSS-backed slot antenna is fabricated, and the results are verified in simulation and measurement. Fig. 4.7 shows the fabricated design of the proposed antenna. The simulation and experimental results of reflection coefficient magnitudes are plotted in Fig. 4.8(a). The simulation result of impedance bandwidth is 55.23%, which is obtained from 2.87 GHz to 5.06 GHz. The experimentally measured impedance bandwidth of 63.22% is obtained from 2.65 GHz to 5.10 GHz. The simulation results of 3 dB axial ratio bandwidth is 30.94% which is obtained from 3.66 GHz to 5 GHz, and the measured axial ratio bandwidth of 31.14% is obtained from 3.66 GHz to 5.01 GHz. Fig. 4.8(b) shows the simulation and experimentally verified results of the axial ratio bandwidth and the broadside gain. A peak gain of 4.87 dB is obtained in the broadside direction at 4.2 GHz with a variation of 2 dB gain in the axial ratio bandwidth. Fig.4.9 depicts the simulation and experimentally verified radiation patterns in azimuth and elevation planes for different frequencies. The LHCP and RHCP radiation patterns are matched

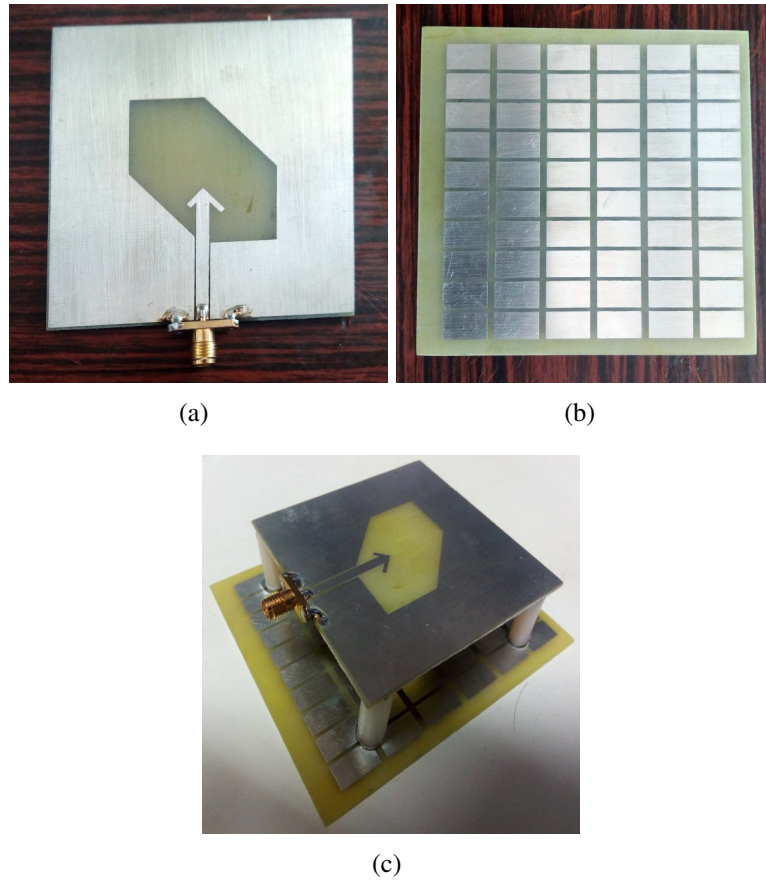


Figure 4.7: Photograph of the fabricated design. (a) Slot antenna, (b) FSS, (c) proposed antenna.

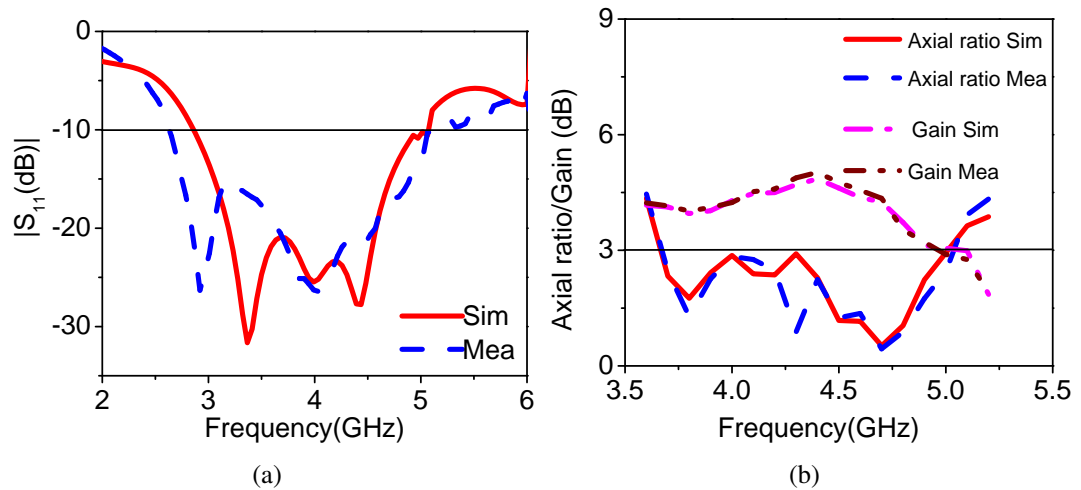


Figure 4.8: Simulation and measured results of reflection coefficient, axial ratio, and gain of the proposed antenna. (a) $|S_{11}|$, (b) axial ratio and gain.

in the simulation and measured results. The LHCP radiation level is 16 dB below the RHCP radiation level in azimuth and elevation planes. The CP radiation is obtained at an angle of 20° concerning to broadside direction. The tilted LHCP radiation is due to the perturbation effect of the slot antenna.

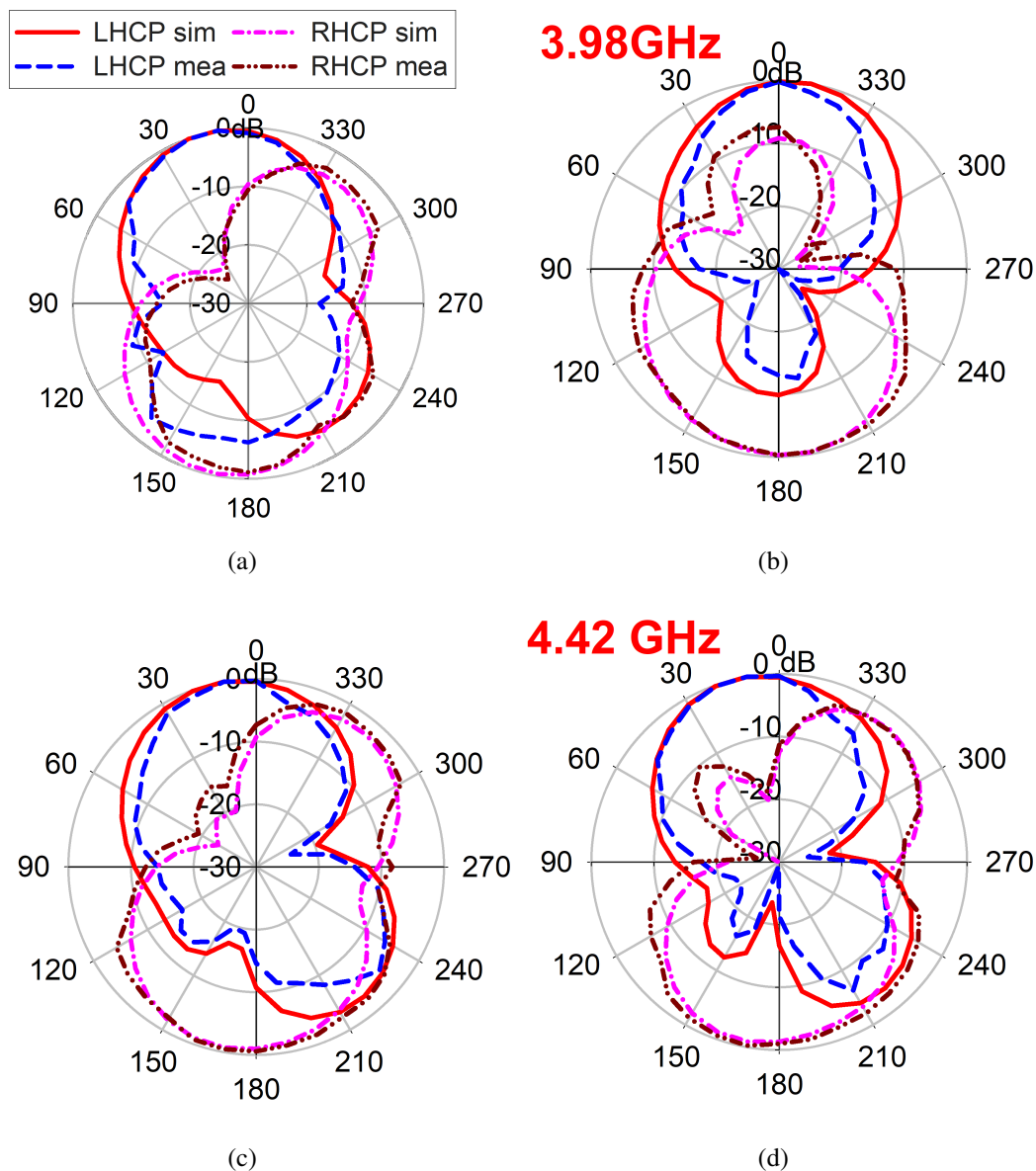


Figure 4.9: Simulation and experimental results of LHCP and RHCP radiation patterns in (a) azimuth plane at 3.98 GHz, (b) elevation plane at 3.98 GHz, (c) azimuth plane at 4.42 GHz, and (d) elevation plane at 4.42 GHz.

4.3 A SRR loaded compact planar slot antenna with circular polarization and wideband characteristics for soil moisture sensor application

This section presents an SRR loaded slot antenna with CPW feeding to obtain wideband CP response. The combined resonances of slot and SRR gives wideband CP. Since the antenna has a single layer, it is utilized to find the moisture content present in the soil. The slot produces two orthogonal modes, which are degenerative in nature to achieve CP at the slot resonance and orthogonal split gaps in the SRR produces CP at the SRR resonance.

4.3.1 Antenna Design and its principle

Fig.4.10 depicts the structure of the SRR loaded slot antenna. The designed antenna is etched on the top surface of the R04003C rogers substrate ($\epsilon_r = 3.38$ and $\tan\delta = 0.0027$) with the thickness of $h = 1.52\text{mm}$. The 50Ω CPW feed is used to excite the slot antenna. Equation (4.1) is used to find the resonance frequency of the slot antenna. R_1 and R_2 are the radius of the inner and outer ring of SRR with a strip width of w . The identical split gaps ($g_1=g_2=g$) are etched on both the rings of the SRR and d is the spacing between two rings. The resonant frequency of 4.62GHz is obtained for the rotated SRR with parameters given by $w_1=w_2=0.5$ mm, $R_2=2.1$ mm, $R_1=2.8$ mm, $d=0.2$ mm, $g_1=g_2=0.4$ mm. The resonance frequency[Saha and Siddiqui (2012)] of the rotated SRR is calculated using the following equation,

$$f_0 = \frac{1}{2\pi \sqrt{L_T \frac{(\pi+q)^2 - \theta^2}{2(\pi+q)} r_{avg} C_{pul}}} \quad (4.3)$$

where, $q = \frac{C_g}{r_{avg} C_{pul}}$, C_{g1} and C_{g2} are the split gap capacitances of two rings, r_{avg} is uniform average dimension of outer and inner ring of SRR, C_{pul} is capacitance per unit length between the rings, θ is the angle of rotation of inner ring with respect to outer ring

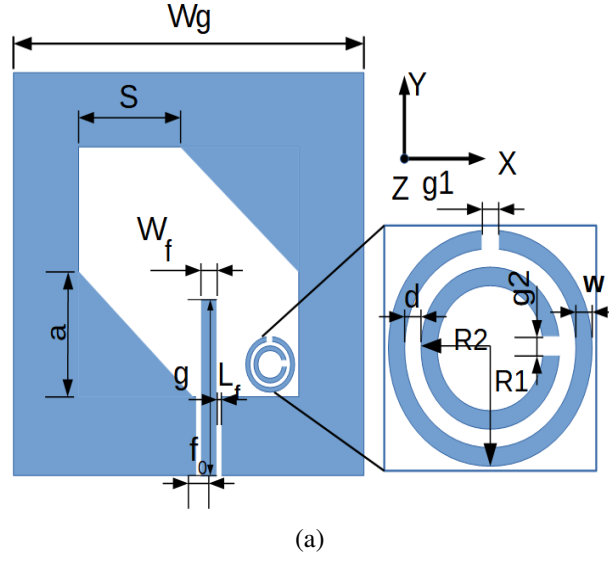


Figure 4.10: Top view of the designed antenna structure. $W_g=70$ mm, $S=26$ mm, $a=8.4$ mm, $W_f=3$ mm, $g=0.3$ mm, $f_0=3$ mm, $L_f=33$ mm

and L_t is the total equivalent inductance of the rings with circumference of $l = 2\pi r_0 - g$ and thickness $w_1=w_2=w$. L_t is calculated using the following equation and it is given by,

$$L_t = 0.0002l(2.303 \log_{10} \frac{4l}{w} - 2.451) \quad (4.4)$$

The corner truncation for CP wave in microstrip patch antennas is common in literature [Sharma and Gupta (1982), Iwasaki et al. (1990), Ta and Park (2015)]. The proposed work presents a CPW fed corner perturbed slot antenna for wideband CP radiation. Fig.4.11 shows the axial ratio and reflection coefficient variation with different perturbation depth. The optimized dimension of the truncation is set as $a=8.4$ mm to get a better axial ratio in the wide frequency range. The slot antenna with a rotated SRR placed on it increases the axial ratio bandwidth. The combination of SRR and slot resonances gives a wide axial ratio bandwidth. The corner perturbed slot gives the resonance at a lower frequency band and it is calculated using equation (4.3). The rotated SRR produces resonance at a higher frequency band and it is calculated from equation (4.4). The optimized axial ratio is obtained in the wide frequency range by tuning the resonances independent to each other. Fig.4.12 depicts the simulation results of the reflection coefficient magnitude and axial ratio curves of the design stages of the proposed antenna. The CPW fed simple square slot (case a) antenna is designed to resonate at

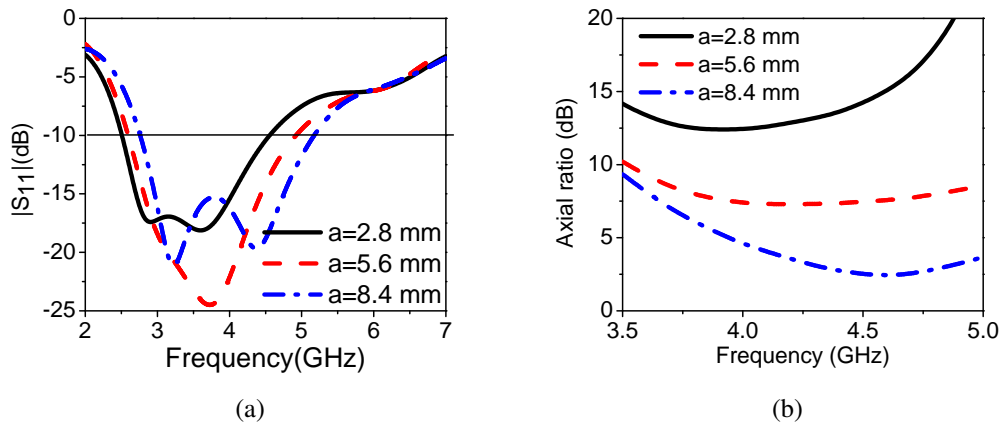


Figure 4.11: Simulation results of reflection coefficient and axial ratio curves of perturbed slot antenna with different values of truncation (a) S_{11} (b) Axial ratio

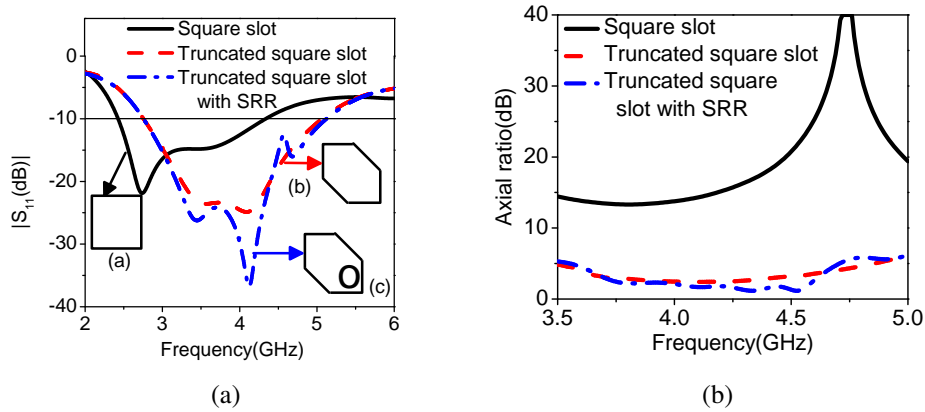


Figure 4.12: Simulation results of reflection coefficient and axial ratio curves of wide-band CP antenna design process (a) S_{11} (b) Axial ratio

2.78 GHz. However, Fig.4.12(b) infers that the axial ratio value of the slot is high and it produces LP radiation. The corner perturbed slot antenna resonates (case b) at 4.12 GHz with better impedance matching over a wide bandwidth with a good axial ratio. The CP bandwidth of 17.69% is achieved due to the corner perturbation of the slot antenna. Further, to enhance the axial ratio over wide operating frequency, the slot antenna is loaded with a rotated SRR. The corner perturbed slot antenna excites the rotated SRR placed on it with its axial magnetic field. The SRR acts as a magnetic dipole and it radiates independently without disturbing slot resonance frequency. The conventional SRR consists of diametrically aligned split gaps in the same axis. When split gaps of SRR

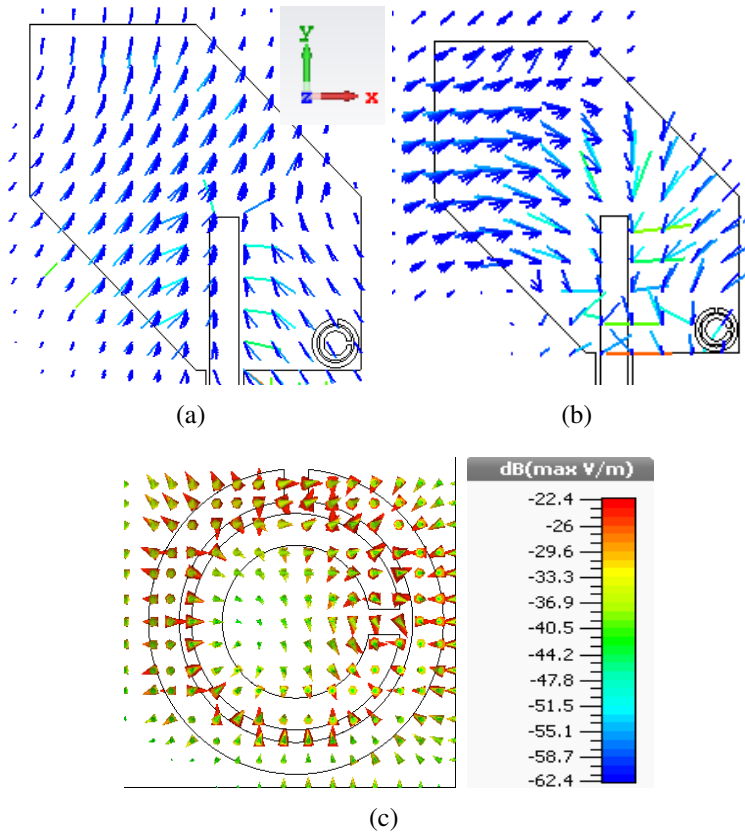


Figure 4.13: Simulated electric field variation at different time instances at slot resonance 4.12 GHz (a) $t=0$ (b) $t=T/4$ (c) Electric field distribution at SRR resonance 4.6 GHz

rings are aligned 90° with each other, they exhibit orthogonal electric fields between two split gaps of the rings that produce CP waves. The good axial ratio is obtained by optimizing the split gaps of the SRR. The perturbed slot antenna loaded with rotated SRR (case c) gives the enhanced axial ratio bandwidth of 21.81%. The resonances of the perturbed slot and rotated SRR are independently tunable by changing the structural dimensions of slot and SRR to optimize the CP bandwidth. Fig.4.13(a) and (b) depicts the electric field distribution of the wideband CP antenna at various time intervals ($t=0$, $T/4$). In the figure, it shows that the radiation from the antenna produces LHCP waves in the $+z$ direction. Fig.4.13(c) illustrates the electric field distribution of the rotated SRR at 4.62 GHz. The figure shows that the electric fields are orthogonal to each other in the two split gaps of inner and outer rings, which produces CP wave at SRR resonance. The CPW feed is shifted with f_o value from the center to optimize the impedance bandwidth. Fig.4.14(a) and (b) shows the variation in reflection coefficient and axial ratio

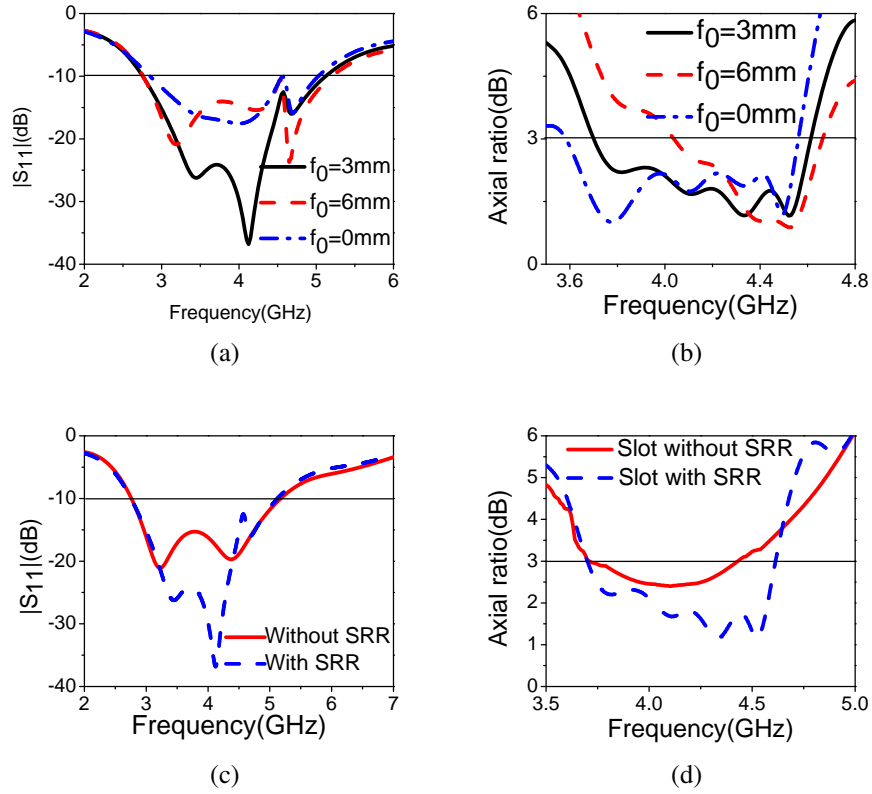


Figure 4.14: Simulation results of reflection coefficient magnitude and axial ratio plot of wideband CP antenna (a) S_{11} of the feed shifted antenna (b) axial ratio of the feed shifted antenna (c) S_{11} plot with and without SRR (d) axial ratio plot with and without SRR

curves. $f_o=3$ mm is chosen to get the optimized impedance matching. Fig.4.14(c) and (d) shows the fractional impedance and CP bandwidth of the antenna with and without loading of SRR on the slot. The SRR placement significantly improves the axial ratio bandwidth, but there is no much effect on the impedance bandwidth.

4.3.2 Fabricated structure and its Results

Fig.4.15(a) shows the photograph of the fabricated structure of the antenna. The simulation results show the impedance bandwidth ($S_{11}<-10$ dB) of 56.36% from 2.77 GHz to 5.10 GHz and measured impedance bandwidth of 61.40% from 2.57 GHz to 5.10 GHz. The simulated axial ratio bandwidth of 0.9 GHz(21.81%) from 3.7 GHz to 4.6 GHz and measured axial ratio bandwidth of 0.9 GHz(21.68%) from 4 GHz to 4.9 is achieved.

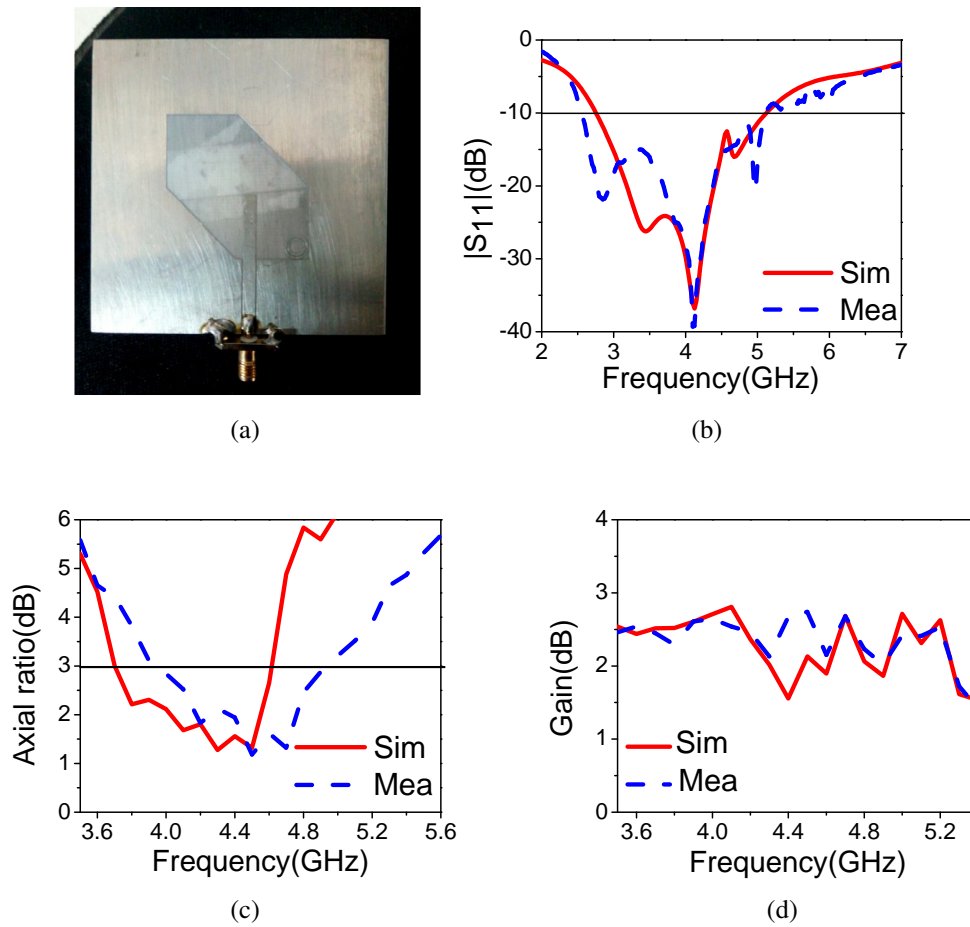


Figure 4.15: (a) Photograph of the fabricated antenna structure (b) simulated and measured reflection coefficient plot (c) measured and simulated plot of axial ratio (d) simulated and measured gain

Fig.4.15(b),(c) and (d) show the comparison between measured and simulated results of the reflection coefficient, gain and axial ratio plots. The measured results show that the peak gain of 2.74 dB is observed at 4.12 GHz, and there is a gain variation of 1 dB over the entire CP bandwidth. Fig.4.16 shows the radiation pattern of the proposed wideband CP antenna in azimuth and elevation planes at 3.8 GHz, 4.12 GHz, and 4.8 GHz. The axial ratio is measured at an angle of 20° with respect to broadside direction. The measured results are in better accordance with the simulated results. The results have little variation due to the losses that occurred in the fabrication errors, SMA connectors and cables used for measurement, which are not taken into account during the simulation.

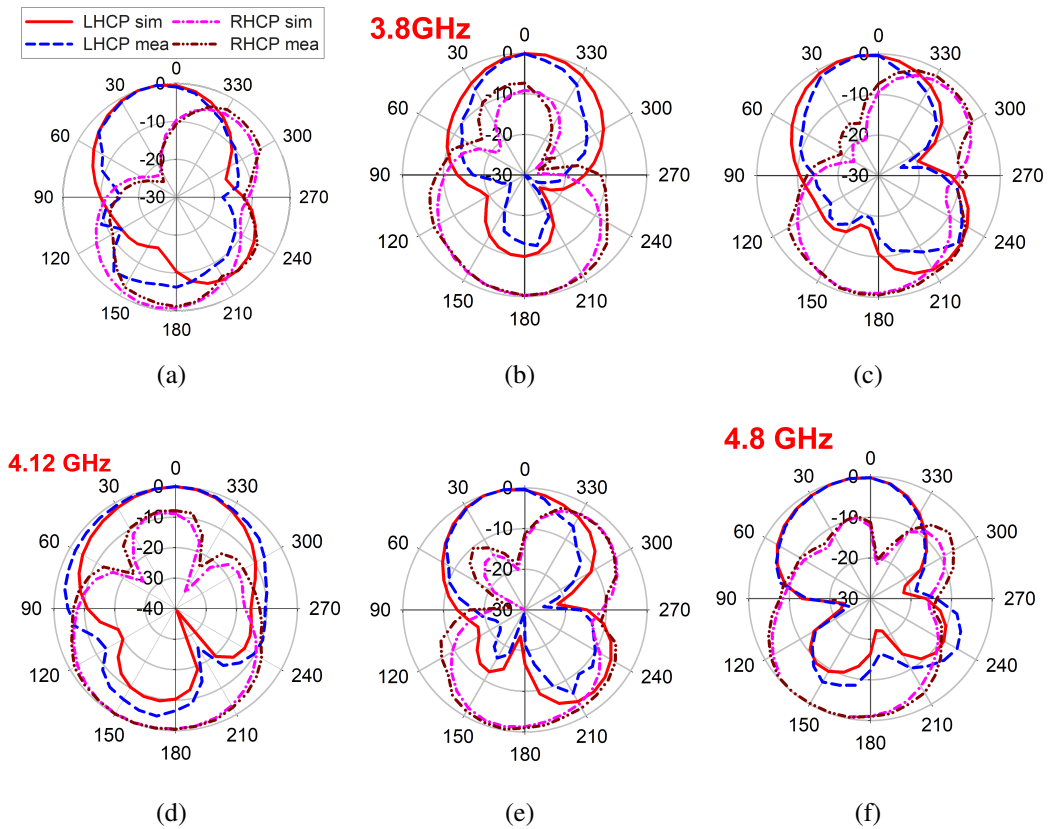


Figure 4.16: Comparison between simulated and measured radiation pattern at different CP frequencies.(a) xz plane at 3.8 GHz (b) yz plane at 3.8 GHz (c) xz plane at 4.12 GHz (d) yz plane at 4.12 GHz (e) xz plane at 4.8 GHz (f) yz plane at 4.8 GHz

4.3.3 Soil sensing application

The proposed wideband CP antenna is a single layer, which is etched on top of the rogers substrate and the backside of the antenna is directly placed on the soil to be tested. The antenna can be shielded with a plastic sheet to avoid short circuit with the water content of the soil. Two types of soil models are simulated based on the change in permittivity of the soil. Dry soil and wet soil have permittivity values of 2.4 and 13.8, respectively [Cataldo et al. (2009)]. The antenna is placed on the testing soil and its reflection coefficient is measured. It is observed from the results that there is a change in the effective permittivity of the antenna, which intern change the resonance frequency. Fig.4.17(a) shows its variation in the reflection coefficient. When the antenna placed on the dry soil, there is no significant variation observed in the reflection coefficient plot.

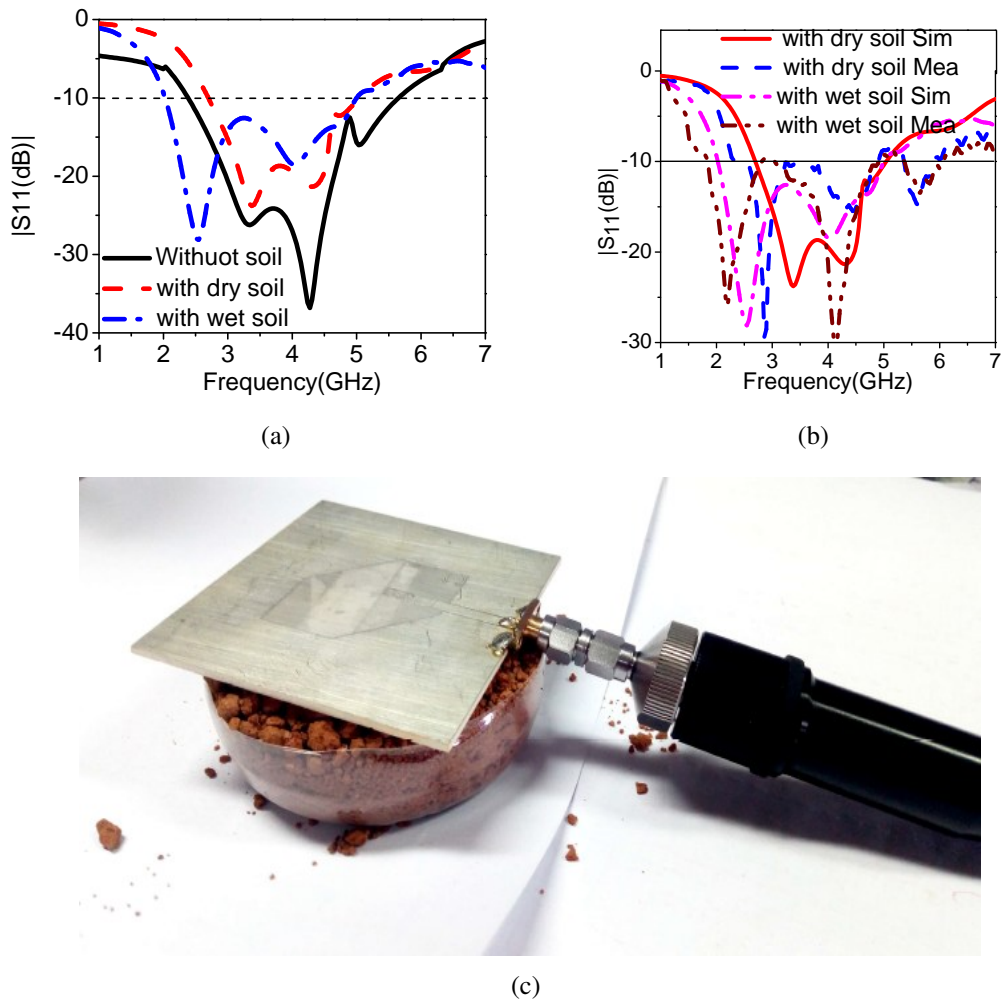


Figure 4.17: (a) Simulated reflection coefficient of wideband CP antenna with and without soil (b) comparison between measured and simulated reflection coefficient of wideband CP antenna with dry and wet soil (c) testing environment

This is due to the permittivity of the dry soil is near to the permittivity of the antenna substrate. In the case of wet soil, the reflection coefficient has more variation due to the high permittivity value of the wet soil and it is measured using a vector network analyzer (VNA). Fig. 4.17(b) shows the reflection coefficient comparison between simulated and measured results of dry and wet soil. In the figure, it is noticed that due to the high permittivity value of the wet soil, the resonance frequency is shifted to lower frequency compared to dry soil. The reflection coefficient variation of dry soil and wet soil can be taken as reference and the moisture content of the soil can be estimated. The measured results of tested soil are in accordance with the simulated results.

To find the exact amount of water, the capacitance principle is used to measure the complex reflection coefficient, Γ of the soil sample. When the water content is added to the soil, the antenna senses the change in capacitance and resonance changes compared to free space. The percentage of moisture content present in the soil can be calculated as

$$Moisture\ content = \frac{M_{water}}{M_{water} + M_{soil}} * 100 \quad (4.5)$$

Where, M_{water} and M_{soil} are the weight of water and weight of dry soil sample, respectively.

4.4 Summary

In this chapter, wideband CP antennas are presented. In the first section, a slot antenna with FSS loading is proposed. The truncated slot antenna achieves an optimized axial ratio but with a low gain. An FSS is used as a reflector to improve the gain and the axial ratio of the truncated slot antenna. The FSS is characterized by its reflection phases for TE and TM incident waves. The proposed antenna achieves 2.44 GHz of measured impedance bandwidth and 1.35 GHz of <3-dB axial ratio bandwidth with a peak gain of 4.87 dB. The proposed design is beneficial for CP applications such as radar, mobile and satellite, over the CP frequency range of 3.66-5.01 GHz. The second section presents a CPW fed single layer truncated square slot antenna loaded with an SRR. The wideband performance is obtained by combining slot and SRR mode resonances. The resonance frequency of each band is independently tunable to achieve optimized wide axial ratio bandwidth. The measured impedance bandwidth of 2.53 GHz and 3-dB axial ratio bandwidth of 0.9 GHz is achieved. The proposed design is useful for soil moisture sensing, military, radar, and microwave sensing application where CP is essential.

CHAPTER 5

HIGH GAIN METASURFACE BASED ANTENNAS WITH CIRCULAR POLARIZATION CHARACTERISTICS

5.1 Introduction

In this chapter, high gain antennas with circular polarization characteristics are designed using zero-index based metasurfaces. In the first section, the gain enhancement of the CP patch antenna is presented. The array of unit cells as a metasurface placed atop of the CP antenna. The performance of the presented design is evaluated with and without metasurface. The second section discusses the gain enhancement of LP antenna along with polarization conversion from LP to CP. The unit cell is designed to achieve polarization conversion and gain improvement. The unit cell's effective parameters are extracted using the algorithm specified in [Szabo et al. (2010)]. The unit cell as an array of the metasurface is placed at an optimum height from the LP antenna to obtain the optimized performance of gain and axial ratio. Finally, both designs are fabricated and verified experimentally. The simulated and experimental results are presented in terms of axial ratio bandwidth, impedance bandwidth, gain, radiation efficiency and radiation patterns.

5.2 A Zero-Index Metasurface Based High Gain Antenna with Circular Polarization Characteristics

In this section, a patch antenna with circular polarization is designed and its gain is enhanced using zero-index based metasurface. A unit cell is analyzed using a periodic

boundary condition and its effective parameters are extracted. An array of unit cells are arranged and placed atop of the CP patch antenna to enhance the gain.

5.2.1 Structure and operating principle of the antenna

Fig.5.1 shows the proposed unit cell structure. It consists of symmetrically centered extended swastika-shaped slots on the top and a ring with a split gap on the bottom of a low-cost FR4 substrate with a thickness of $h_s=0.76$ mm. ($\epsilon_r=4.3$ and $\tan\delta=0.025$). A plane wave is incident normal to the top surface of the unit-cell. The effective parameters of the unit-cell are extracted are shown in Fig.5.2.

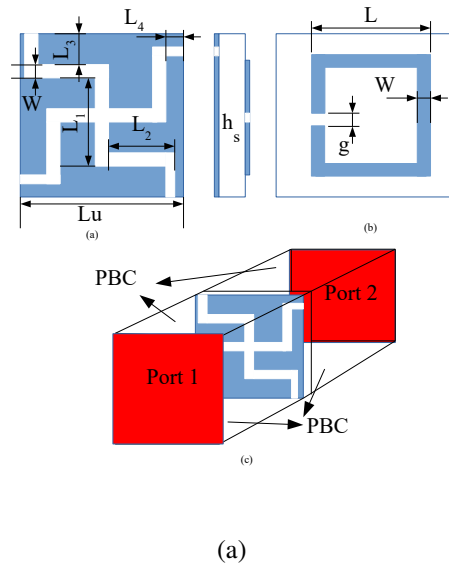


Figure 5.1: Proposed unit-cell geometry. (a) Front view (b) Back view (c) Boundary condition. $L_u=8.5$ mm, $L_1=4.5$ mm, $L_2=3.7$ mm, $L_3 = L_4=1.75$ mm, $L= 5$ mm, $W=0.4$ mm, $g=0.4$ mm, $h_s=0.8$ mm.

In the figure, the unit cell gives a zero refractive index at 7.47 GHz. The zero refractive index MTS has no phase variation at the surface and focuses the energy towards the direction normal to its interface. This property of the unit-cell can be used to enhance the gain of any primary source. The array of 9×9 unit cells used as a MTS, and it is placed at the height of h_{am} from the patch antenna. The MTS is placed at a suitable height from the patch antenna to achieve optimized gain. Fig.5.3 shows the designed antenna structure. The patch antenna is printed on the top layer of rogers RO4003C

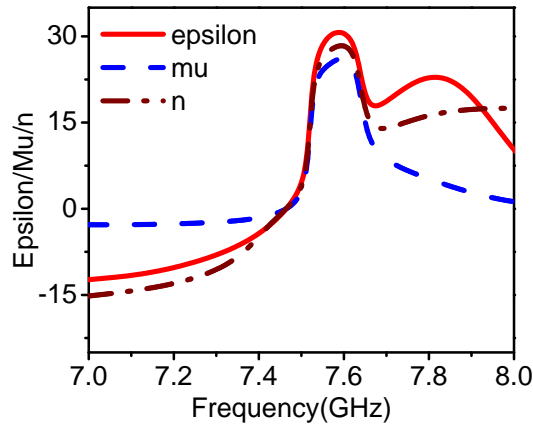


Figure 5.2: Effective parameters of the proposed unit-cell.

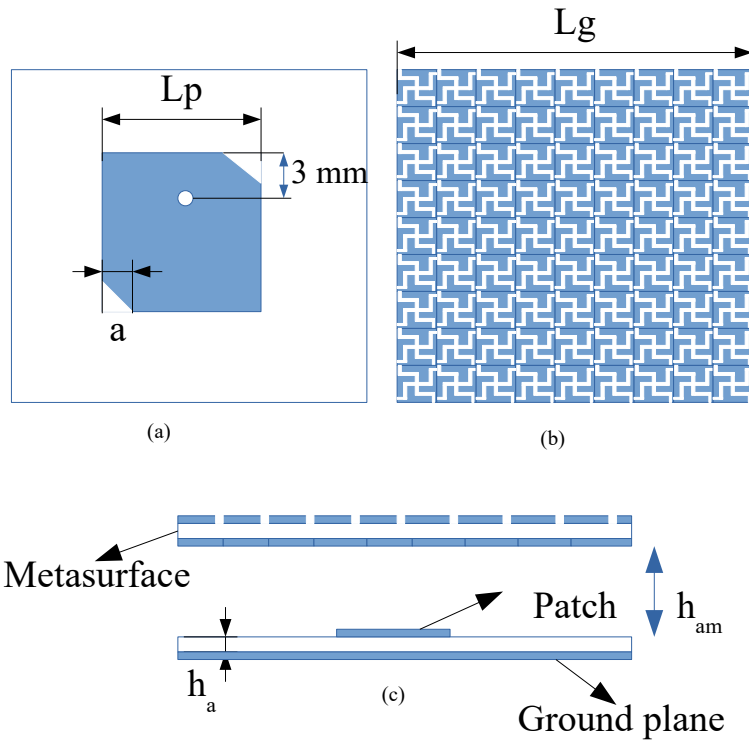


Figure 5.3: Proposed antenna geometry. (a) patch antenna (b) zero-index based MTS (c) side view of the high gain CP antenna. $L_p=10.6$ mm, $a=1$ mm, $L_g=76.5$ mm, $h_{am}=21.5$ mm, $h_a=0.508$ mm.

substrate ($\epsilon_r=3.38$, $\tan\delta=0.0027$) with a thickness of $h_a=0.508$ mm. The square patch antenna is operated at 7.5 GHz resonance frequency. The two corners of the patch

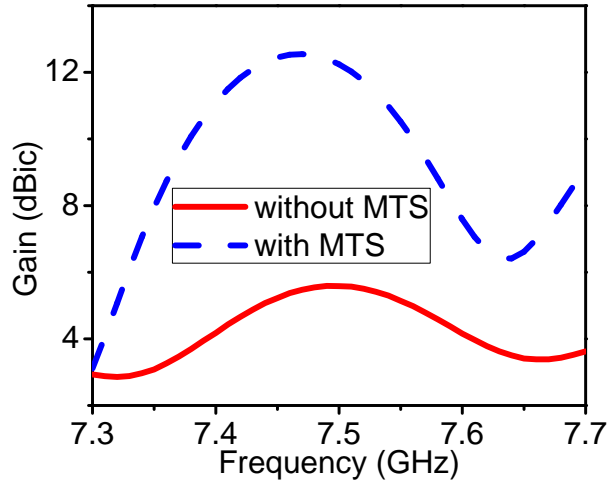


Figure 5.4: Simulated gain comparison of the proposed antenna with and without MTS.

antenna are perturbed to get two orthogonal modes required to achieve circular polarization. As per the Snell-Descartes principle [Enoch et al. (2002)], the incident waves from the CP patch antenna at the grazing angle on the zero-index MTS refract the waves towards the direction normal to the MTS interface. This focusing effect of the MTS increases the gain of the patch antenna intern, increasing the overall gain of the antenna. The proposed antenna with and without MTS is shown in Fig.5.4. The patch antenna gain without MTS is around 5-6 dB. The gain is enhanced by 5-6 dB by placing the MTS atop of the CP patch antenna.

5.2.2 Experimental results and discussion

The design is fabricated and its photograph is shown in Fig.5.5. Simulated impedance bandwidth of 360 MHz is obtained from 7.37 GHz-7.73 GHz. The impedance bandwidth of 530 MHz is achieved from 7.2 GHz- 7.73 GHz experimentally. The measured and simulation results of impedance bandwidth are shown in Fig. 5.6(a). Fig. 5.6(b) illustrates the simulated and measured axial ratio bandwidth of 100 MHz. Measured peak gain of 12.15 dBiC is achieved at 7.47 GHz. The simulated and measured gain is shown in Fig.5.7(a). Simulation results are in accordance with the measured results. Fig. 5.7(b) shows the simulated radiation efficiency of around 80% in the overlapped impedance and axial ratio bandwidth.

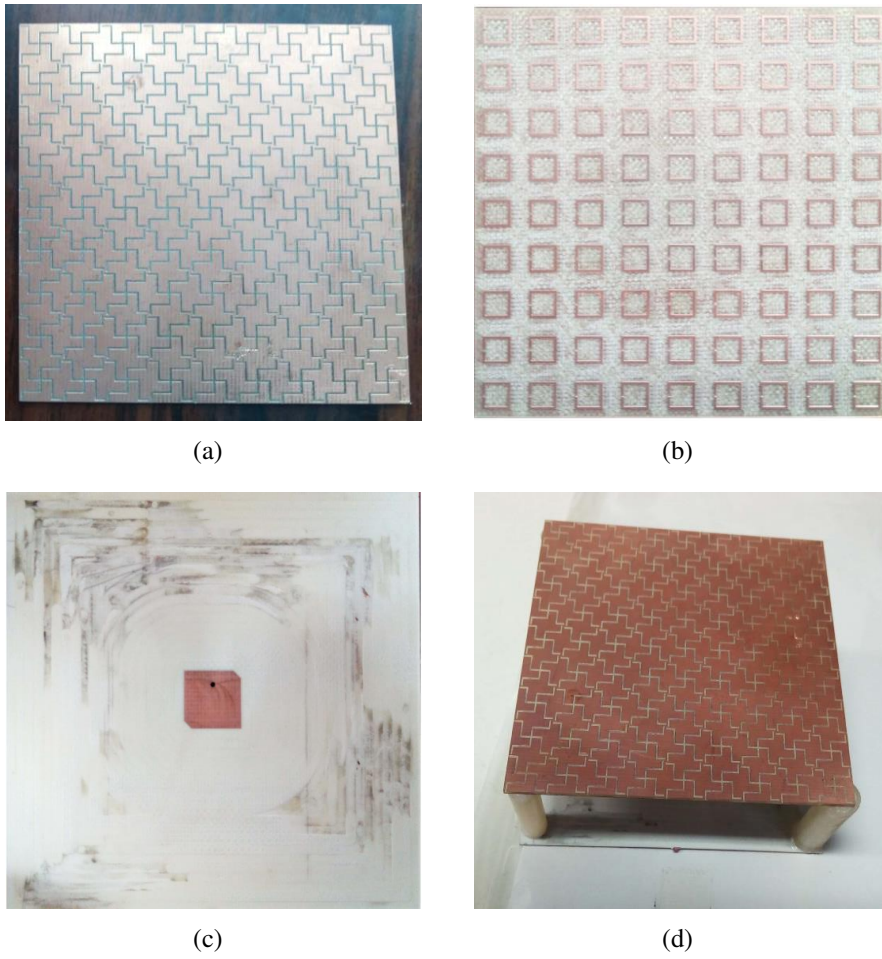


Figure 5.5: Fabricated prototype (a) MTS front view (b) MTS back view (c) Patch antenna (d) Proposed high gain CP antenna

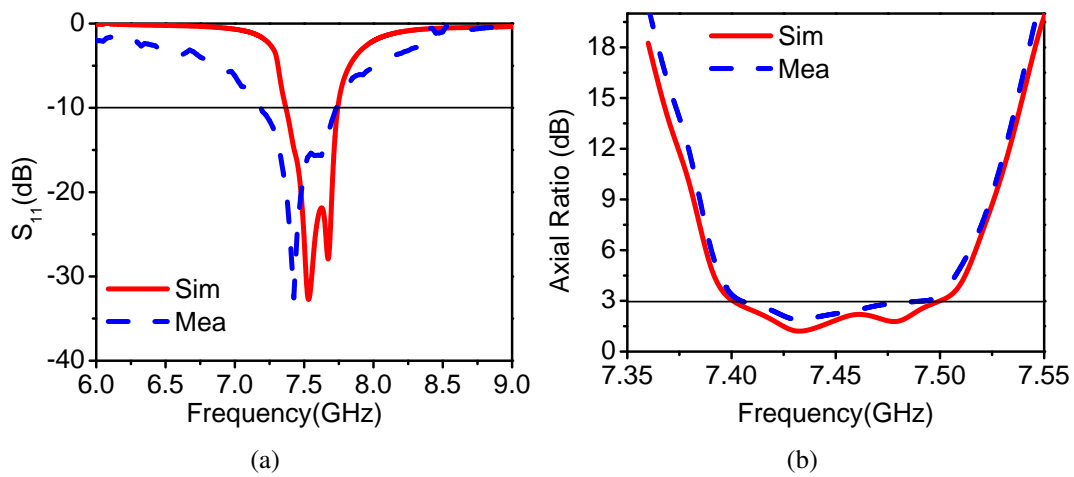


Figure 5.6: Comparison between measured and simulated reflection coefficient and axial ratio. (a) S_{11} (b) axial ratio

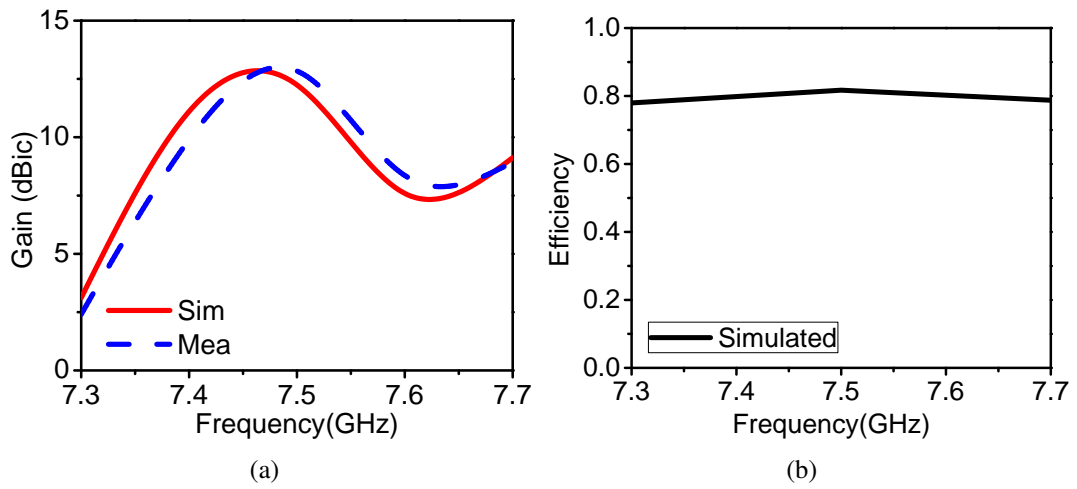


Figure 5.7: (a) Comparison between simulated and measured gain (b) simulated radiation efficiency

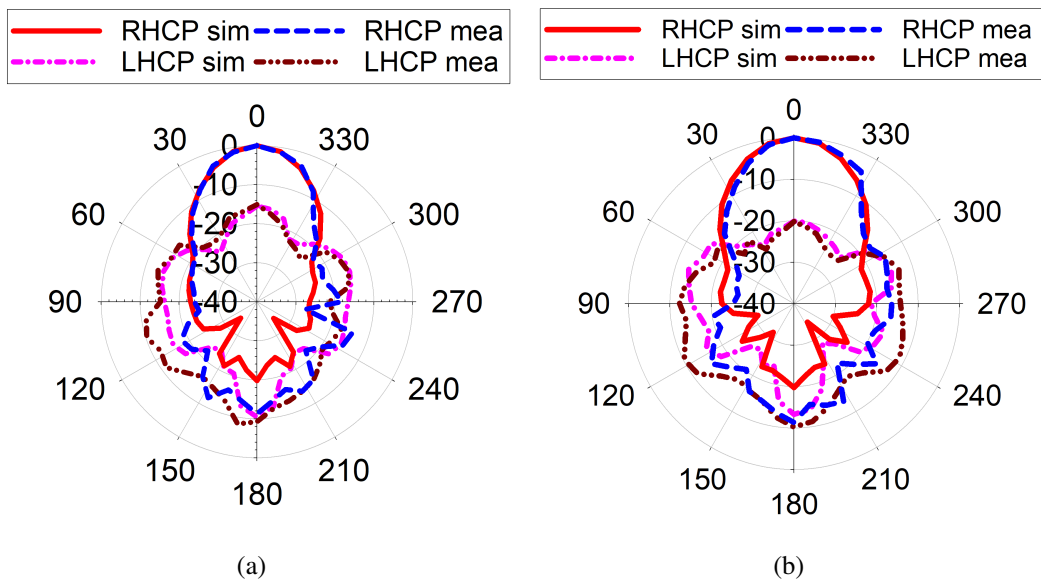


Figure 5.8: Comparison between measured and simulated radiation patterns at 7.5 GHz (a) xz plane (b) yz plane

The measured and simulated radiation pattern of the high gain CP antenna in two principle planes is shown in Fig. 5.8. The cross-polarization level of 15 dB is obtained in both the principal planes. A little discrepancy in the simulated and experimental results is due to measurement and connector losses.

5.3 A zero index metasurface based high gain antenna with polarization conversion

In this design, a novel ZIM is proposed to gain enhancement as well as linear to circular polarization conversion. The proposed ZIM reduces the complexity and overall weight of the antenna. A square ring with two asymmetric splits unit-cell is designed to achieve near-zero effective permittivity and permeability. This ZIM improves the gain of a linearly polarized patch antenna placed at nearly $\lambda_0/2$ (where $\lambda_0=c/f$ is free space wavelength) distance. The CP is obtained by the asymmetrical split gaps on the rings, which produce two orthogonal electric field components and produce CP waves. The proposed antenna has a simple geometry with high gain and good axial ratio bandwidth.

5.3.1 Antenna Design and Operating Principle

Unit cell design

The structure of the proposed ZIM unit-cell is shown in Fig. 5.9(a). FR4 substrate ($\epsilon_r=4.3$ and $\tan\delta=0.025$) with a thickness of $h_u=0.8$ mm is used to design the ZIM. The unit cell consists of two identical square rings with asymmetrical split gaps. The rings are printed on the top and bottom of the FR4 substrate. The dimensions of the unit cell are $a=8.5$ mm, $b=5$ mm, $c=0.3$ mm, $g_1=0.4$ mm and $g_2=0.6$ mm.

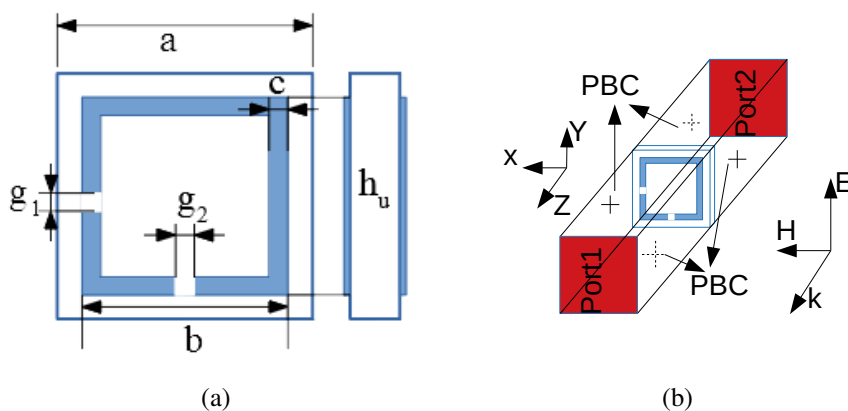


Figure 5.9: (a) Proposed ZIM based unit cell geometry (b) Simulation set-up

The unit cell is simulated using CST microwave studio. Fig. 5.9(b) shows the simulation setup with boundary conditions. A plane wave which has propagation vector k parallel to the z -direction is incident on the unit cell, and periodic boundary condition (PBC) is applied to x and y directions. The simulated magnitude and phase plot of reflection and transmission coefficients are presented in Fig. 5.10(a) and Fig. 5.10(b). The figure shows that the unit cell resonates at 7.45 GHz. At the resonance, the transmission coefficient magnitude value is equal for both x and y polarization. The constituent material parameters are extracted from simulated reflection and transmission coefficient. Fig. 5.10(c) and 5.10(d) shows the extracted effective material parameters. The real and imaginary part of the refractive index value is zero at the resonance frequency. At this resonance frequency, the incident electromagnetic wave does not change its phase, and ZIM focuses the wave to the direction normal to its interface. The periodic arrangement of the designed unit-cells as an array of 9×9 can be used as a superstrate atop of any primary source antenna to enhance the overall gain.

Linear to circular polarization conversion capability of the proposed ZIM is explained using the transmission coefficients of x and y polarized incident waves. Fig.5.10 shows the transmission coefficient magnitudes ($|T_x|$ and $|T_y|$) and corresponding phases (ϕ_{Tx} and ϕ_{Ty}) for the applied x and y polarized incident wave. When $|T_x|$ and $|T_y|$ are equal in magnitude and $\phi_{Tx} - \phi_{Ty} = \pm 90^\circ$, then ZIM converts linearly polarized incident waves into circularly polarized waves. From Fig. 5.10, it is observed that the transmission magnitude is equal at 7.45 GHz for the applied x and y polarized wave, but the phase difference between the two polarization is nearly 90° . According to [Balanis (2005)] the axial ratio is calculated as,

$$AR = \frac{|T_x|^2 + |T_y|^2 + \sqrt{a}}{|T_x|^2 + |T_y|^2 - \sqrt{a}} \quad (5.1)$$

where $a = |T_x|^4 + |T_y|^4 + 2|T_x|^2|T_y|^2 \cos(2(\phi_{Tx} - \phi_{Ty}))$ The transmission phase difference of nearly 90° is obtained from 7.1 GHz to 7.5 GHz. In this operating band, the axial ratio can be obtained below 3 dB for incident waves. The periodic arrangement of the proposed unit cell combined with linearly polarized microstrip patch antenna produce

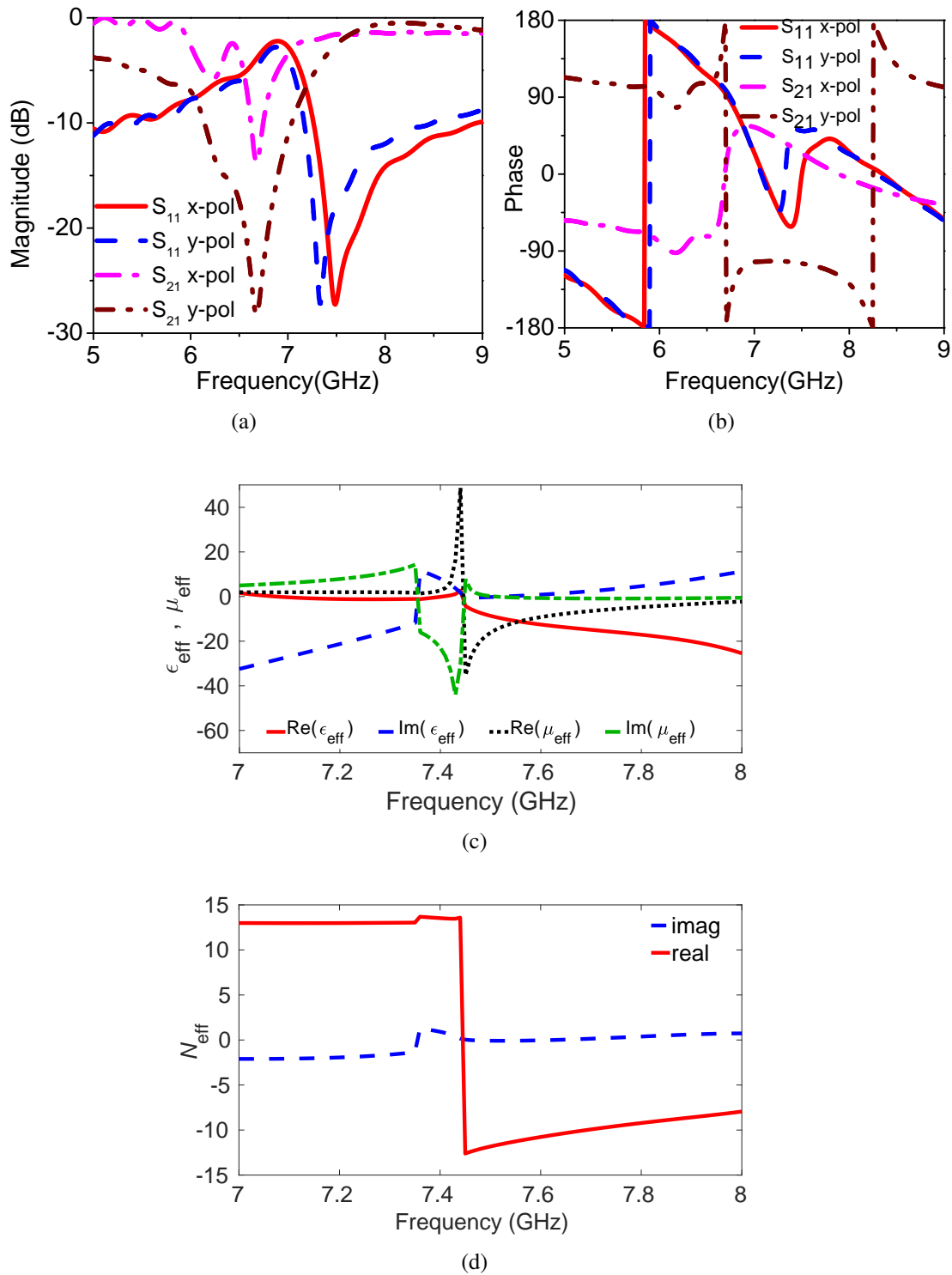


Figure 5.10: Simulated reflection and transmission coefficient and extracted parameters of the unit cell. (a) Magnitude curves of S_{11} and S_{21} . (b) Phase curves of S_{11} and S_{21} . (c) Effective permeability and permittivity. (d) Refractive index.

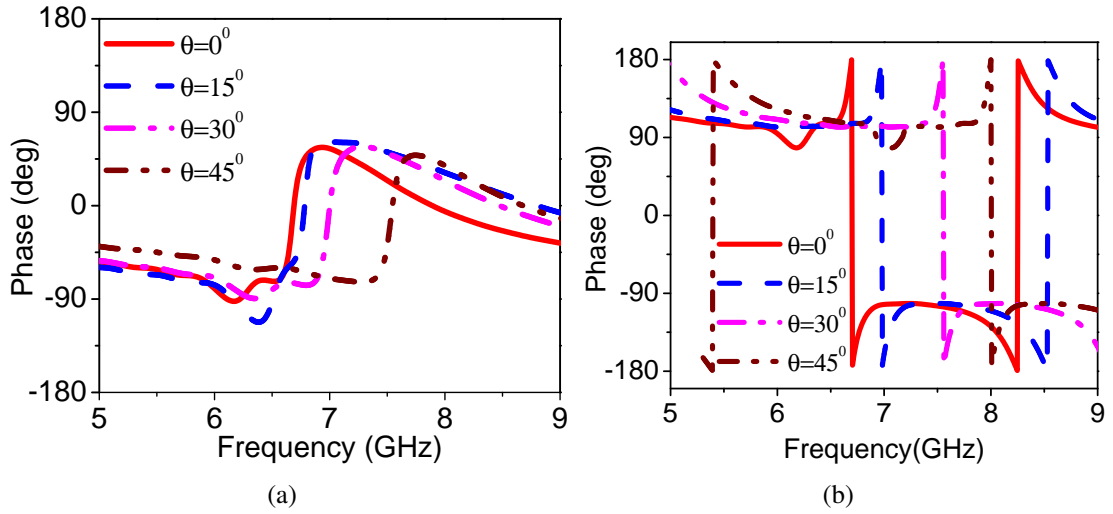


Figure 5.11: Transmission coefficient phase variation of the unit-cell for oblique plane wave incidence. (a) Transmission coefficient phase of x-component. (b) Transmission coefficient phase of y-component.

CP wave with gain enhancement. Fig.5.11 shows the angular stability of the unit-cell. The transmission phase difference of 90° is maintained up to the incidence angle of 30° . This shows that the unit-cell gives stable characteristics for oblique incidence.

High Gain CP Antenna

The schematic diagram of the proposed ZIM based high gain CP antenna and its geometric parameters are shown in Fig. 5.12. The antenna structure consists of a co-axial line fed microstrip patch and the array of ZIM unit cells. The substrate used to design the patch antenna is RTduroid 5880 ($\epsilon_r=2.2$ and $\tan\delta=0.0027$) with a thickness of 1.52 mm. The patch antenna resonates at 7.45 GHz. The 9×9 array of ZIM unit cells are placed at the height of 23.3 mm from the patch antenna. The array of ZIM unit cells provides the zero refractive index around the resonance of the patch, as discussed in section II A. According to the Snell-Descartes principle [Enoch et al. (2002)], radiation from the patch antenna incident on the ZIM surface with a grazing angle will be refracted towards the broadside direction. This focusing effect of ZIM increases the gain of the patch about 5-6 dB. On the other hand, in the Fabry Perot cavity (FPC) based high gain antennas work according to the cavity resonant condition to enhance the gain

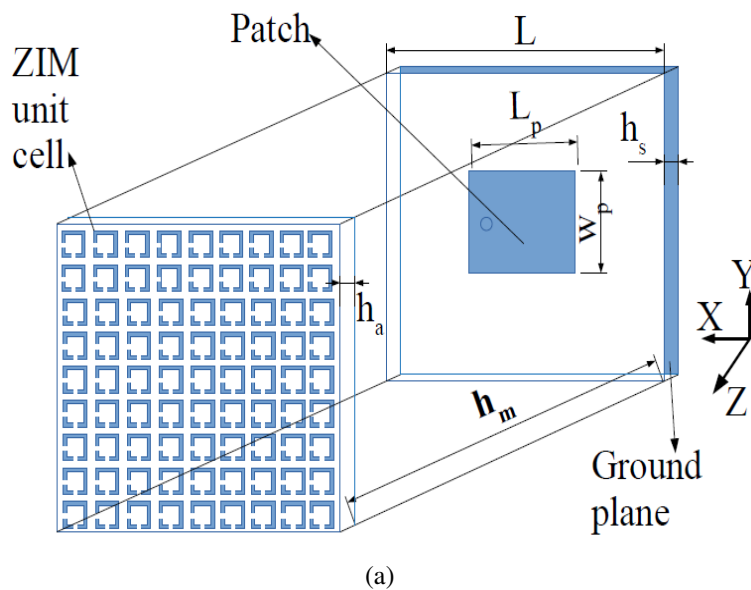


Figure 5.12: Proposed high-gain antenna with ZIM unit cells. $L = 76.5$ mm, $L_p = 12.6$ mm, $W_p = 12.2$ mm, $h_m = 22.3$ mm, $h_a = 0.8$ mm, and $h_s = 1.52$ mm.

[Feresidis et al. (2005)]. Here, a partially reflective surface is used as a cavity resonator to reflect the primary source antenna signal. The height of the cavity is optimized for constructive interference of the reflected signal and primary radiation.

The gain of the patch with and without ZIM loading are shown in Fig.5.13(a). It is observed that the gain of the patch antenna is about 6 dB over the impedance bandwidth. By introducing the ZIM as MTS over patch antenna, the gain is increased up to 12.31 dBiC. The ZIM increases the aperture efficiency and due to the zero refractive index, it focuses the incoming wave to broadside direction, thereby increasing the gain. The circular polarization is obtained by the excitation of two modes with equal amplitude and 90° phase difference, which is created by the two asymmetrical split gaps in the ZIM surface. The gap variation of two asymmetrical splits is optimized to get better axial ratio performance. As shown in Fig.5.13(b), the axial ratio of the conventional rectangular patch antenna has a high value of the axial ratio. After introducing ZIM upon patch antenna, the axial ratio improves and achieves less than 3 dB over the entire impedance bandwidth. This shows that the ZIM acts as a polarization converter as well as it improves the gain. Fig.5.14 shows that the portion of MTS surface current

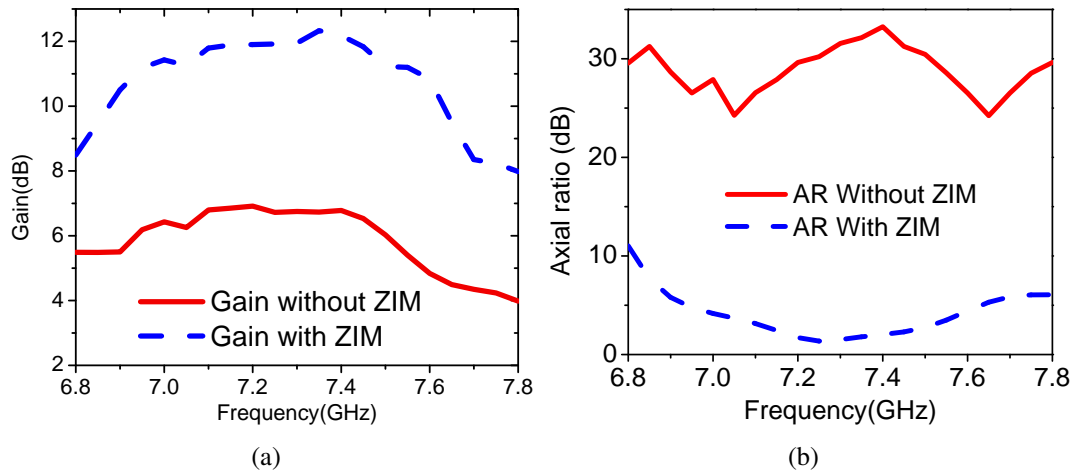


Figure 5.13: Simulated gain and axial ratio variation of the proposed antenna with and without ZIM. (a) Gain. (b) Axial ratio.

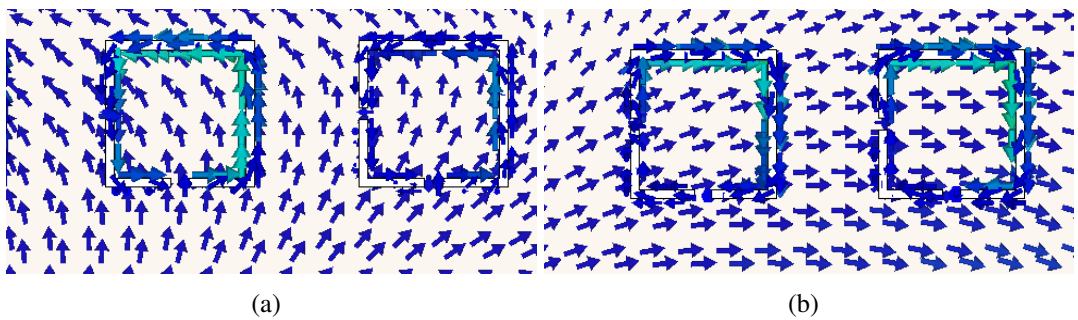


Figure 5.14: Simulated surface current distribution of a portion of the MTS at different time instants. (a) $\omega t = 0^\circ$. (b) $\omega t = 90^\circ$

distribution in the $+z$ -direction at different time intervals ($\omega t = 0^\circ$ and $\omega t = 90^\circ$). From the figure, the observation shows that the current vector rotates in the clockwise direction and produces left hand CP (LHCP) waves.

Parametric study

It is essential to do the parametric variation of the proposed antenna to analyze the sensitiveness of parameters, which contributes to the gain and axial ratio performance. The reflection coefficient magnitude and axial ratio plots for different split gap values are given in Fig. 5.15 and Fig. 5.16. It is observed from figures, there is no much variation in the reflection coefficient, but there is a significant change in the axial ratio for a little

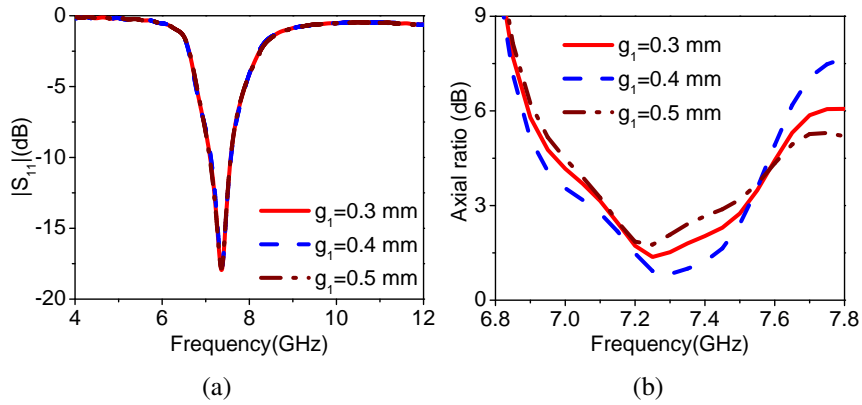


Figure 5.15: (a) Reflection coefficient plot variation for split gap g_1 (b) Axial ratio plot variation for split gap g_1 .

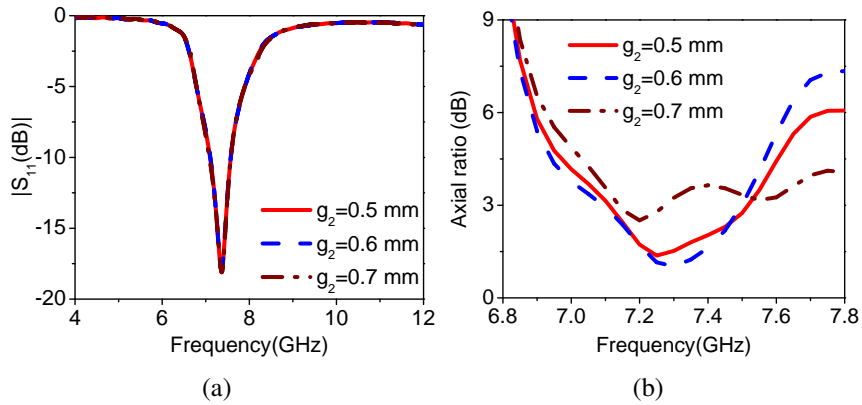


Figure 5.16: (a) Reflection coefficient plot variation for split gap g_2 (b) Axial ratio plot variation for split gap g_2 .

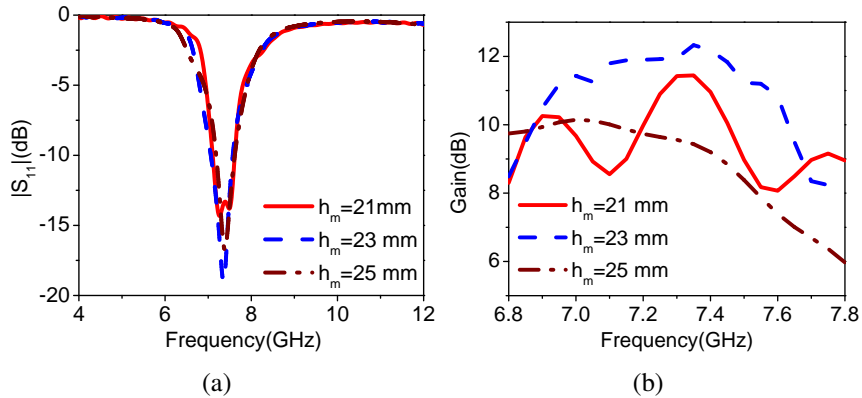


Figure 5.17: (a) Reflection coefficient plot for different height between patch and ZIM.(b) Gain plot for different height between patch and ZIM.

variation in both the split gaps. The optimum gap dimension helps to achieve a better axial ratio. The change in reflection coefficient and gain variations with respect to different height (h_m) between patch and ZIM is shown in Fig. 5.17. The gain is changing with the function of height, so the optimum height is selected for better gain value. The prototype of the proposed high gain CP antenna is fabricated and its performance is tested experimentally. Fig.5.18 shows the photograph of the proposed antenna prototype. The Teflon rods are used as a mechanical supporting structure to form the air gap between patch and ZIM.

5.3.2 Results and Discussion

The simulated and experimental results are compared regarding impedance bandwidth, axial ratio bandwidth, and gain. The simulated and measured reflection coefficient magnitudes are shown in Fig.5.19(a). The simulation results give the impedance bandwidth of 6.87% from 7.11 GHz to 7.56 GHz is observed. The experimental results give the measured impedance bandwidth of 8.69% is obtained from 7.04 GHz to 7.68 GHz. The measured and simulated axial ratio bandwidth curves are presented in Fig.5.19(b). The <3 -dB axial ratio bandwidth for both simulation and measurement is observed from 7.11 GHz to 7.56 GHz. Also, the measured and simulated gain plot is shown in the same figure. The measured peak gain of 12.31 dBic is achieved at the resonance frequency of 7.4 GHz. The observation from the figures shows that the simulation results

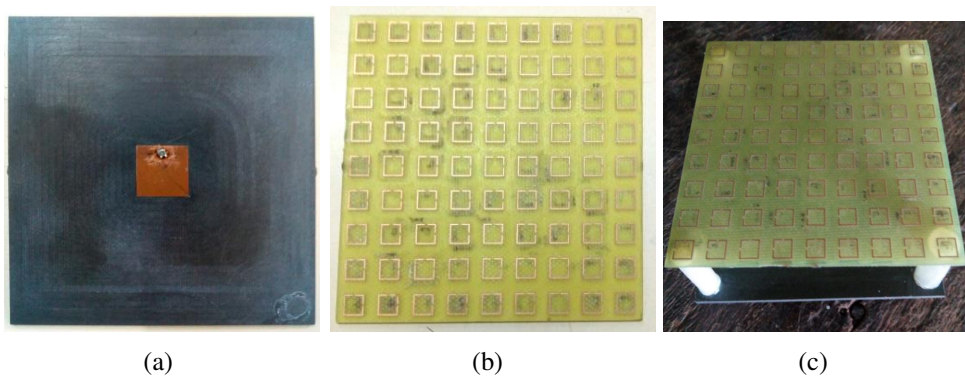


Figure 5.18: Fabricated high-gain CP antenna. (a) Patch antenna. (b) Double-sided 9×9 ZIM unit cells. (c) Proposed high-gain CP antenna.

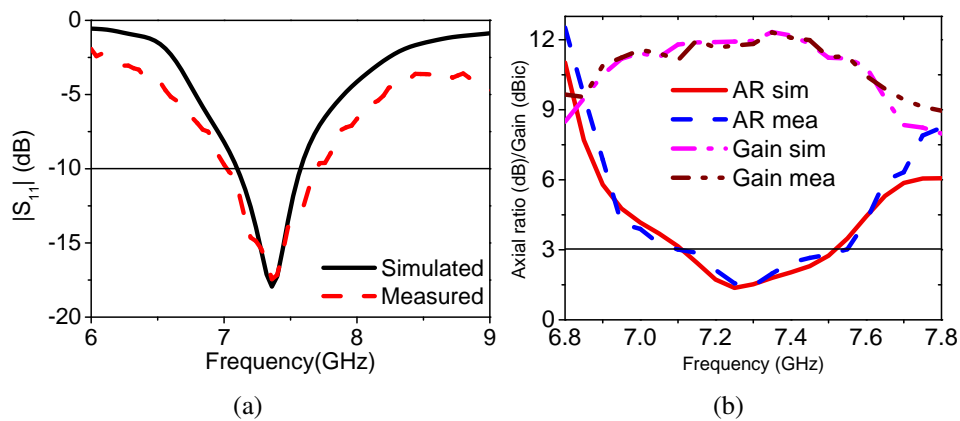


Figure 5.19: Comparison between measured and simulated (a) Reflection coefficient (b) Axial ratio and gain

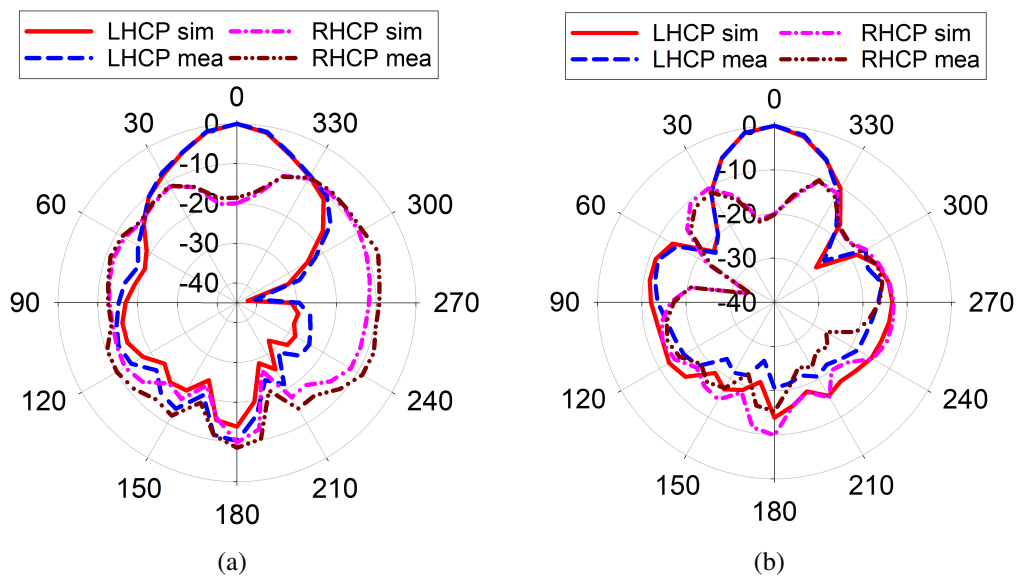


Figure 5.20: Radiation pattern of the proposed antenna at 7.4 GHz. (a) xz plane. (b) yz plane.

are in accordance with the measured results and 1-dB gain variation is observed over the entire CP bandwidth. The simulated and measured radiation patterns of the antenna in both azimuth and elevation planes are shown in Fig.5.20. The radiated waves from the antennas are the LHCP waves in +z direction. RHCP is the cross-polarization field. The RHCP level is -20 dB less compared to the LHCP level and the front to back (FB) ratio of 12 dB is achieved in both planes. The 3-dB angular beamwidth of 30.6° and 29.8° is obtained in xz and yz planes, respectively. The directivity can be calculated using 3-dB

beamwidth as [Balanis (2005)],

$$D = 10 \log(41000/\Delta\theta\Delta\phi) = 16.61dB \quad (5.2)$$

Theoretically, the equation used to calculate the maximum directivity of any aperture antenna is given by

$$D_{max} = 10 \log(4\pi A\lambda_0^2) = 16.43dB \quad (5.3)$$

where $\lambda_0=c/f$ and $A=76.5 \text{ mm} \times 76.5 \text{ mm}$ (in the proposed antenna).The theoretical value is comparable to the measured directivity of the proposed antenna. This shows the capability of proposed design with the directivity of the same size antenna, which is physically realizable. Table 5.1 provides a comparison between existing literature and the proposed high gain CP antenna. The measured results are in accordance with simulated results regarding CP bandwidth, impedance bandwidth and gain with slight variation due to connector losses and measurement errors.

Table 5.1: The performance metrics comparison between the high gain CP antenna and existing literature

Ref.	Size	Impedance band-width (%)	Axial ratio band-width (%)	Gain	Gain-enhanced method
[Majumder et al. (2016)]	$0.108\lambda_0^3$	14	—	11.3	Double layer metasurface
[Singh et al. (2017)]	$2.88\lambda_0^3$	5	—	12.5	Fabry Perot Cavity resonator
[Liu et al. (2015)]	$0.21\lambda_0^3$	8.1	—	10.6	Fabry Perot Cavity resonator
[Ren et al. (2018)]	$2.84\lambda_0^3$	2.63	1.12	9.5	Fabry Perot Cavity resonator
Proposed work	$2.09\lambda_0^3$	8.69	6.87	12.31	ZIM

5.3.3 Summary

High gain CP antennas using Zero-Index based metasurfaces are discussed. The zero index property of metasurface focuses the incoming waves into the direction normal to the interface and acts as a focusing lens. In the first design, the gain of the CP patch antenna is enhanced using swastika and ring-shaped unit cells, which provides the zero refractive index at the CP bandwidth. In the second design, the double square split ring-shaped unit cell is analyzed to obtain zero-index property and polarization conversion simultaneously. The gain enhancement of the LP patch antenna is presented along with polarization conversion from LP waves into CP waves.

CHAPTER 6

MULTIBAND ANTENNAS WITH CIRCULAR POLARIZATION CHARACTERISTICS

6.1 Introduction

In the first section of this chapter, a CP slot antenna loaded with asymmetric cross strips for dual-band application is discussed. The slot resonance provides a lower band and a pair of asymmetric cross strips resonate at the higher band. The truncated slot alone gives CP at the lower frequency band and a combination of slot mode and strip mode gives CP at the higher frequency band. The novelty of the proposed design is that it achieves CP bands with an axial ratio above 10% with its simple geometry. In the second section, a triband CP antenna with the independent tuning of each frequency band is proposed. The corner truncated slot provides CP at the first band and a rotated SRR gives a CP at the second band. The inner ring is rotated 90^0 with respect to the outer ring provides orthogonal fields to produce CP at the second band. The CP in the third band is achieved by introducing orthogonal micro-splits in both the rings of the rotated SRR. Finally, both the designs are fabricated and performance metrics are verified in-terms of axial ratio bandwidth, impedance bandwidth, gain and radiation patterns experimentally.

6.2 Dual Band CP antenna Using Asymmetric Cross Strips

A simple and compact design of CP antenna loaded with asymmetric cross strips for dual-band application is presented in this section. The first band is achieved by a truncated slot antenna, which produces two orthogonal modes that are in degenerative nature to produce CP. The second band is achieved due to asymmetric cross strips. The

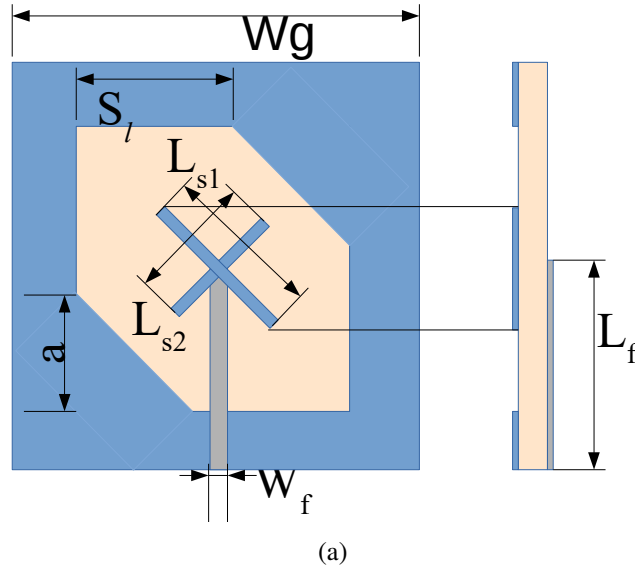


Figure 6.1: The proposed antenna geometry. $W_g=70\text{mm}$, $S_t=29.6\text{mm}$, $a=8.4\text{mm}$, $W_f=2.5\text{mm}$, $L_f=34.5\text{mm}$, $L_{s1}=26\text{mm}$, $L_{s2}=24\text{mm}$

combination of slot and strip mode gives CP in this band. The proposed design is compact and gives axial ratio bandwidth $>10\%$ in both the bands.

6.2.1 Working principle of the antenna and its structure

Fig.6.1 shows the antenna structure and it consists of the slot, asymmetric strips, and microstrip feed-line. The slot and asymmetric strips are printed on the top layer of the rogers substrate and the feed-line is printed on the bottom layer. Rogers 4003C substrate ($\epsilon_r=3.38$, $\tan\delta=0.0027$) is used with height of 1.52mm. The slot antenna is perturbed at the corners, which produces two orthogonal modes that are in degenerative nature to obtain CP. The corner perturbation is optimized to obtain better axial ratio bandwidth. The slot resonance frequency is calculated using equation (4.1). The square slot antenna is designed using equation 4.1 produces linear polarization. The corners of the square slot antenna are perturbed to achieve CP. The axial ratio value is improved by increasing perturbation up to $a=8.4\text{mm}$. Further increase in the value of perturbation deteriorates the axial ratio. This perturbed slot gives CP in the lower band. Further, the perturbed slot loaded with asymmetric cross strips gives the higher band. The strip mode and slot mode together gives CP in the higher frequency band. The asymmetry in

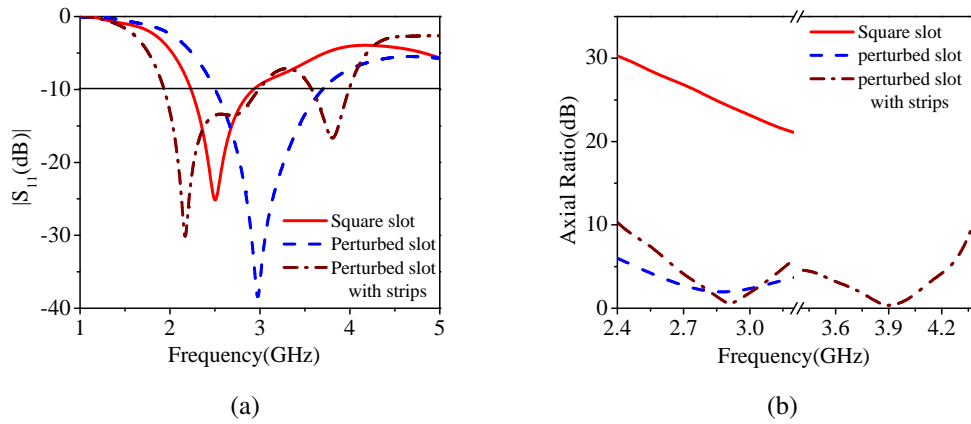


Figure 6.2: The design process of presnetd dual-band CP antenna. (a) Simulated reflection coefficient (b) Simulated axial ratio

strips helps to achieve better axial ratio value at the upper band. The simulation results of reflection coefficient magnitude and axial ratio curves for different configurations of the proposed antenna are shown in Fig.6.2. It is observed that the square slot resonates at 2.6 GHz with a linearly polarized wave. The corner truncated square slot resonates at 2.95 GHz with two orthogonal degenerate modes produces CP. The resonant frequency is shifted to the higher side because of the reduced size of the corner truncated slot antenna. Finally, the asymmetric cross strips loaded slot antenna gives dual-band operation at 2.16 GHz and 3.82 GHz with circular polarization capability in both bands.

The electric field distribution of perturbed slot antenna at different time instant at 2.76 GHz is shown in Fig.6.3. From results, it shows that the perturbed slot antenna radiates the LHCP wave in +z direction. The corners should be perturbed at the opposite side of the slot antenna to obtain RHCP waves. Fig. 6.4 shows the surface current distribution of the proposed design at 3.82 GHz. It is also radiating the LHCP wave at its resonance frequency. The optimized performance of the axial ratio in both the bands is achieved by tuning slot and strips dimensions.

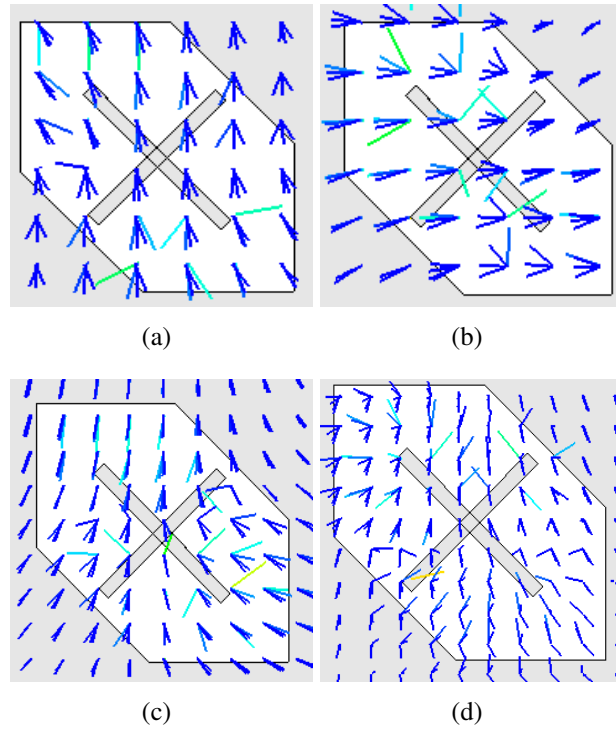


Figure 6.3: Simulated Electric field distribution at 2.76 GHz (a) $t=0^\circ$ (b) $t=90^\circ$ and 3.82GHz (c) $t=0^\circ$ (d) $t=90^\circ$

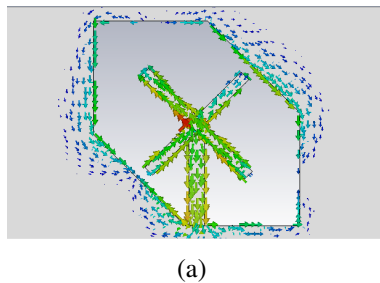


Figure 6.4: Simulation results of surface current distribution of designed antenna at 3.82GHz

6.2.2 Fabricated antenna and experimental results

Fig. 6.5 shows the fabricated prototype of the proposed dual-band CP antenna. The measured and simulated impedance bandwidth (IBW) ($S_{11} < -10dB$) is shown in Fig.6.6(a). The simulated IBW of 48.14% from 1.94 GHz to 2.98 GHz at lower frequency band and 17.75% from 3.58 GHz to 4.18 GHz at the upper-frequency band is achieved. The measured IBW of 40.70% from 1.96 GHz to 2.88 GHz at lower band and 16.56% from 3.62 GHz to 4.18 GHz at the upper band is achieved. The ratio of

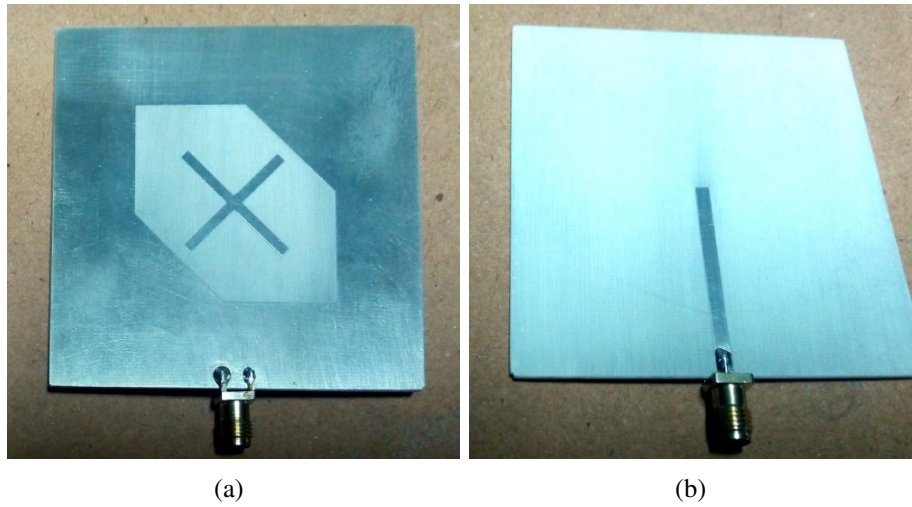


Figure 6.5: The fabricated prototype of proposed dual band CP antenna (a) top view (b) bottom view

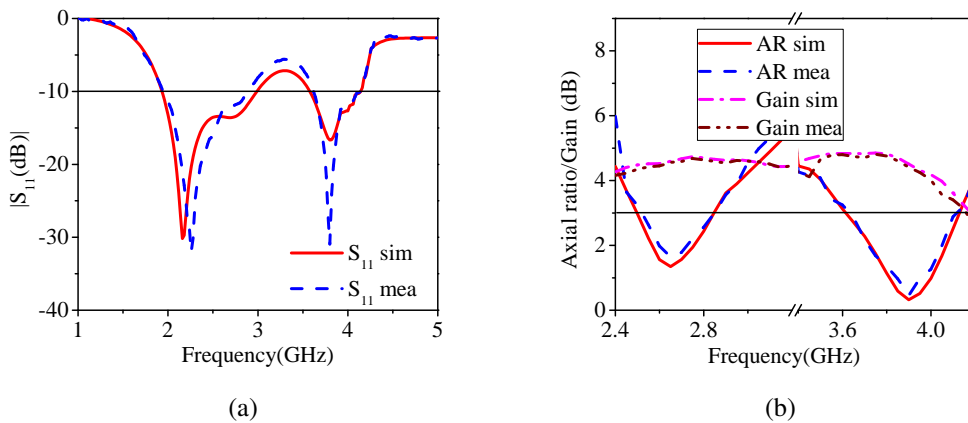


Figure 6.6: (a) Simulated and measured reflection coefficient (b) Simulated and measured axial ratio and gain

two orthogonal polarized components normal to the wave propagation direction gives the axial ratio. The simulated AR bandwidth of 16.20% from 2.5 GHz to 2.85 GHz at lower band and 16.27% from 3.6 GHz to 4.15 GHz at the upper band is achieved. The measured AR bandwidth of 13.27% from 2.55 GHz to 2.85 GHz at lower band and 13.31% from 3.65 GHz to 4.1 GHz at the upper band is achieved. Fig.6.6(b) shows the measured and simulated plots of axial ratio and broadside peak gain. There is a 0.5 dB variation of gain over the axial ratio bandwidth. The maximum peak gains of 4.68 dB at the lower band and 4.81 dB at the upper band is achieved. The axial ratio bandwidth

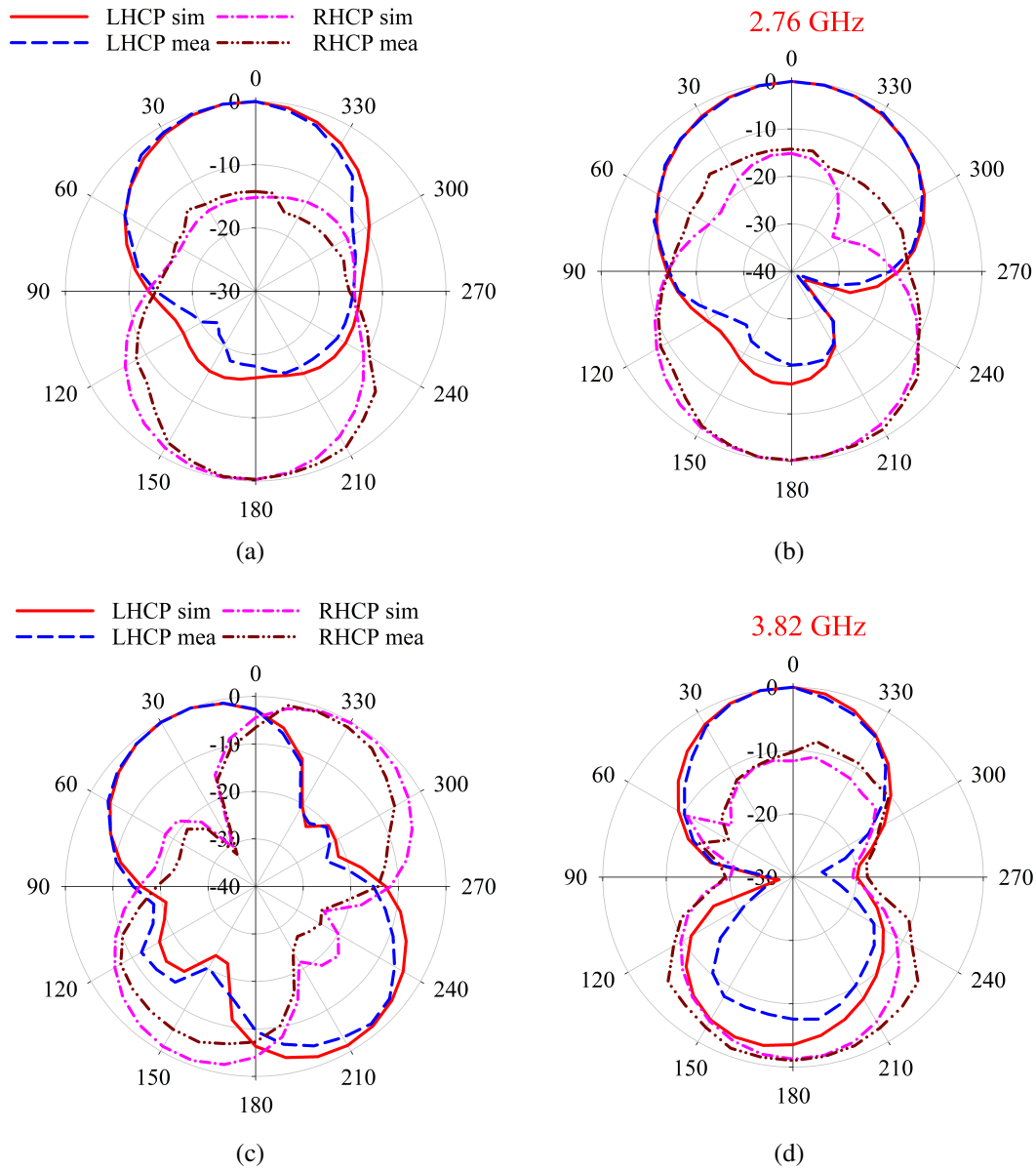


Figure 6.7: Comparison between measured results and simulated results of radiation pattern of the dual band CP antenna at 2.76 GHz and 3.82 GHz. (a)xz plane (b) yz plane (c)xz plane (d) yz plane

is obtained at an inclined angle of 20° in the lower frequency band and upper-frequency band, respectively. This is due to the corner truncation of the slot antenna and the orientation of strips diagonally. The radiation patterns of the dual-band CP antenna in azimuth and elevation planes are shown in Fig.6.7. The results show that the LHCP wave is well radiated and the RHCP level is -10 dB below LHCP level at an angle of 20° . The measured results are in accordance with the simulated results.

6.3 Tri-band circularly polarized antenna using SRRs

A truncated planar slot antenna loaded with a pair of SRRs for triband CP application is discussed in this section. In the structure, the CP in the first band is achieved by the perturbation of two corners of the square slot antenna which resonates at 4.15 GHz. The corner perturbation gives two orthogonal modes which are degenerative in nature produce CP in this band. A pair of SRRs are loaded on the slot antenna to get the resonances at 4.77 GHz in the second and 5.1 GHz in the third band, respectively. In the second and third band, the CP is produced by the orthogonal electric fields due to split gaps in each ring of SRRs. The axial ratio is optimized and tuned independently in all three bands. The proposed design is fabricated and verified experimentally. The experimental results give the axial ratio bandwidths of 450 MHz, 90 MHz and 200 MHz at first, second, and the third band, respectively.

6.3.1 Antenna structure and principle of operation

The proposed antenna is designed using Rogers substrate 4003C ($\epsilon_r=3.38$ and $\tan\delta=0.0027$) with a thickness of 1.52mm. Fig.6.8 shows the geometry of the antenna and it consists of a single layer CPW fed corner truncated slot antenna and a pair of SRRs. The slot and SRRs are printed on the top surface of the rogers substrate. The resonance frequency of the slot antenna is calculated using equation (4.1). The SRR has radii of R_1 and $R_2(R_2=R_1-c-d)$ forming the outer and inner rings with a strip width of c . d is the spacing between two rings and the similar gaps in both rings are $g_1=g_2$. The SRR_1 resonates at 4.77 GHz with parameters given by $R_1=3$ mm, $R_2=2.4$ mm, $c=0.5$ mm, $d=0.2$ mm, $g_1=g_2=0.7$ mm. The resonance frequency (Saha and Siddiqui (2012)) of the rotated SRR is given by,

$$f_0 = \frac{1}{2\pi\sqrt{L_t C_{eq}}} \quad (6.1)$$

where, $C_{eq} = \frac{(\pi+q)^2-\theta^2}{2(\pi+q)} r_{avg} C_{pul}$, $q = \frac{C_g}{r_{avg} C_{pul}}$, $C_{g1}=C_{g2}= C_g$ is the split gap capacitance of the rings, r_{avg} is the uniform average dimension of the inner and outer ring of SRR,

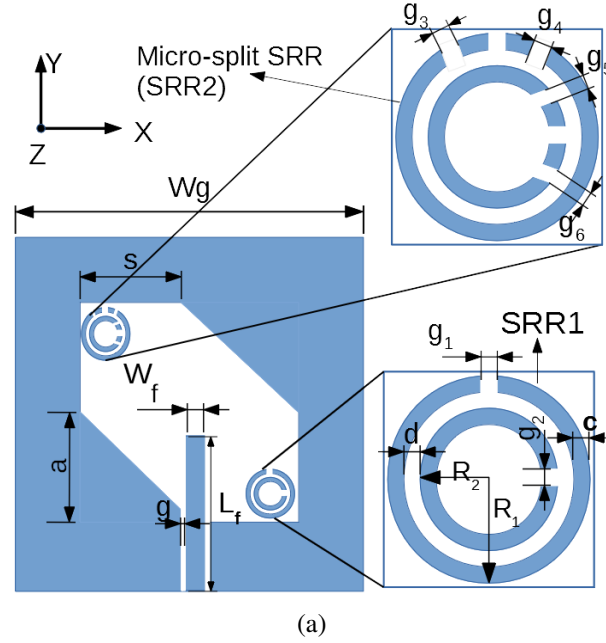


Figure 6.8: Geometry of the triband CP antenna $W_g=70$ mm, $S=28$ mm, $a=10$ mm, $W_f=3$ mm, $g=0.7$ mm, $L_f=33$ mm

C_{pul} is capacitance per unit length between outer and inner rings of SRR, θ is the angle of rotation of the inner ring with respect to the outer ring and L_t is the total equivalent inductance for circular rings with circumference $l = 2\pi r_0 - g$ having thickness $c_1=c_2=c$ is given by,

$$L_t = 0.0002l(2.303\log_{10}\frac{4l}{c} - 2.451) \quad (6.2)$$

The capacitances C_1 and C_2 are equal when two split gaps of SRR are aligned in the same axis. When the inner ring is rotated 90° with respect to the outer ring, the values of C_1 and C_2 become unequal. C_1 and C_2 are calculated as, $C_1 = (\pi - \theta)r_{avg}C_{pul}$ and $C_2 = (\pi + \theta)r_{avg}C_{pul}$. The micro-splits [Ekmekci et al. (2009)] are etched on SRR_2 to achieve the third band with CP. The micro-split gap dimensions are $g_3 = g_4 = g_5 = g_6 = g_c=0.3$ mm. The split gaps which are orthogonal to each other concerning the conventional axis of SRR generate orthogonal electric fields which are required for circular polarization. The gaps are optimized to obtain a better axial ratio at the second and third bands.

The proposed work presents a truncated slot antenna with a pair of SRRs for triband CP. The truncated slot antenna generates two orthogonal modes, which are degenerate

tive to produce CP in the first band by optimizing the truncation. Fig.6.9 shows the simulation results of the reflection coefficient and the axial ratio of the perturbed slot antenna for different truncated values. The incremental values of truncation increase the axial ratio of the slot. The value of truncation is optimized to $a=10$ mm, further increase of truncation deteriorates the axial ratio value. The SRRs are placed at the two diagonal corners of the slot antenna and it is excited by the axial magnetic field of the slot gives second and third band respectively. Fig. 6.10 shows the design process

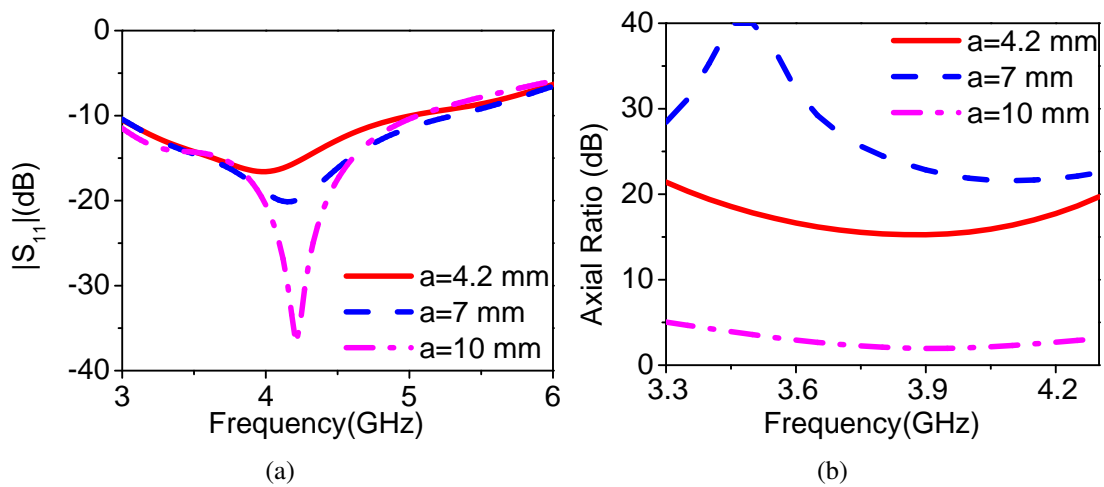


Figure 6.9: Simulation results of reflection coefficient and axial ratio of truncated slot antenna for different values of a (a)S11 (b) axial ratio

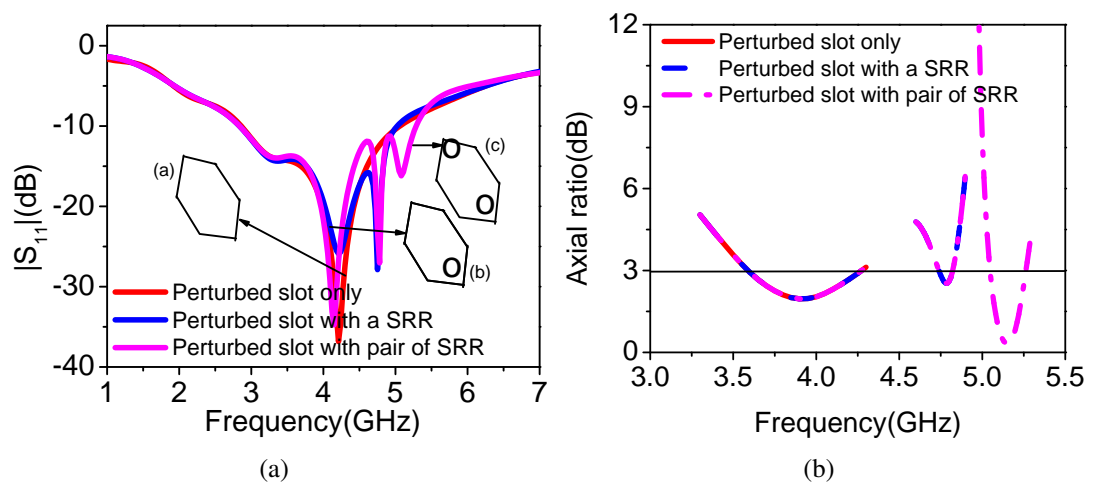


Figure 6.10: Simulation results of reflection coefficient and axial ratio of triband CP antenna design process. (a) Reflection coefficient (b) Axial ratio

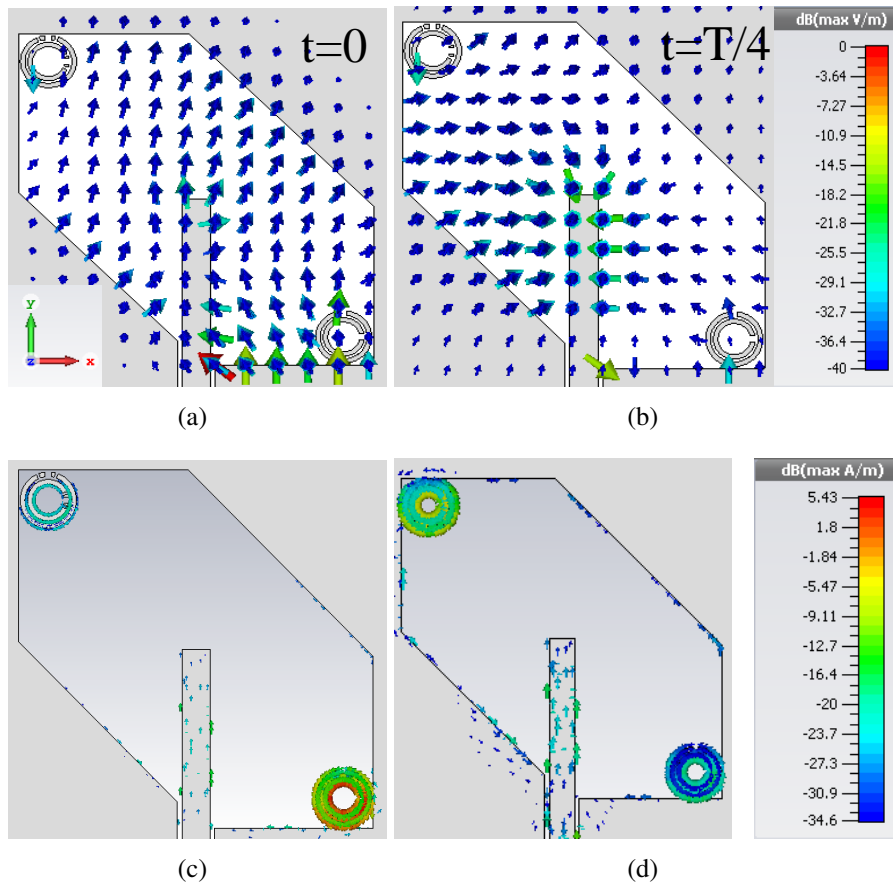


Figure 6.11: Simulated Electric field distribution at 4.4 GHz. (a) $\omega t = 0^0$ (b) $\omega t = 90^0$
 (c) variation in the surface current of SRRs at 4.77 GHz and 5.1 GHz.

of the triband CP antenna. The CPW fed perturbed slot antenna (case a) resonates at 4.15 GHz with circularly polarized waves. The axial ratio curves in Fig.6.10(b) shows that the perturbed slot generates CP at its resonance frequency. The corner perturbed slot with a rotated SRR (case b) resonates at 4.77 GHz produces circular polarization at the second band. To achieve tri-band operation, a micro-split SRR is placed at another corner of the slot antenna (case c), which resonates at 5.1 GHz and achieves CP in the third band. Fig.6.11(a) and (b) shows the electric field variation of the truncated slot antenna at different instances of time. From the figure, the observation shows that the LHCP waves are radiated by the truncated slot in the +z -direction. The corners should be truncated at the opposite corner of the slot to obtain the RHCP wave. Fig.6.11(c) and (d) show the variation of the surface current of SRRs at 4.77 GHz and 5.1 GHz. The two SRRs are also radiating LHCP waves at their corresponding resonance frequency. The

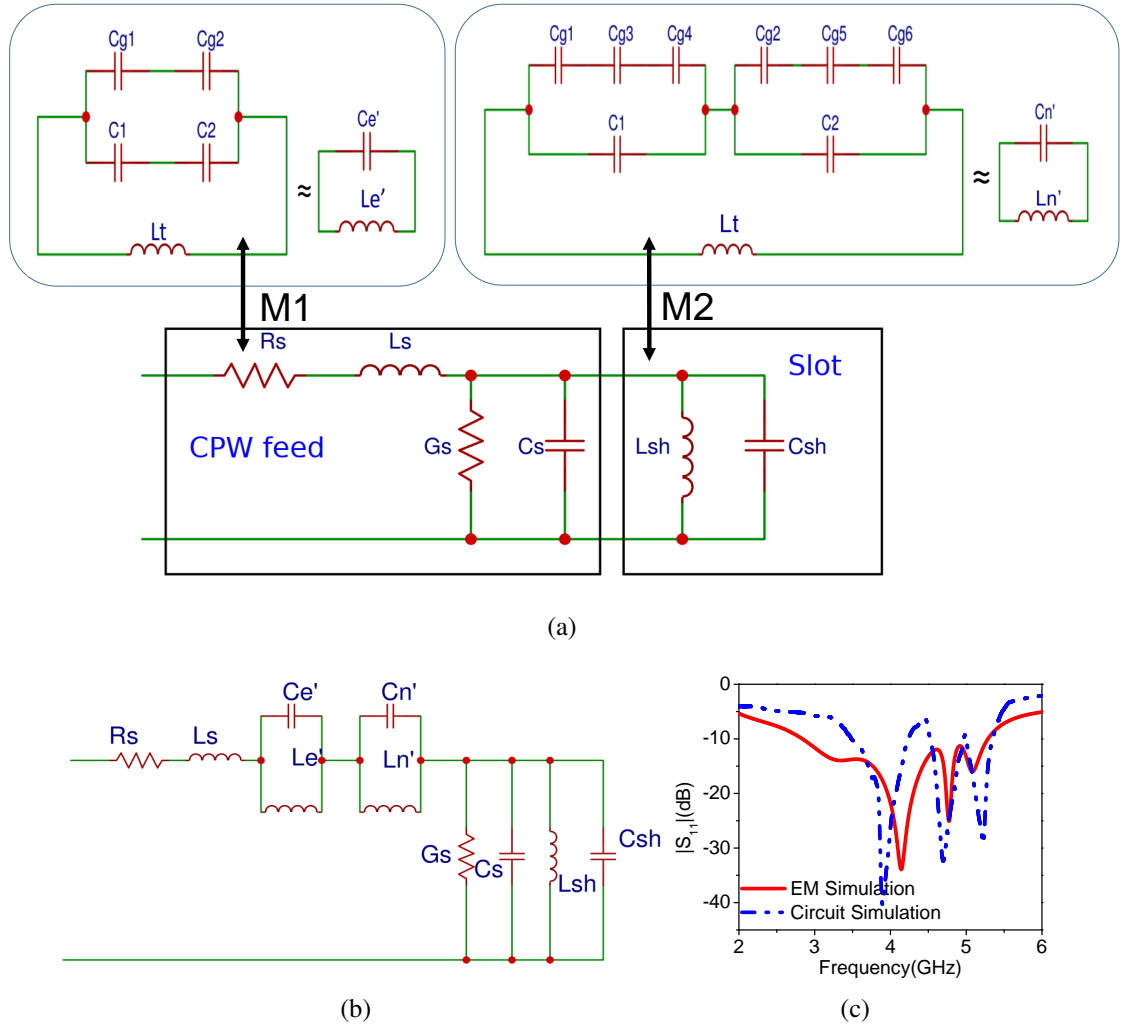


Figure 6.12: Equivalent circuit modeling of the triband CP antenna (a) SRR loaded CPW fed slot antenna (b) simplified equivalent circuit of proposed antenna. (c) The simulated reflection coefficient comparison between EM and circuit simulation

optimized performance of the axial ratio in all the bands is achieved by independently tuning the slot and SRRs modes. The equivalent circuit of a pair of SRR loaded slot antenna [Saha and Siddiqui (2012)] is shown in Fig.6.12(a). Where R_s and G_s are the losses in the feed and substrate. L_s is feed inductance, C_s is feed gap capacitance, L_{sh} and C_{sh} represent the slot. Fig.6.12(b) shows the simplified equivalent circuit of the triband CP antenna. C_e' and L_e' are the effective equivalent capacitance and inductance of the SRR_1 . C_n' and L_n' are the effective equivalent capacitance and inductance of the SRR_2 . $M1$ and $M2$ are the mutual coupling coefficients between SRRs and the slot.

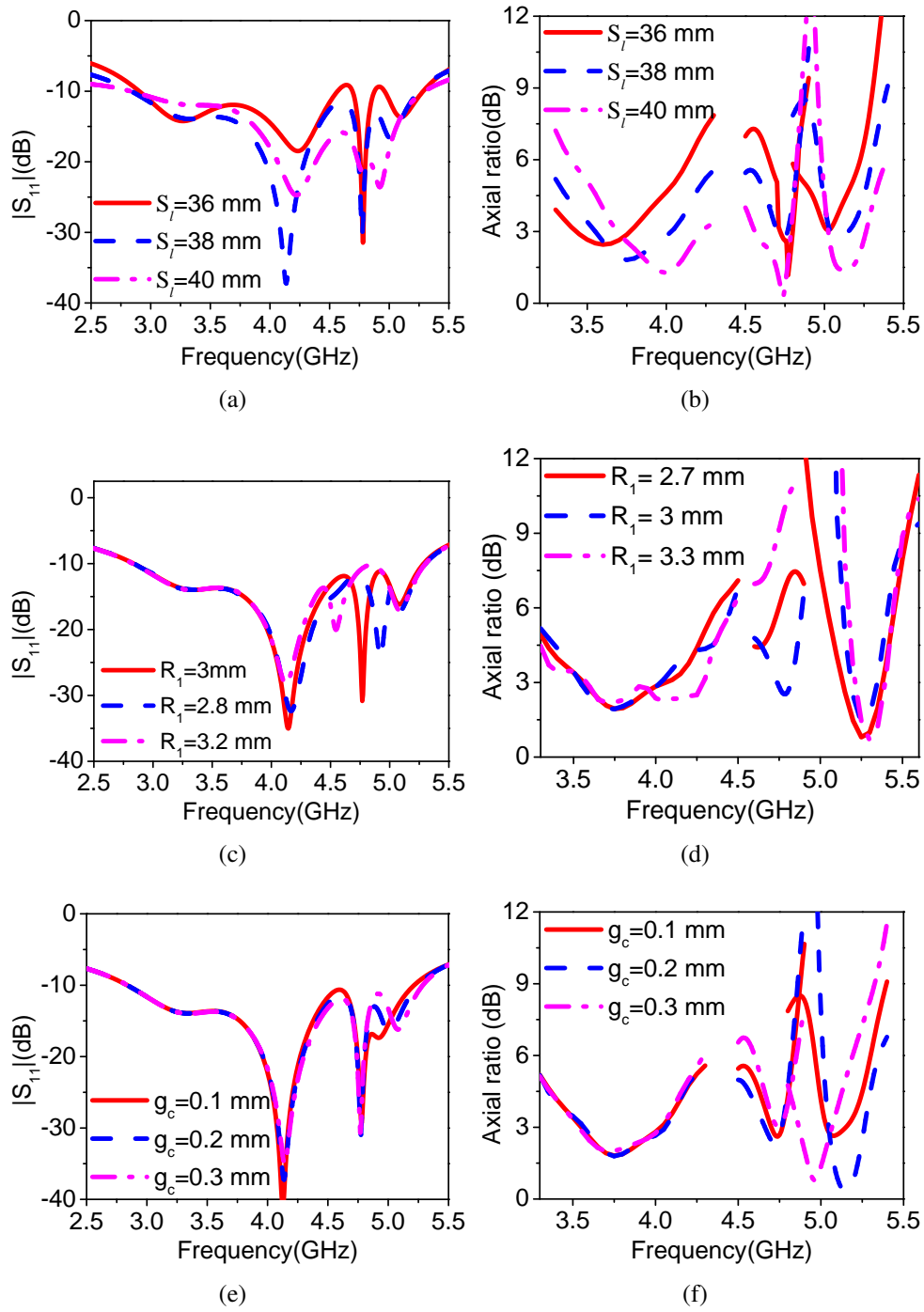


Figure 6.13: Simulation results of reflection coefficient and axial ratio due to variation of S_l , R_1 and split gap g_c . (a) S_{11} due to variation of S_l (b) axial ratio due to variation of S_l (c) S_{11} due to variation of R_1 (d) axial ratio due to variation of R_1 (e) S_{11} due to variation of g_c (f) axial ratio due to variation of g_c

The calculated resonance frequency of SRR using equation (6.1) is $f_0=4.65$ GHz. The corresponding values of L'_e , C'_e , L'_n and C'_n are 9.14 nH, 0.128 pF, 9 nH and 0.103 pF respectively. Fig.6.12(c) shows the reflection coefficient comparison between EM simulation and circuit simulation. In the figure, the EM simulation is in accordance with the circuit simulation in each frequency band. The values of L_{sh} and C_{sh} are 0.13 nH and 1.37 pF.

The parametric study of the proposed antenna to analyze the sensitivity of parameters is shown in Fig.6.13. In the first band, the results show that the value of truncation plays a vital role in achieving an optimized axial ratio. The ring radius and micro-split gaps in the ring are responsible for the tuning of a second and third band. Fig. 6.13(a) and (b) shows the simulation results of the reflection coefficient and axial ratio for the variation in S_l value, the resonance shifts due to the variation in the electrical dimension of the slot antenna. There is a substantial variation in the axial ratio of the first band due to the perturbation effect, but the second and third bands are not affected by this perturbation. Fig.6.13(c) and (d) shows the reflection coefficient and axial ratio due to the variation of the ring radius. It is noticed from the figure that there is a significant variation in the axial ratio and impedance bandwidth of the second band due to the variation of electrical dimensions of the ring. The first and third bands are not affected by SRR_1 . The gap variation of micro-split SRR changes the resonance and axial ratio of the third band and it is shown in Fig.6.13(e) and Fig.6.13(f). This variation is due to the change in the capacitance value of the micro-splits. There is no significant variation observed on the slot and SRR_1 resonance due to these micro-splits. This shows that the bands can be tuned independently to desired resonance with SRR dimension and micro-splits.

6.3.2 Fabricated prototype and its results

The fabricated triband CP antenna is shown in Fig.6.14(a) to verify the simulated design and its measurement set-up is shown in Fig.6.14(b). The comparison is made between measured and simulated impedance bandwidth ($S_{11} < -10dB$), axial ratio bandwidth

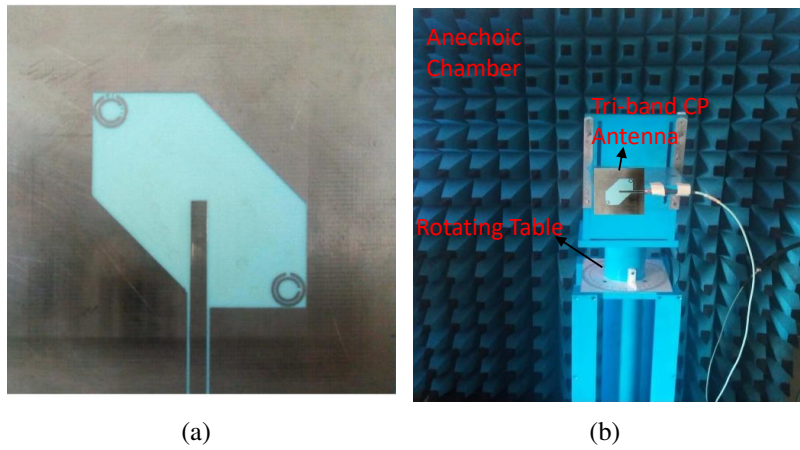


Figure 6.14: (a) Prototype of the fabricated antenna (b) Radiation pattern measurement set-up for the proposed tri-band CP antenna

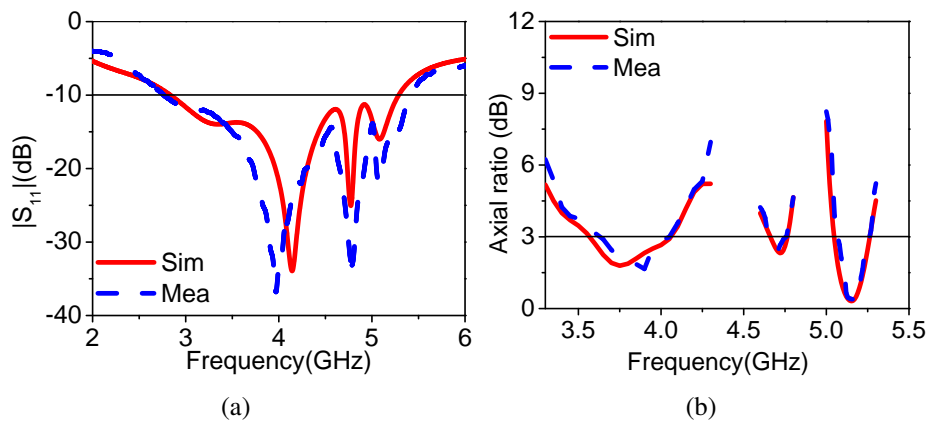


Figure 6.15: (a) Simulated and measured reflection coefficient (b) Simulated and measured axial ratio

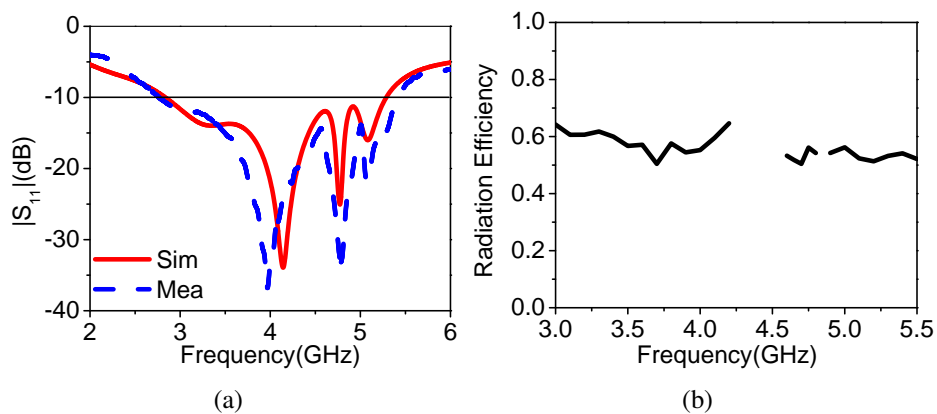


Figure 6.16: Comparison between measured and simulated gain and simulated radiation efficiency (a) Gain (b) Radiation efficiency

(AR < 3dB), and broadside gain. Fig.6.15(a) shows the simulated and measured reflection coefficient. The measured and simulated axial ratio is shown in Fig.6.15(b). The simulated impedance bandwidth of 60.44% is achieved from 2.84 GHz to 5.30 GHz and the impedance bandwidth of 64.54% is achieved from 2.77 GHz to 5.41 GHz experimentally. The simulated and measured axial ratio bandwidth of 13.15% (3.55 GHz-4.05 GHz) and 11.76% (3.6 GHz-4.05 GHz) is achieved at the first band, 2.33% (4.66 GHz-4.77 GHz) and 1.9% (4.67 GHz-4.76 GHz) is achieved at the second band, 4.47% (5.03 GHz-5.26 GHz) and 3.87%(5.06 GHz-5.26 GHz) is obtained at the third band. Fig.6.16(a) shows the simulated and measured broadside gain. The broadside peak gain of 2.88 dBic at the first band, 1.96 dBic at the second band and 2.96 dBic at the third band is achieved at 3.9 GHz, 4.7 GHz and 5.2 GHz respectively with 1 dB variation over axial ratio bandwidth. The simulated radiation efficiency of around 58% at the first resonant frequency, 52% at the second resonance frequency and 51% at the third resonance frequency are obtained and the graph is shown in Fig.6.16(b). The comparison is made between simulated and measured radiation patterns of the triband CP antenna in azimuth and elevation planes are shown in Fig.6.17. The figure shows that the measured and simulated radiation patterns are bidirectional and they are in good agreement with co-pol and x-pol levels in all the bands. The RHCP level is -12 dB below LHCP level in the first band, -20 dB at the second and third band respectively. The LHCP is obtained at an inclined angle of 20⁰, 2⁰ and 32⁰ with respect to broadside direction at the first, second and third band, respectively. This is due to the truncation effect of the slot antenna and gap capacitance of the micro-splits. The variation in simulated and measured patterns is due to measurement errors and connector losses. Also, the high cross-polarization is due to the geometry of the CPW feeding structure. Table 6.1 gives the comparison table of the triband CP antenna with previous literature.

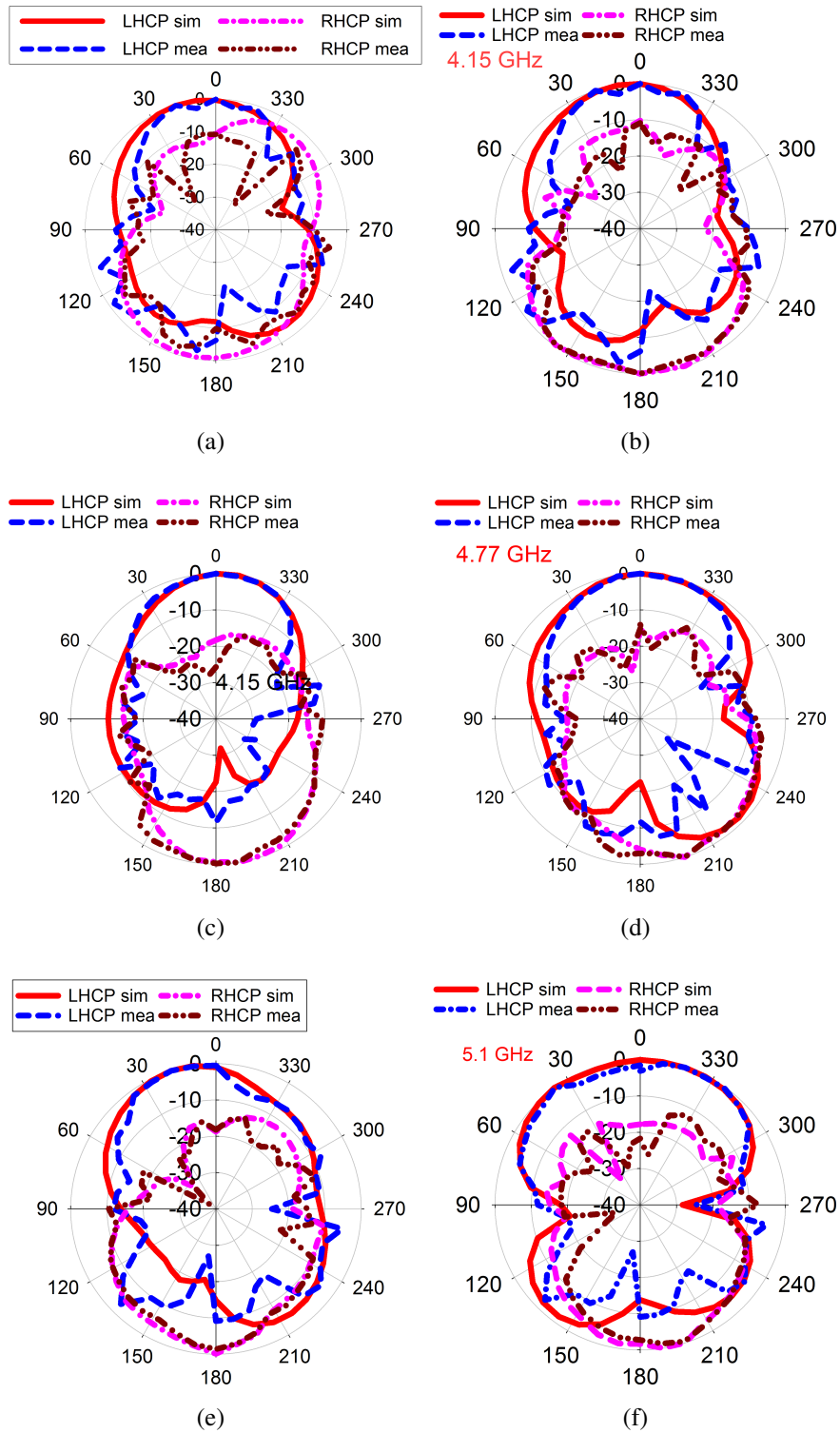


Figure 6.17: Simulated and measured radiation pattern of proposed antenna at 4.15 GHz, 4.77 GHz, 5.1 GHz (a)xz plane (b) yz plane (c)xz plane (d) yz plane (e)xz plane (f) yz plane

Table 6.1: The comparison of the triband CP antenna with recent literature

Ref.	Size	Impedance bandwidth (%)	Axial ratio Bandwidth(%)	Gain(dBic)	Independent Band and Polarization Sense Tunability
[Chen et al. (2017)]	$0.201\lambda_g \times 0.201\lambda_g$	2.3, 7.3	0.62, 1.41	6.4, 7.9	No
[Wang et al. (2018)]	$0.42\lambda_g \times 0.42\lambda_g$	0.69, 5.53	3.79, 1.43	1.43, 5	No
[Xu et al. (2017)]	$1.25\lambda_g \times 1.25\lambda_g$	44, 70.9	35.9, 44, 6.3	6, <4.2	No
[Kandasamy et al. (2016)]	$1.48\lambda_g \times 1.48\lambda_g$	13.15, 14.88	3.1, 4.2	5.9, 6.2	Yes
[Hoang and Park (2014)]	$0.68\lambda_g \times 0.65\lambda_g$	70.6	12, 10, 4.4	<3.13	No
[Bao and Ammann (2014)]	$0.48\lambda_g \times 0.48\lambda_g$	3.37, 4.66, 7.49	0.625, 1.25, 0.63	4.2, 5.5, 4	No
[Tan and Wang (2016)]	$0.41\lambda_g \times 0.49\lambda_g$	15.5, 22.5	7.34, 15.81	2.48, 3.09	No
proposed	$1.78\lambda_g \times 1.78\lambda_g$	64.54	11.76, 1.9, 3.87	2.88, 1.96, 2.96	Yes

6.4 Summary

In this chapter, two CP antennas were discussed. A dual-band CP antenna is presented in the first section and it gives wide CP bandwidth in both the bands. The truncated corner slot antenna is used to obtain CP in the lower frequency band and a pair of asymmetric cross strips helps to achieve CP in the higher frequency band. In this design, the two frequency bands cannot be tuned independently. In the second section, a triband CP antenna is proposed with the independent tuning of each frequency band. A pair of SRRs are used with the truncated slot antenna to obtain triple bands. The truncated corner slot antenna gives CP in the first band. A rotated SRR and micro-split based SRR with equal split gaps placed on the perturbed slot antenna gives CP in the second and third frequency bands, respectively. All the frequency bands are tuned independently to each other. Also, the polarization sense can be tuned independently.

CHAPTER 7

CONCLUSION AND FUTURE WORK

The need for circularly polarized antennas with multiple functionalities is rapidly growing in the modern era due to demand in new generation wireless communication. Mobile applications require low profile wideband/multi-band CP antennas. In military and stealth technology, it requires antennas which have good in-band and out-band low RCS capability. Space applications like radar and satellite communication demand low profile compact high gain CP antennas. This research aims at the design and development of wideband, multi-band and high gain CP antennas using the potential properties of metamaterials. Also, CMA is used effectively to analyze the modes of the MTS antenna. The presented antenna models are capable of providing

- A low profile compact antenna with circular polarization and in-band RCS reduction capability.
- Circular polarization over wide bandwidth with stable gain using frequency selective surface.
- High gain and polarization conversion from LP to CP at the required resonance frequency.
- Triple band circularly polarized antenna with independent control of each resonance frequency and polarization sense at each band as required.

7.1 Contributions

The thesis contribution can be summarized into sections based on designed antennas and their applications.

7.1.1 CM based CP metasurface Antenna

The MTS is designed and analyzed to achieve a circularly polarized wave using source free characteristic modes. Two degenerate modes required to produce CP are analyzed using the eigenvalue equation that is responsible for broadside radiation. These two modes are excited with simple slot geometry. Further, the absorptivity property of MTS is used to find the in-band RCS reduction capability of the antenna. The proposed structure is compact and verified in-terms of axial ratio bandwidth, impedance bandwidth, gain and monostatic RCS values experimentally.

7.1.2 Wideband CP antennas

In the first design, the slot antenna is simulated and fabricated with wideband CP characteristics using FSS. The square slot antenna is truncated to achieve good axial ratio bandwidth. To improve axial ratio bandwidth and gain of slot antenna, a 6 X 10 array of FSS unit cells are arranged and placed below the slot antenna at an optimum height. 3 dB axial ratio bandwidth of 31.14% is achieved with a peak gain of 4.87 dBiC at the resonance frequency of 4.2 GHz. In the second design, a wideband CP characteristic is obtained using the combined resonances of truncated square slot antenna and SRR. Both resonances are independently tunable to obtain optimized axial ratio bandwidth. Axial ratio bandwidth of 21.68% is achieved with a peak gain of 2.74 dBiC. Since it is a compact antenna with a single layer design, it can be used to test the moisture content present in the soil. In the proposed method, wet and dry soils are tested experimentally and significant change in the reflection coefficient is observed.

7.1.3 High gain CP antennas

Compact high gain CP antennas are realized using zero-index based MTS. Gain enhancement of simple patch antennas is obtained by placing a zero-index based MTS atop of the patch antennas. The first design has a CP patch antenna with an array of unit cells as MTS placed atop of patch. The gain of the CP patch antenna is enhanced

using zero refractive index property of MTS. Reflection and transmission coefficients of the MTS unit-cell are analyzed and its constitutive parameters are extracted. The zero refractive index based MTS has no phase variation at its surface and focus the energy towards the direction normal to its interface, thus enhancing the gain. In the second design, The unit cell is designed to achieve zero refractive index and polarization conversion from LP to CP simultaneously. Axial ratio is calculated using the reflection and transmission property of the unit-cell. The gain of an LP patch antenna is increased along with LP to CP conversion. The gain of around 12 dBic is achieved in both designs. The proposed designs are fabricated and verified in-terms of axial ratio bandwidth, impedance bandwidth and gain experimentally.

7.1.4 Multiband CP antennas

This section contributes to the design of dual and triband CP antennas. In the first design, a dual-band CP antenna is designed using a truncated slot antenna loaded with a pair of asymmetric cross strips. The lower band CP is obtained using the truncated slot antenna, which generates two orthogonal degenerate modes required to produce CP. The combination of slot and strip mode achieves CP in the second band. In the second design, a triband CP antenna is designed using a MTM structure called a split ring resonator. The truncated slot antenna gives CP in the first band. A rotated SRR and a micro-split SRR achieve CP in the second and third bands, respectively. The resonant frequency of each band is tuned independently. The comparison is made between circuit and EM simulations. The equivalent circuit of the proposed design is discussed with optimized values of the circuit components, and its simulation is performed using ADS software. The proposed prototypes are fabricated and verified experimentally.

7.2 Future Work

In the present era, Space communication needs circularly polarized antennas with wide-band and high gain characteristics with good in-band and out-band RCS reduction ca-

pability. The presented designs can be further extended to achieve CP with multiple characteristics using phase gradient metasurfaces(PGM). PGM is the potential structure in which phase, amplitude and polarization of each unit cell can be controlled. The active metasurface antennas can be designed using the pin diodes and varactor diodes. These diodes are incorporated into MTS to achieve frequency, polarization and pattern reconfigurability. In optical communication, compact metasurface antennas are needed to achieve a myriad of future applications like optical meta-lenses, meta-holograms, and Quantum MTS. The Optical metasurfaces(OMs) are the emerging solutions to solve the problems of bulky optical antennas. The new fundamental method is adopted in OM is to scatter the light by nanostructure rather than the conventional method of refraction and propagation. The ultra-thin dielectric metasurfaces are promising structures to increase the efficiency and manipulate the light emission and detection in the optical domain. The programmable metasurfaces are emerging solutions to reduce the hardware requirements in future wireless communication. Also, in the medical field, these metasurfaces are designed to test the biological tissue samples and their frequency responses.

The shortage of bandwidth due to the rapid increase of mobile data and high-speed communication facing the wireless carriers needs the exploration of millimeter-wave communication. The compact and low profile antennas can be designed in millimeter-wave frequency to achieve multiple functionalities. The wideband and multi-band CP antennas can be designed with less size and low complexity. There is a need for miniaturized multi-band antennas in the area of a biomedical field that requires communication into different parts of the body tissues. The recognition of diseased tissues and its treatment led to the development of these miniaturized multi-band antennas.

LIST OF PUBLICATIONS BASED ON THESIS

Peer reviewed International Journals

1. Puneeth Kumar T R, Karthik Rudramuni and Krishnamoorthy Kandasamy, "Characteristic Mode Based Compact Circularly Polarized Metasurface Antenna for In-Band RCS Reduction", International Journal of Microwave and Wireless Technologies. 1-7. doi:10.1017/S1759078719001119, Sep. 2019.
2. Puneeth Kumar T R, Karthik Rudramuni and Krishnamoorthy Kandasamy, "A Wideband Circularly Polarized Slot Antenna Backed by Frequency Selective Surface" Journal of Electromagnetic Engineering and Science. Vol. 19(3), PP. 166-171, July 2019.
3. Puneeth Kumar T R, Karthik Rudramuni and Krishnamoorthy Kandasamy, "A High Gain Circularly Polarized Antenna Using Zero-Index Metamaterial" IEEE antennas and Wireless Propagation Letters. Vol. 18, no. 6, PP. 1129-1133, June 2019.
4. Puneeth Kumar T R, Karthik Rudramuni and Krishnamoorthy Kandasamy, "Compact Triband Circularly Polarized Planar Slot Antenna loaded with Split Ring Resonators", International Journal of RF and Microwave Computer-Aided Engineering. <https://doi.org/10.1002/mmce.21953>.
5. Puneeth Kumar T R, Karthik R and Krishnamoorthy K, "Compact Wideband Circularly Polarized SRR Loaded Slot Antenna for Soil Moisture Sensor Application", Microwave Review (Under Revision).

International Conferences

1. Puneeth Kumar T R, Karthik R and Krishnamoorthy K, "A Zero-Index Based Metasurface Antenna with Improved Gain and Circular Polarization Characteristics" 2019 IEEE (Submitted)
2. Puneeth Kumar T R, Karthik Rudramuni and Krishnamoorthy Kandasamy, "Dual Band Circularly Polarized Slot Antenna Loaded with Asymmetric Cross Strips", 2018 IEEE Indian Conference on Antennas and Propagation (InCAP 2018), Hyderabad, India, Dec 16-19, 2018. (Conference Travel grant awarded).
3. Puneeth Kumar T R, Karthik Rudramuni and Krishnamoorthy Kandasamy, "Compact Dual Band Circularly Polarized Planar Slot Antenna loaded with a Rotated SRR", 2018 IEEE-INAE Workshop on Electromagnetics (IIWE), December 06 to 08, 2018, Trivandrum, India.

CURRICULUM VITAE

Name Puneeth Kumar T R

Address Shivapriya,
Indira nagar,Kyathasandra,Tumkur -572104
Karnataka, India

E-mail puneeth.tc@gmail.com

Qualification • M.Tech | Digital Communication Engineering | VTU University Karnataka
• B.E | Telecommunication Engineering | VTU University Karnataka

Experience • Assistant Professor | Siddaganga Institute of Technology, Tumakuru.
• project Trainee| Electronics and Radar Development Establishment.
• Junior Research Fellow | Aeronautical Development Agency.

REFERENCES

- Agarwal, K., Nasimuddin, and A. Alphones (2013a), “Unidirectional wideband circularly polarised aperture antennas backed with artificial magnetic conductor reflectors.” *IET Microwaves, Antennas Propagation*, 7, 338–346.
- Agarwal, K., Nasimuddin, and A. Alphones (2013b), “Wideband circularly polarized amc reflector backed aperture antenna.” *IEEE Transactions on Antennas and Propagation*, 61, 1456–1461.
- Alu, A., F. Bilotti, N. Engheta, and L. Vegni (2003), “How metamaterials may significantly affect the wave transmission through a sub-wavelength hole in a flat perfectly conducting screen.” *IEE Seminar on Metamaterials for Microwave and (Sub) Millimetre Wave Applications: Photonic Bandgap and Double Negative Designs, Components and Experiments 2003*, 11/1–11/8.
- Balanis, Constantine A (2005), *Antenna theory: analysis and design*. Wiley-Interscience.
- Bao, X. L. and M. J. Ammann (2007), “Dual-frequency circularly-polarized patch antenna with compact size and small frequency ratio.” *IEEE Transactions on Antennas and Propagation*, 55, 2104–2107.
- Bao, X. L. and M. J. Ammann (2014), “Printed triple-band circularly polarised antenna for wireless systems.” *Electronics Letters*, 50, 1664–1665.
- Caloz, Christophe and Tatsuo Itoh (2005), *Electromagnetic Metamaterials: Transmission Line Theory and Microwave Applications*. Wiley-IEEE Press.
- Cao, R. and S. Yu (2015), “Wideband compact cpw-fed circularly polarized antenna for universal uhf rfid reader.” *IEEE Transactions on Antennas and Propagation*, 63, 4148–4151.

- Cataldo, A., G. Monti, E. De Benedetto, G. Cannazza, and L. Tarricone (2009), “A non-invasive resonance-based method for moisture content evaluation through microstrip antennas.” *IEEE Transactions on Instrumentation and Measurement*, 58, 1420–1426.
- Chen, C. and E. K. N. Yung (2009), “Dual-band dual-sense circularly-polarized cpw-fed slot antenna with two spiral slots loaded.” *IEEE Transactions on Antennas and Propagation*, 57, 1829–1833.
- Chen, C. H. and E. K. N. Yung (2011), “A novel unidirectional dual-band circularly-polarized patch antenna.” *IEEE Transactions on Antennas and Propagation*, 59, 3052–3057.
- Chen, Hou-Tong, Antoinette J Taylor, and Nanfang Yu (2016a), “A review of metasurfaces: physics and applications.” *Reports on Progress in Physics*, 79, 076401.
- Chen, Hou-Tong, Antoinette J Taylor, and Nanfang Yu (2016b), “A review of metasurfaces: physics and applications.” *Reports on Progress in Physics*, 79, 076401.
- Chen, J., K. F. Tong, A. Al-Armaghany, and J. Wang (2016c), “A dual-band dual-polarization slot patch antenna for gps and wi-fi applications.” *IEEE Antennas and Wireless Propagation Letters*, 15, 406–409.
- Chen, K., J. Yuan, and X. Luo (2017), “Compact dual-band dual circularly polarised annular-ring patch antenna for beidou navigation satellite system application.” *IET Microwaves, Antennas Propagation*, 11, 1079–1085.
- Chen, W., C. A. Balanis, and C. R. Birtcher (2015), “Checkerboard ebg surfaces for wideband radar cross section reduction.” *IEEE Transactions on Antennas and Propagation*, 63, 2636–2645.
- Chen, W., C. A. Balanis, and C. R. Birtcher (2016d), “Dual wide-band checkerboard surfaces for radar cross section reduction.” *IEEE Transactions on Antennas and Propagation*, 64, 4133–4138.

Chen, Y. and C. Wang (2012), “Characteristic-mode-based improvement of circularly polarized u-slot and e-shaped patch antennas.” *IEEE Antennas and Wireless Propagation Letters*, 11, 1474–1477.

Chen, Yikai and Chao-Fu Wang (2015a), *Characteristic Modes*. John Wiley & Sons Ltd.

Chen, Yikai and Chao-Fu Wang (2015b). John Wiley and Sons.

Costa, F., A. Monorchio, and G. Manara (2012), “Efficient analysis of frequency-selective surfaces by a simple equivalent-circuit model.” *IEEE Antennas and Propagation Magazine*, 54, 35–48.

Daviu, Eva Antonino (2008), *Analysis and Design of Antennas for wireless Communications Using Modal methods*. Ph.D. thesis, University of Politecnica, De Valencia.

Deng, C., Z. Feng, and S. V. Hum (2016), “Mimo mobile handset antenna merging characteristic modes for increased bandwidth.” *IEEE Transactions on Antennas and Propagation*, 64, 2660–2667.

Ding, K., C. Gao, T. Yu, and D. Qu (2017), “Wideband cp slot antenna with backed fss reflector.” *IET Microwaves, Antennas Propagation*, 11, 1045–1050.

Ekmekci, Evren, Kagan Topalli, Tayfun Akin, and Gonul Turhan-Sayan (2009), “A tunable multi-band metamaterial design using micro-split srr structures.” *Opt. Express*, 17, 16046–16058.

Eleftheriades, G. V. and K. G. Balmain (2005), *Negative-Refractive Metamaterials: Fundamental Principles and Applications*. Wiley-IEEE Press.

Engheta, Nader and Richard W. Ziolkowski (2006), *Metamaterials: Physics and Engineering Explorations*. John Wiley and Sons, Ltd.

Enoch, S., G. Tayeb, and B. Gralak (2003), “The richness of the dispersion relation of electromagnetic bandgap materials.” *IEEE Transactions on Antennas and Propagation*, 51, 2659–2666.

Enoch, Stefan, Gérard Tayeb, Pierre Sabouroux, Nicolas Guérin, and Patrick Vincent (2002), “A metamaterial for directive emission.” *Phys. Rev. Lett.*, 89, 213902, URL <https://link.aps.org/doi/10.1103/PhysRevLett.89.213902>.

Fabres, Marta Cabedo (2007), *Systematic Design of Antennas Using Theory of Characteristic Modes*. Ph.D. thesis, University of Politecnica, De Valencia.

Fan Yang and Y. Rahmat-Samii (2005), “A low profile single dipole antenna radiating circularly polarized waves.” *IEEE Transactions on Antennas and Propagation*, 53, 3083–3086.

Feresidis, A. P., G. Goussetis, , and J. C. Vardaxoglou (2005), “Artificial magnetic conductor surfaces and their application to low-profile high-gain planar antennas.” *IEEE Transactions on Antennas and Propagation*, 53, 209–215.

Fu, S., Q. Kong, S. Fang, and Z. Wang (2014), “Broadband circularly polarized microstrip antenna with coplanar parasitic ring slot patch for l-band satellite system application.” *IEEE Antennas and Wireless Propagation Letters*, 13, 943–946.

Garbacz, R. and R. Turpin (1971), “A generalized expansion for radiated and scattered fields.” *IEEE Transactions on Antennas and Propagation*, 19, 348–358.

Garbacz, R. J. (1965), “Modal expansions for resonance scattering phenomena.” *Proceedings of the IEEE*, 53, 856–864.

Ghosh, S., S. Bhattacharyya, D. Chaurasiya, and K. V. Srivastava (2015), “An ultrawideband ultrathin metamaterial absorber based on circular split rings.” *IEEE Antennas and Wireless Propagation Letters*, 14, 1172–1175.

Glybovski, Stanislav, Sergei Tretyakov, Pavel Belov, Yuri Kivshar, and Constantin Simovski (2016), “Metasurfaces: From microwaves to visible.” *Physics Reports*, 634.

Han, Z. J., W. Song, and X. Q. Sheng (2017), “Gain enhancement and rcs reduction for patch antenna by using polarization-dependent ebg surface.” *IEEE Antennas and Wireless Propagation Letters*, 16, 1631–1634.

Harrington, R. and J. Mautz (1971), “Computation of characteristic modes for conducting bodies.” *IEEE Transactions on Antennas and Propagation*, 19, 629–639.

Harrington, R. and J. Mautz (1971), “Theory of characteristic modes for conducting bodies.” *IEEE Transactions on Antennas and Propagation*, 19, 622–628.

Hoang, T. V., T. T. Le, Q. Y. Li, and H. C. Park (2016), “Quad-band circularly polarized antenna for 2.4/5.3/5.8-ghz wlan and 3.5-ghz wimax applications.” *IEEE Antennas and Wireless Propagation Letters*, 15, 1032–1035.

Hoang, T. V. and H. C. Park (2014), “Very simple 2.45/3.5/5.8 ghz triple-band circularly polarised printed monopole antenna with bandwidth enhancement.” *Electronics Letters*, 50, 1792–1793.

Holloway, C. L., E. F. Kuester, J. A. Gordon, J. O’Hara, J. Booth, and D. R. Smith (2012), “An overview of the theory and applications of metasurfaces: The two-dimensional equivalents of metamaterials.” *IEEE Antennas and Propagation Magazine*, 54, 10–35.

Huang, C., W. Pan, X. Ma, and X. Luo (2016), “A frequency reconfigurable directive antenna with wideband low-rcs property.” *IEEE Transactions on Antennas and Propagation*, 64, 1173–1178.

Iwasaki, H., K. Kawabata, and K. Yasukawa (1990), “A circularly polarized microstrip antenna using a crossed-slot feed.” *International Symposium on Antennas and Propagation Society, Merging Technologies for the 90’s*, 807–810 vol.2.

J.C.Bose (1898), “On the rotation of plane of polarisation of electric wave by a twisted structure.” *Proc. Roy. Soc.*, 63, 146–152.

Jia, Y., Y. Liu, Y. J. Guo, K. Li, and S. Gong (2017), “A dual-patch polarization rotation reflective surface and its application to ultra-wideband rcs reduction.” *IEEE Transactions on Antennas and Propagation*, 65, 3291–3295.

Jia, Y., Y. Liu, H. Wang, K. Li, and S. Gong (2015), “Low-rcs, high-gain, and wideband mushroom antenna.” *IEEE Antennas and Wireless Propagation Letters*, 14, 277–280.

Jiang, Z. H., Q. Wu, D. E. Brocker, P. E. Sieber, and D. H. Werner (2014), “A low-profile high-gain substrate-integrated waveguide slot antenna enabled by an ultrathin anisotropic zero-index metamaterial coating.” *IEEE Transactions on Antennas and Propagation*, 62, 1173–1184.

Kandasamy, K., B. Majumder, J. Mukherjee, and K. P. Ray (2015), “Low-rs and polarization-reconfigurable antenna using cross-slot-based metasurface.” *IEEE Antennas and Wireless Propagation Letters*, 14, 1638–1641.

Kandasamy, K., B. Majumder, J. Mukherjee, and K. P. Ray (2016), “Dual-band circularly polarized split ring resonators loaded square slot antenna.” *IEEE Transactions on Antennas and Propagation*, 64, 3640–3645.

Karamzadeh, S., V. Rafii, M. Kartal, and H. Saygin (2016), “Compact uwb cp square slot antenna with two corners connected by a strip line.” *Electronics Letters*, 52, 10–12.

Lamb, H. (1904), “On group-velocity.” *Proc. London Math. Soc.*, s2-1, 473–479.

Li, D., Z. Szabo, X. Qing, E. Li, and Z. N. Chen (2012), “A high gain antenna with an optimized metamaterial inspired superstrate.” *IEEE Transactions on Antennas and Propagation*, 60, 6018–6023.

Li, H., K. W. Xu, X. B. Wang, R. Kanan, and L. X. Ran (2013), “Low-profile circularly polarised loop antenna assisted with an effective pmc bandwidth.” *Electronics Letters*, 49, 978–979.

Li, K., Y. Liu, Y. Jia, and Y. J. Guo (2017), “A circularly polarized high-gain antenna with low rcs over a wideband using chessboard polarization conversion metasurfaces.” *IEEE Transactions on Antennas and Propagation*, 65, 4288–4292.

Li, Ke and Yan Shi (2018), “Wideband mimo handset antenna design based on theory of characteristic modes.” *International Journal of RF and Microwave Computer-Aided Engineering*, 28, e21217, URL <https://onlinelibrary.wiley.com/doi/abs/10.1002/mmce.21217>.

Li, R., B. Pan, A. N. Traille, J. Papapolymerou, J. Laskar, and M. M. Tentzeris (2008), “Development of a cavity-backed broadband circularly polarized slot/strip loop antenna with a simple feeding structure.” *IEEE Transactions on Antennas and Propagation*, 56, 312–318.

Li, T. and Z. N. Chen (2018), “A dual-band metasurface antenna using characteristic mode analysis.” *IEEE Transactions on Antennas and Propagation*, 66, 5620–5624.

Liang, W., Y. C. Jiao, Y. Luan, and C. Tian (2015), “A dual-band circularly polarized complementary antenna.” *IEEE Antennas and Wireless Propagation Letters*, 14, 1153–1156.

Lin, F. H. and Z. N. Chen (2017), “Low-profile wideband metasurface antennas using characteristic mode analysis.” *IEEE Transactions on Antennas and Propagation*, 65, 1706–1713.

Liu, Ruopeng, Qiang Cheng, Thomas Hand, Jack J Mock, Tie Jun Cui, Steven Cummer, and D Smith (2008), “Experimental demonstration of electromagnetic tunneling through an epsilon-near-zero metamaterial at microwave frequencies.” *Physical review letters*, 100, 023903.

Liu, T., X. Cao, J. Gao, Q. Zheng, W. Li, and H. Yang (2013), “Rcs reduction of waveguide slot antenna with metamaterial absorber.” *IEEE Transactions on Antennas and Propagation*, 61, 1479–1484.

Liu, Y., Y. Hao, S. Gong, and Y. Xv (2015), “A low-profile and high-gain multilayered slot antenna based on the fabry-perot cavity and the mushroom-like electromagnetic gap band structure.” *2015 International Workshop on Antenna Technology (iWAT)*, 191–193.

Long, M., W. Jiang, and S. Gong (2017), “Wideband rcs reduction using polarization conversion metasurface and partially reflecting surface.” *IEEE Antennas and Wireless Propagation Letters*, 16, 2534–2537.

- Luo, Y., Z. N. Chen, and K. Ma (2019), “Enhanced bandwidth and directivity of a dual-mode compressed high-order mode stub-loaded dipole using characteristic mode analysis.” *IEEE Transactions on Antennas and Propagation*, 67, 1922–1925.
- Majumder, B., K. Kandasamy, and K. P. Ray (2018), “A zero index based meta-lens loaded wideband directive antenna combined with reactive impedance surface.” *IEEE Access*, 6, 28746–28754.
- Majumder, B., K. Krishnamoorthy, J. Mukherjee, and K. P. Ray (2016), “Compact broadband directive slot antenna loaded with cavities and single and double layers of metasurfaces.” *IEEE Transactions on Antennas and Propagation*, 64, 4595–4606.
- Marqués, R., J. Martel, F. Mesa, and F. Medina (2002), “Left-handed-media simulation and transmission of em waves in subwavelength split-ring-resonator-loaded metallic waveguides.” *Phys. Rev. Lett.*, 89, 183901, URL <https://link.aps.org/doi/10.1103/PhysRevLett.89.183901>.
- Meng, F.-Y., Y.-L. Lyu and K. Zhang, Q. Wu, and J.L.-W. Li (2012), “A detached zero index metamaterial lens for antenna gain enhancement.” *progress In Electromagnetic Research*, 132, 463–478.
- Miers, Z. T. and B. K. Lau (2016), “Computational analysis and verifications of characteristic modes in real materials.” *IEEE Transactions on Antennas and Propagation*, 64, 2595–2607.
- Mu, J., H. Wang, H. Wang, and Y. Huang (2017), “Low-rs and gain enhancement design of a novel partially reflecting and absorbing surface antenna.” *IEEE Antennas and Wireless Propagation Letters*, 16, 1903–1906.
- Munk, Ben A. (2000), *Frequency Selective Surfaces: Theory and Design*. John Wiley and Sons.
- Nasimuddin, Z. N. Chen, and X. Qing (2010), “Dual-band circularly polarized *s*-shaped slotted patch antenna with a small frequency-ratio.” *IEEE Transactions on Antennas and Propagation*, 58, 2112–2115.

Nasimuddin, N., Z. N. Chen, and X. Qing (2016), “Bandwidth enhancement of a single-feed circularly polarized antenna using a metasurface: Metamaterial-based wideband circularly polarized rectangular microstrip antenna.” *IEEE Antennas and Propagation Magazine*, 58, 39–46.

Nayeri, P., K. F. Lee, A. Z. Elsherbeni, and F. Yang (2011), “Dual-band circularly polarized antennas using stacked patches with asymmetric u-slots.” *IEEE Antennas and Wireless Propagation Letters*, 10, 492–495.

Pan, S., J. Sze, and P. Tu (2012), “Circularly polarized square slot antenna with a largely enhanced axial-ratio bandwidth.” *IEEE Antennas and Wireless Propagation Letters*, 11, 969–972.

Peixeiro, C. (2012), “Microstrip antenna papers in the IEEE transactions on antennas and propagation [Euraap corner].” *IEEE Antennas and Propagation Magazine*, 54, 264–268.

Pendry, J. B. (2000), “Negative refraction makes a perfect lens.” *Phys. Rev. Lett.*, 85, 3966–3969, URL <https://link.aps.org/doi/10.1103/PhysRevLett.85.3966>.

Pourahmadazar, J. and S. Mohammadi (2011), “Compact circularly-polarised slot antenna for UWB applications.” *Electronics Letters*, 47, 837–838.

Rabah, M. H., D. Seetharamdoo, and M. Berbineau (2016a), “Analysis of miniature metamaterial and magnetodielectric arbitrary-shaped patch antennas using characteristic modes: Evaluation of the Q -factor.” *IEEE Transactions on Antennas and Propagation*, 64, 2719–2731.

Rabah, M. H., D. Seetharamdoo, M. Berbineau, and A. De Lustrac (2016b), “New metrics for artificial magnetism from metal-dielectric metamaterial based on the theory of characteristic modes.” *IEEE Antennas and Wireless Propagation Letters*, 15, 460–463.

- Reddy, V. V. and N. V. S. N. Sarma (2014), “Triband circularly polarized koch fractal boundary microstrip antenna.” *IEEE Antennas and Wireless Propagation Letters*, 13, 1057–1060.
- Ren, J., W. Jiang, K. Zhang, and S. Gong (2018), “A high-gain circularly polarized fabry–perot antenna with wideband low-rcs property.” *IEEE Antennas and Wireless Propagation Letters*, 17, 853–856.
- Rui, X., J. Li, and K. Wei (2016), “Dual-band dual-sense circularly polarised square slot antenna with simple structure.” *Electronics Letters*, 52, 578–580.
- Saha, C. and Jawad Siddiqui (2012), “Theoretical model for estimation of resonance frequency of rotational circular split-ring resonators.” *Electromagnetics*, 32, 345–355.
- Saini, R. K., S. Dwari, and M. K. Mandal (2017), “Cpw-fed dual-band dual-sense circularly polarized monopole antenna.” *IEEE Antennas and Wireless Propagation Letters*, 16, 2497–2500.
- Saraswat, Kapil and A. R. Harish (2018), “Analysis of wideband circularly polarized ring slot antenna using characteristics mode for bandwidth enhancement.” *International Journal of RF and Microwave Computer-Aided Engineering*, 28, e21186, URL <https://onlinelibrary.wiley.com/doi/abs/10.1002/mmce.21186>.
- Saurav, K., D. Sarkar, A. Singh, and K. V. Srivastava (2015), “Multiband circularly polarized cavity-backed crossed dipole antenna.” *IEEE Transactions on Antennas and Propagation*, 63, 4286–4296.
- Shao, Y. and Z. Chen (2012), “A design of dual-frequency dual-sense circularly-polarized slot antenna.” *IEEE Transactions on Antennas and Propagation*, 60, 4992–4997.
- Sharma, P. and K. Gupta (1982), “Optimized design of single feed circularly polarized microstrip patch antennas.” *1982 Antennas and Propagation Society International Symposium*, 20, 156–159.

Shelby, R. A., D. R. Smith, and S. Schultz (2001), “Experimental verification of a negative index of refraction.” *Science*, 292, 77–79, URL <https://science.sciencemag.org/content/292/5514/77>.

Silveirinha, Mario and Nader Engheta (2007), “Design of matched zero-index metamaterials using non-magnetic inclusions in epsilon-near-zero (enz) media.” *Phys. Rev. B*, 75.

Singh, A. K., M. P. Abegaonkar, and S. K. Koul (2017), “High-gain and high-aperture-efficiency cavity resonator antenna using metamaterial superstrate.” *IEEE Antennas and Wireless Propagation Letters*, 16, 2388–2391.

Steven Gao, Qi Luo and Fuguo Zhu (2014), *Introduction to Circularly Polarized Antennas*. John Wiley and Sons, Ltd, URL <https://onlinelibrary.wiley.com/doi/abs/10.1002/9781118790526.ch1>.

Sun, M., Z. N. Chen, and X. Qing (2013), “Gain enhancement of 60-ghz antipodal tapered slot antenna using zero-index metamaterial.” *IEEE Transactions on Antennas and Propagation*, 61, 1741–1746.

Szabo, Z., G. Park, R. Hedge, and E. Li (2010), “A unique extraction of metamaterial parameters based on kramers–kronig relationship.” *IEEE Transactions on Microwave Theory and Techniques*, 58, 2646–2653.

Sze, J. ., J. . Wang, and C. . Chang (2008), “Axial-ratio bandwidth enhancement of asymmetric-cpw-fed circularly-polarised square slot antenna.” *Electronics Letters*, 44, 1048–1049.

Ta, S. X. and I. Park (2015), “Low-profile broadband circularly polarized patch antenna using metasurface.” *IEEE Transactions on Antennas and Propagation*, 63, 5929–5934.

Tan, M. and B. Wang (2016), “A dual-band circularly polarized planar monopole antenna for wlan/wi-fi applications.” *IEEE Antennas and Wireless Propagation Letters*, 15, 670–673.

Tayeb, Gérard, Stefan Enoch, Patrick Vincent, and Pierre Sabouroux (2003), “A compact directive antenna using ultrarefractive properties of metamaterials.” *ICEAA 2003 - International Conference on Electromagnetics in Advanced Applications*.

Turpin, J. P., Q. Wu, D. H. Werner, B. Martin, M. Bray, and E. Lier (2014), “Near-zero-index metamaterial lens combined with amc metasurface for high-directivity low-profile antennas.” *IEEE Transactions on Antennas and Propagation*, 62, 1928–1936.

Veselago, Viktor G (1968), “THE ELECTRODYNAMICS OF SUBSTANCES WITH SIMULTANEOUSLY NEGATIVE VALUES OF ϵ AND μ .” *Soviet Physics Uspekhi*, 10, 509–514.

Vesseur, Ernst Jan, Toon Coenen, Humeyra Caglayan, Nader Engheta, and Albert Polman (2013), “Experimental verification of $n=0$ structures for visible light.” *Physical review letters*, 110, 013902.

Viswanathan, H. and M. Weldon (2014), “The past, present, and future of mobile communications.” *Bell Labs Technical Journal*, 19, 8–21.

Wang, C. J., M. H. Shih, and L. T. Chen (2015), “A wideband open-slot antenna with dual-band circular polarization.” *IEEE Antennas and Wireless Propagation Letters*, 14, 1306–1309.

Wang, M., X. Zhu, Y. Guo, and W. Wu (2018), “Compact dual-band circularly polarised antenna with omnidirectional and unidirectional properties.” *IET Microwaves, Antennas Propagation*, 12, 259–264.

Weng, W. C., J. Y. Sze, and C. F. Chen (2014), “A dual-broadband circularly polarized slot antenna for wlan applications.” *IEEE Transactions on Antennas and Propagation*, 62, 2837–2841.

William A. Imbriale, Steven (Shichang) Gao, and Luigi Boccia (2006), *Space Antenna Handbook*. John Wiley & Sons Ltd.

Wu, Q., W. Su, Z. Li, and D. Su (2016a), “Reduction in out-of-band antenna coupling using characteristic mode analysis.” *IEEE Transactions on Antennas and Propagation*, 64, 2732–2742.

Wu, Z., L. Li, Y. Li, and X. Chen (2016b), “Metasurface superstrate antenna with wide-band circular polarization for satellite communication application.” *IEEE Antennas and Wireless Propagation Letters*, 15, 374–377.

Xu, R., J. Li, Y. Qi, Y. Guangwei, and J. Yang (2017), “A design of triple-wideband triple-sense circularly polarized square slot antenna.” *IEEE Antennas and Wireless Propagation Letters*, 16, 1763–1766.

Yi, H. and S. Qu (2013), “A novel dual-band circularly polarized antenna based on electromagnetic band-gap structure.” *IEEE Antennas and Wireless Propagation Letters*, 12, 1149–1152.

Zhang, J. D., W. Wu, and D. G. Fang (2016), “Dual-band and dual-circularly polarized shared-aperture array antennas with single-layer substrate.” *IEEE Transactions on Antennas and Propagation*, 64, 109–116.

Zhang, J. D., L. Zhu, N. W. Liu, and W. Wu (2017), “Dual-band and dual-circularly polarized single-layer microstrip array based on multiresonant modes.” *IEEE Transactions on Antennas and Propagation*, 65, 1428–1433.

Zhang, L. and T. Dong (2017), “Low rcs and high-gain cp microstrip antenna using sa-ms.” *Electronics Letters*, 53, 375–376.

Zhao, Y., X. Cao, J. Gao, X. Yao, T. Liu, W. Li, and S. Li (2016), “Broadband low-rcs metasurface and its application on antenna.” *IEEE Transactions on Antennas and Propagation*, 64, 2954–2962.

Zhao, Y., X. Cao, J. Gao, X. Yao, and X. Liu (2016), “A low-rcs and high-gain slot antenna using broadband metasurface.” *IEEE Antennas and Wireless Propagation Letters*, 15, 290–293.

- Zhao, Y., J. Gao, X. Cao, T. Liu, L. Xu, X. Liu, and L. Cong (2017), “In-band rcs reduction of waveguide slot array using metasurface bars.” *IEEE Transactions on Antennas and Propagation*, 65, 943–947.
- Zhao, Y., C. Yu, J. Gao, X. Yao, T. Liu, W. Li, and S. Li (2017), “Broadband metamaterial surface for antenna rcs reduction and gain enhancement.” *IEEE Transactions on Antennas and Propagation*, PP, 1–1.
- Zheng, Y., J. Gao, X. Cao, Z. Yuan, and H. Yang (2015), “Wideband rcs reduction of a microstrip antenna using artificial magnetic conductor structures.” *IEEE Antennas and Wireless Propagation Letters*, 14, 1582–1585.
- Zheng, Y., J. Gao, L. Xu, X. Cao, and T. Liu (2017), “Ultrawideband and polarization-independent radar-cross-sectional reduction with composite artificial magnetic conductor surface.” *IEEE Antennas and Wireless Propagation Letters*, 16, 1651–1654.
- Zhou, H., Z. Pei, S. Qu, S. Zhang, J. Wang, Z. Duan, H. Ma, and Z. Xu (2009), “A novel high-directivity microstrip patch antenna based on zero-index metamaterial.” *IEEE Antennas and Wireless Propagation Letters*, 8, 538–541.
- Zhu, H. L., S. W. Cheung, K. L. Chung, and T. I. Yuk (2013), “Linear-to-circular polarization conversion using metasurface.” *IEEE Transactions on Antennas and Propagation*, 61, 4615–4623.
- Zhu, H. L., S. W. Cheung, X. H. Liu, and T. I. Yuk (2014), “Design of polarization reconfigurable antenna using metasurface.” *IEEE Transactions on Antennas and Propagation*, 62, 2891–2898.
- Ziolkowski, Richard W. (2004), “Propagation in and scattering from a matched metamaterial having a zero index of refraction.” *Phys. Rev. E*, 70, 046608, URL <https://link.aps.org/doi/10.1103/PhysRevE.70.046608>.